Towards the investigation of ultrafast dynamics in chiral systems using free-electron lasers

put forward by

Valerija Music

submitted to

Faculty of Mathematics and Natural Sciences
Department Experimental Physics IV
of the University of Kassel, Germany
Dissertation for the Degree of
Doktorin der Naturwissenschaften - Dr. rer. nat. -

Examination board:
Prof. Dr. Arno Ehresmann (Referee)
Prof. Dr. Markus Ilchen (Referee)
Prof. Dr. Stefan Yoshi Buhmann
Prof. Dr. Thomas Giesen
Day of disputation: 17. January 2024

Kassel, August 2023

ABSTRACT

Chiral molecules are life's building blocks, making the study of their ultrafast processes a pursuit across various fundamental research fields. The results presented in this dissertation contain methodological, technical and scientific advancements that pave the way for future time-resolved, site-specific investigations into chiral photochemistry of randomly orientated molecules, using photoelectron circular dichroism and free-electron lasers. The high-repetition-rate free-electron lasers EuXFEL and FLASH2 will soon deliver undulator-based circularly polarized pulses, opening new avenues for chiral studies. The EuXFEL's instrumentation and applicability for chiral studies are presented based on the first performed experiments at the SQS endstation. The ultrafast spectroscopy technique of velocity map imaging and its suitability to measure the angular distribution of photoelectrons and ions in experiments targeting ultrafast dynamics is presented in detail. The double-sided velocity map imaging spectrometer, which was built and commissioned in the frame of this work, is presented, including technical details, and its simulated and experimentally retrieved performance. Inside into a performed study combining free-electron lasers and double-sided velocity map imaging spectroscopy, in the light of chiral perspectives, is given via the performed and here-presented experiment at FLASH1. Here, highly intense XUV pulses 63 eV and 75 eV, addressing the neutral and singly charged iodine 4d edge respectively, were used to probe the optical laser-induced fragmentation of the prototypical chiral molecule 1-iodo-2-methyl-butane ($C_5H_{11}I$) in a pump-probe scheme using 267 nm and 800 nm pulses. For charged Coulombic interaction of dissociating photofragments, the optical-laser-pump FEL-probe scans revealed that the molecule dissociates significantly slower with an 800 nm pump than with a 267 nm pump. The results show substantial wavelength and intensity dependence for the dissociation dynamics of this prototypical chiral molecule. In addition, electron-ion partial covariance imaging was demonstrated and enabled isolating the I 4d atomic and molecular levels. The outcomes of this dissertation provide a basis for future time-resolving investigations of chiral systems using free-electron lasers.

KURZFASSUNG

Chirale Moleküle sind essenzielle Bausteine des Lebens und die Untersuchung ihrer ultraschnellen Prozesse ist ein weitverbreiteter Forschungsschwerpunkt verschiedenster Grundlagenforschungsbereiche. Die in dieser Dissertation präsentierten Ergebnisse beinhalten methodologische, technische und wissenschaftliche Fortschritte, die den Weg für zukünftige zeitlich aufgelöste und ortsspezifische Untersuchungen der Photochemie von zufällig orientierten chiralen Molekülen ebnen. Methodologisch sollen der Photoelektronen-Zirkulardichroismus und Freie-Elektronen-Laser angewandt werden. Die in Lichtpulsen hoch wiederholende Freie-Elektronen-Laser EuXFEL und FLASH2 werden in Kürze zirkular polarisierte Pulse mittels Undulatoren bereitstellen. Mit der Bereitstellung dieses Lichtes werden neue Möglichkeiten für chirale Studien eröffnet. Die Instrumentierung des EuXFELs und Anwendbarkeit für chirale Studien werden anhand der ersten durchgeführten Experimenten an der SQS-Endstation vorgestellt. Die ultraschnelle Velocity-Map-Imaging Spektroskopietechnik und die Eignung zur Messung der Winkelverteilung von Photoelektronen und Ionen, die aus den Experimenten zur Untersuchung ultraschneller Dynamiken stammen, wird detailliert erläutert. Das doppelseitige Velocity-Map-Imaging Spektrometer, welches im Rahmen dieses Projektes gebaut und in Betrieb genommen wurde, wird vorgestellt, einschließlich technischer Details, sowie der simulierten und experimentell ermittelten Leistung. Einblicke in eine durchgeführte Studie, die Freie-Elektronen-Laser und doppelseitige Velocity-Map-Imaging Spektroskopie im Lichte chiraler Studienperspektiven kombiniert, werden anhand des hier vorgestellten Experimentes an FLASH1 gegeben. Dabei wurden hochintensive XUV-Pulse mit 63 eV und 75 eV, die die neutrale und einfach positiv geladene Jod-4d-Kante adressieren, verwendet, um die durch optische Laser induzierte Fragmentierung des prototypischen chiralen Moleküls 1-iodo-2-methyl-butan ($C_5H_{11}I$) in einem Pump-Probe-Schema mit 267 nm und 800 nm Pulsen zu untersuchen. Für die geladene Coulomb-Wechselwirkung von dissoziierenden Photofragmenten zeigen die optischen Laser-Pump-FEL-Probe-Scans, dass das Molekül mit einem 800 nm Laser deutlich langsamer dissoziiert als mit einem 267 nm Laser. Die Ergebnisse zeigen eine erhebliche Wellenlängen- und Intensitätsabhängigkeit für die Dissoziationsdynamik dieses prototypischen chiralen Moleküls. Ebenso wurde die Elektron-Ion-Teilkovarianz-Bildgebung demonstriert, welche die Isolierung der I 4d-atomaren und molekularen Niveaus ermöglichte. Die Ergebnisse dieser Dissertation liefern die Basis für zukünftige zeitaufgelöste Untersuchungen chiraler Systeme mittels Freie-Elektronen-Lasern.

никад не заборави одакле си

Contents

Chapter One

Introduction

On December 14, 1900, a significant milestone in the history of physics took place with the birth of quantum theory. Max Planck derived the law for black body radiation and postulated quanta of energy [1]. It was the start of modern physics. Throughout the following century, tremendous advancements occurred in the field of atomic and molecular physics.

However, even for the pioneers and brilliant physicists of subsequent years, understanding quantum theory proved to be a challenging task. In 1965, Richard Feynman famously stated, "I think it is safe to say that no one understands quantum mechanics" [2]. Enrico Fermi once confessed his confusion on the subject, saying, "Before I came here, I was confused about this subject. Having listened to your lecture, I am still confused. But on a higher level" [3]. Or Max Born, who wrote in a letter to Einstein that "the quanta are really a hopeless mess" [4].

Despite the difficulties, the necessity and inevitability of quantum theory were undeniable. In 1913, the Bohr model was invented [5], explaining the stability of atoms by postulating electron orbits around a dense nucleus. Classical physics failed to account for this stability, as a classical electron would continuously emit electromagnetic waves, losing energy and collapsing into the inner part of the atom. Consequently, the exploration of microscopic objects like atoms and molecules became feasible only through the lens of quantum physics.

At the present day, over a century later, significant progress has been made in the development of techniques that allow for the control of several degrees of freedom of atoms and molecules. These advancements have made it feasible to investigate these entities using various measurement methods. The field of atomic, molecular, and optical physics encompasses a vast array of diverse subfields, making it impossible to fully encapsulate its breadth within a single book, article, or thesis.

This work provides insights into the investigation of atoms and molecules when exposed to light of different wavelengths, which induces changes in their electronic structures and dynamical processes. These changes can lead to various physical processes such as photoexcitation, photoionization, or photodissociation of the illuminated sample. By analyzing the angular distribution and energy of the emitted photoelectrons and ions, valuable information about the interaction process can be extracted. The primary objective of such experiments is to decipher the structure and properties of the atom or molecule. Spectroscopic measurement techniques are commonly employed to detect the photofragments resulting from the interaction between light and matter. These experiments often involve the use of isolated atoms or molecules in the gas phase to facilitate controlled and precise observations.

Chirality [6], which plays a crucial role in the formation of life on Earth, holds significant importance across various research fields. Nonetheless, there are still many fundamental aspects of molecular chirality that remain not fully comprehended, here is one example of many open questions: how do chiral molecules undergo ultrafast conformational changes or transitions during photochemical reactions? Recognizing and characterizing chiral molecules and understanding the underlying fundamental chemical and physical processes in chiral systems are relevant pursuits in many research fields.

By using different light sources and adequate spectroscopic techniques, several relevant excitation regions in terms of energy, intensity, and temporal resolution, can be addressed and so the entire molecular quantum system consisting of electrons and atomic nuclei can be encompassed. Such a collaborative effort is for example followed by the DFG-funded CRC 1319 ELCH (Extreme light for sensing and driving molecular chirality) [7, 8], aiming with several research projects to make progress in: 1. understanding chirality on a single-molecule level, 2. determination of enantiomeric excess, 3. advancing the instrumentation, 4. getting the direct absolute configuration of enantiomers, 5. performance of fundamental physics experiments and 6. purification of enantiomers.

The work presented here focuses on the fundamental physical processes of single chiral molecules studied via free-electron lasers within the scientific agenda of the A4 project [9] of the CRC ELCH. Such chiral studies utilizing circularly polarized light from free-electron lasers, which generate ultraintense and ultrashort pulses, have opened up new avenues for exploring transient, time-resolved, and non-linear chirality phenomena from specific atomic observer sites. Time-resolved photoelectron circular dichroism spectroscopy is the method of choice for this work. It is the detection of the forward-backward asymmetry in the electron angular distribution at different times during the ultrafast process of interest. These different probing times are interconnected, with the distance between the probe-photoelectron emission site and the chiral center. Such experiments can provide valuable insights into the evolution

of molecular transformations, such as the transformation from chiral to achiral fragments, for example, during the dissociation of the molecule induced by optical laser pulses and probed via photoionizing free-electron laser pulses. Therefore, double-sided velocity map imaging spectrometers have been employed in this work to capture the angular momentum and energy of electrons and cations generated from noble gases or (chiral) halogen-alkanes following exposure to extreme light sources. The utilization of double-sided velocity map imaging spectrometers in conjunction with free-electron lasers will offer the potentially required technology for the tracking and analysis of electron behavior with remarkable precision and temporal resolution.

In the upcoming chapters, a short exploration of the aforementioned physical processes will be provided. Chapter 2 delves into the fundamental principles of matter, light-matter interaction, and the investigation of gas-phase chiral molecules in the light of time-resolved photoelectron circular dichroism as a tool for sensing chirality after ionization via circularly polarized light from free-electron lasers. Moving forward to Chapter 3, it will showcase a series of experiments conducted during the early operation phase of the Small Quantum Systems scientific instrument at European XFEL in Hamburg/Schenefeld Germany. Chapter 4, provides an in-depth exploration of double-sided velocity map imaging spectrometers. A key objective of this work was the design improvement and complete build-up of a spectrometer for the study of chiral dynamics at free-electron lasers. This chapter covers the new design, corresponding simulations, and the results obtained from the commissioning of this spectrometer using the Metrology Light Source in Berlin. Chapter 5 gives an extensive insight into a specifically performed study conducted on a prototypical chiral molecule, namely 1-iodo-2-methyl-butane, using FLASH1 the free-electron laser in Hamburg. Finally, Chapter 6 concludes the scientific results presented in this PhD thesis and provides insight into possible future studies.

Chapter Two

Basic Concepts

2.1 Atoms, Molecules, and Chirality of Life

Atoms and molecules are the fundamental building blocks of life. Atoms consist of a nucleus containing protons and neutrons, surrounded by a cloud of electrons orbiting the nucleus [10]. The number of protons defines the element, while the arrangement of electrons determines the atom's chemical behavior. The electronic structure governs how atoms interact, form bonds, and undergo chemical reactions. Molecules are formed when two or more atoms, from the same or different elements, chemically combine. The atoms within a molecule are held together by chemical bonds. By studying the atom's and molecule's electronic structure, valuable insights into the behavior of matter at the atomic and subatomic scales can be gained. One method to investigate this is by illuminating the target with light, allowing for the study of various phenomena.

This work puts particular emphasis on the study of chiral molecules with free-electron lasers (FELs) and establishes a methodological and spectroscopic foundation for investigating these systems. Chiral molecules exist in two distinct forms, known as enantiomers, which exhibit a right- or left-handedness analogous to human hands [11]. They possess a non-superimposable mirror-image relationship while having the same molecular formula and connectivity of atoms. Their molecular chirality stems from the asymmetric arrangement of atoms within the molecule, resulting in differences in their spatial orientation (visualized in Figure 2.1). Furthermore, they are characterized by identical chemical properties in an achiral environment but can exhibit different interactions with other chiral objects (molecules or helical light) and in chiral environments. There are few conventions for naming, for example, the mostly used one is the R/S system, which involves assigning priorities to substituents around a chiral center (usually a carbon atom) based on the Cahn-Ingold-Prelog priority rules, and then determining the configuration as either clock-

wise (R) or anticlockwise (S) [12]. Another convention is the D/L (aberrations from Latin: dexter for right and laevus for left) system, invented by Emil Fischer [13], which is commonly used for naming enantiomers of sugars and certain natural products. It is based on the orientation of the hydroxyl group on the chiral center, farthest from the carbonyl group. The enantiomer with the hydroxyl group on the left side is designated as (L)-enantiomer, and the one with the hydroxyl group on the right side is designated as (D)-enantiomer. In addition, the Letter S/R or D/L is accompanied by a (+) or (-), which refers to the optical activity after the irradiation with plane-polarized light. This phenomenon rotates the plane of the light. The enantiomer that rotates the light clockwise is designated as (+)-enantiomer (dextrorotary), and the one that rotates it counterclockwise is designated as (-)-enantiomer (levorotary).

Chirality is ubiquitous in life, and it can be found in various aspects of biological systems. It exists a homochirality in terrestrial life [14], which refers to the preference for one handedness. Two examples are the L-amino acids, which are the building blocks of proteins, and, nucleic acids, such as the DNA (right-handed) and RNA (left-handed). Thus, as a consequence also the interaction of living organisms with their surrounding is enantioselective, for instance affecting the odor perception, taste, and the effect of most pharmaceutical drugs. Although many examples of chirality can be observed, many fundamental questions are still unanswered. The origin of homochirality remains still unclear and is closely interconnected with the parity violation, leading to an energy difference of the enantiomers and represents an intersection of fundamental physics and the properties of chiral systems. The parity-violation effects in chiral molecules so far are only theoretically studied and not yet experimentally confirmed ([15] and references therein).

Enantiomers can typically and in practical applications only be distinguished through their interaction with a chiral object, for example circularly polarized light. The absorption of such light, if the photon energy is high enough, can result in the ejection of photoelectrons, either in the forward or backward direction regarding the light propagation direction, depending on the handedness of the enantiomer or the light helicity. This phenomenon is known as photoelectron circular dichroism (PECD) [16]. To investigate scientific inquiries pertaining to ultrafast structural changes in chiroptically sensitive systems, the utilization of ultrashort light pulses is indispensable. Combining the chiral discriminator technique of PECD, a sensitive observable that exhibits a significant modulation in the signal during changes in the electronic molecular structure, proves to be enticing and will be further elaborated in detail in Section 2.5.

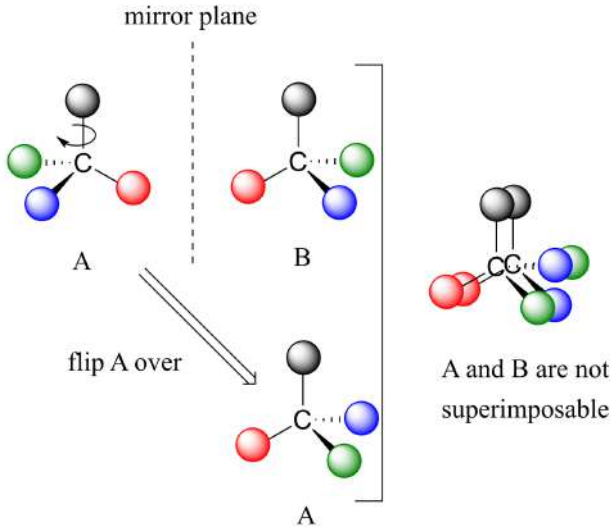

Figure 2.1: Sketch of a chiral molecule consisting of 5 atoms, including one Carbon atom, representing the chiral center, and four distinct atoms colored black, red, blue, and green. The enantiomers A and B are mirror images of each other and are non-superimposable. Figure adapted from [17].

2.2 Light-Atom Interaction

Photoionization and Decay Processes

The irradiation of an atom with photons can induce different processes, which appearance depends on the incident energy of the photons. The relevant processes for spectroscopic purposes will be elaborated in the following. To address outer shell electrons, thus in the valance orbitals, photon energies of a few tens of electron volts (eV) are required. Whereas, hundreds of electron volts are needed for intermediate shells in heavy atoms [18]. Thus, in the frame of this work, which focuses on probing the electronic structure of the target of interest and measures spectroscopically the observables created after the light-matter interaction, extreme ultraviolet (XUV) and soft X-rays are utilized, which range to photon energies of maximum 10 keV, where the photoelectric effect [19] is the most dominant process. Processes, that can be induced by higher photon energies, are out of the scope of this work and will not be presented here. The photoelectric effect can be described as follows: the incident photon is absorbed by the atom, and its energy (E_{ph}) is transferred either to the non-resonant ionization into the continuum (photoionization, $E_{ph}>E_{bin}$) or resonant excitation into a higher unoccupied state if energetically possible (photoexcitation, $E_{ph}\leq E_{bin}$) of an electron with the discrete binding energy E_{bin}. The photoionization process leads to the generation of photoelectrons,

whose kinetic energy can be described by the equation:

$$E_{kin} = E_{ph} - E_{bin} \tag{2.1}$$

with the photon energy defined by the product of the fundamental Planck constant h and the electromagnetic-wave frequency ν:

$$E_{ph} = h\nu \tag{2.2}$$

These processes are depicted in Figure 2.2(a), illustrating the outcomes depending on the energy of the incident photons. When UV photons interact with the system, valence electrons can be ejected via direct photoionization, leading to the formation of a singly charged atom (represented by the blue circle in steps 1 and 2). Alternatively, higher-energy photons can create inner-core holes (step 1, white background), resulting either in photoionization (step 2a) or photoexcitation (step 2b), both of which correspond to unstable states. As a result, a secondary process occurs to fill the hole with an electron from a higher orbital. This can take place through nonradiative resonant (also autoionization) decay (b), nonradiative non-resonant Auger-Meitner decay (c), or spontaneous X-ray emission known as fluorescence (d). In the case of (b) and (d), these processes lead to the formation of singly charged atoms, while (c) results in a doubly charged atom. The resonant Auger process can be further classified into participator and spectator transitions. In the participator scenario, the initially excited electron directly fills the hole during the subsequent Auger decay, while in the spectator scenario, the electron does not participate, as illustrated in Figure 2.2(b). In larger Z-systems, cascades of Auger-Meitner decays can occur, leading to the generation of multiply charged ions. The Auger-Meitner and fluorescence processes compete with each other. In the fluorescence process, a photon (E'_{ph}) is emitted, with its energy corresponding to the difference in binding energy between the two involved energy levels. In contrast, within the Auger-Meitner decay, the released energy is transferred through Coulomb interaction (indicated by the black dashed line and labeled as step 4) to another electron, which is then ionized into the continuum (step 5).

As visualized in Figure 2.3 the yield of these two processes depends on the photoionized electron shell and the atomic number (Z) of the atom [20–22]. The figure illustrates that the fluorescence yield increases with increasing Z and begins to dominate for electrons originating from the K-shell with atomic numbers greater than or equal to 30 (indicated by the dashed black line). For L-shell electrons, the Auger-Meitner effect dominates up to atomic numbers of $Z \leq 95$ (gray line). As for the M-shell (light gray line) and higher inner or intermediate shells, the fluorescence yield gets negligible. However, for higher charge states, accessible e.g. through non-linear studies at free-electron lasers, the fluorescence yield can even earlier surpass the Auger decay [23].

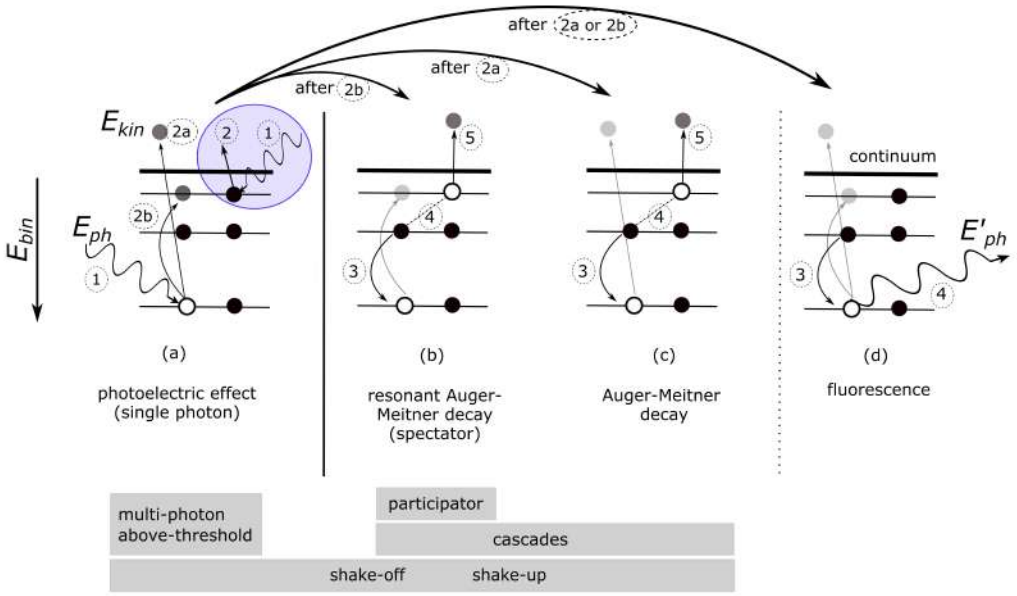

Figure 2.2: Schematic photon-electron interaction. Shown in (a) is the direct single-photon ionization occurring either in the valance shell (represented by the blue circle and steps 1 and 2) or in an inner shell (steps 1 and 2b), as well as photoexcitation (step 2a). The decay of the inner-shell hole can take place through non-resonant (b) or resonant (c) Auger decay, or x-ray emission (d). These processes can be accompanied by additional processes or achieved through alternative pathways. Among these, the most relevant ones are selected and depicted in the gray text boxes.

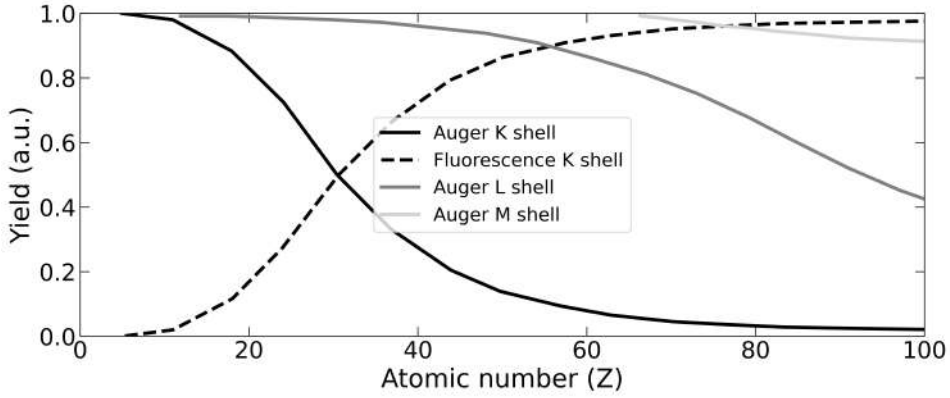

Figure 2.3: Yield for the Auger-Meitner effect (continuous lines) and the fluorescence yield (black dashed line) plotted as a function of the atomic number Z. The data is presented for the K-shell (black) and averaged over all L-shells and M-shells (gray and light gray, respectively). Figure adapted from [20, 21].

There are additional possibilities for the primary process of photoionization and the secondary Auger-Meitner process, which are not additionally illustrated in Figure 2.2 but annotated in the gray rectangles beneath each process. Photoionization or photoexcitation can be caused by the absorption of a single photon (as depicted in (a)), referred to as direct single-photon ionization, mostly studied using high-energy radiation from tabletop VUV and X-ray sources, synchrotrons or FELs. Instead of single-photon ionization, additional processes can occur for photon energies below the ionization threshold originating from intense pulsed laser sources e.g. optical lasers or FELs. Here, the atom interacts with multiple photons simultaneously, resulting in a sequential absorption of many photons, the so-called multi-photon ionization (MPI). Above-threshold ionization (ATI) is an extension of the MPI and occurs when an electron absorbs more photons than necessary to overcome the ionization threshold [24]. The via one of the above-mentioned processes ionized atom decays via a secondary mechanism as already introduced before. Fourth-generation light sources for example free-electron lasers, offer high photon energy, short pulse duration, and a large number of photons, which is achieved by a new technology applied within these light sources. These facilities generate synchrotron radiation, which is a type of electromagnetic radiation produced when charged particles, such as electrons, are accelerated to nearly the speed of light and are forced to travel in curved paths by magnetic fields, in the following elaborated in more detail. Consequently, at FELs, a sequence of inner-core holes can be created even before the relaxation through an Auger-Meitner decay. One example of such an application is the creation of double-core holes, which will be explored in more detail in Chapter 3.

Additional processes that can occur during primary photoionization and secondary Auger-Meitner decay involve electron correlations. These processes include the excitation of another electron into a higher unoccupied state (shake-up) or the ejection of another electron into the continuum (shake-off) [25]. These effects, resulting from electron correlations, cause a quantized decrease in the kinetic energy of the photoelectron created in step 2b and appear as "satellite lines" in the photoelectron spectra. It is important to note that there are further possible regimes of photoionization, such as strong-field ionization, that do not apply to the experiments presented in this work and are therefore not elaborated further. A broader overview of photoionization in the VUV and soft X-ray regime can be found elsewhere [26].

Atomic Orbitals

Each electron in an atom is characterized by a unique set of quantum numbers, namely n, l, m_l, s, m_s. These quantum numbers provide information about the energy, atomic orbital shape, orientation, and spin state of the electron. In Figure 2.2, the energy levels of the atom are represented by black horizon-

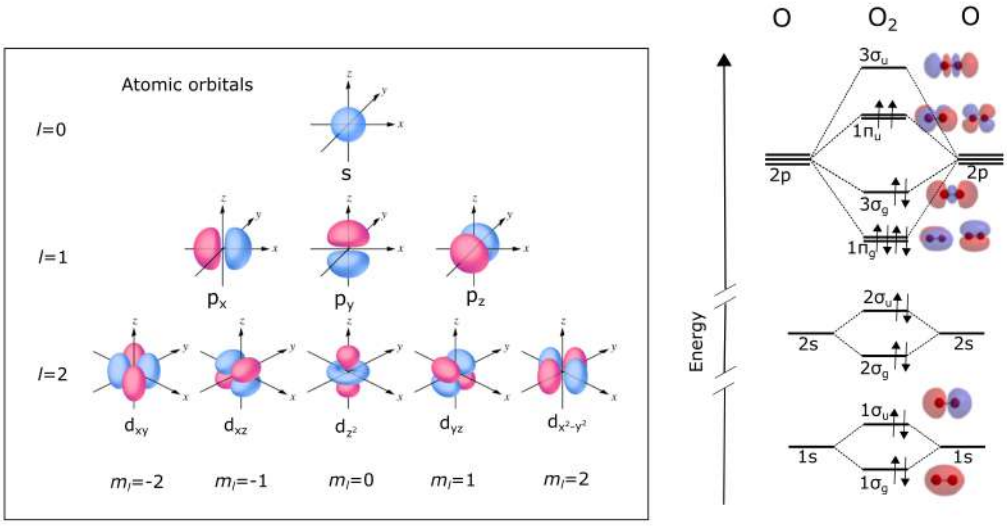

Figure 2.4: Left: Shape of the atomic orbitals including s, p, and d. Image adapted from [27]. Right: Molecular orbital diagram for O_2, containing bonding and antibonding molecular orbitals. Molecular orbitals taken from [28].

tal lines, which correspond to the three-dimensional shells containing atomic orbitals. The shells are labeled by the principal quantum number, n, taking values of n=1, 2, 3, 4 and so on, or represented by capital letters K, L, M, N, and so forth. Each shell consists of subshells called atomic orbitals (AO), which are regions of space around the nucleus where electrons are likely to be found. They provide a framework for understanding the distribution and behavior of electrons within atoms. The probability distribution of finding an electron in an AO is described by the wavefunction Ψ. The AOs are visualized in the black box on the left side of Figure 2.4. They exhibit different shapes, characterized by the azimuthal quantum number, l, which ranges from 0 to n-1, and is represented by the letters s, p, d, f, and so on (in alphabetic order excluding the letter j). The most common AO, s, p, and d, are visualized in Figure 2.4. The s orbital is spherical and centered around the nucleus. The p orbitals are dumbbell-shaped and come in three orientations (p_x, p_y, and p_z). The d orbitals have more complex shapes, and all the following orbitals are even more intricate. An electron in an atomic orbital is further defined by its magnetic quantum number m_l, which takes values from 0 to $\pm l$, representing the orientation of AO for the corresponding subshell l. The spin state of the electron is determined by the quantum numbers s and m_s, where m_s can be $+s$ or $-s$, with s=$+\frac{1}{2}$ fixed for electrons. This results in $m_s = +\frac{1}{2}$ (spin up) and $m_s = -\frac{1}{2}$ (spin down).

Electrons fill up the atomic orbitals following the Aufbau principle [10], which states that they occupy orbitals in order of increasing energy. The occupation sequence is 1s 2s 2p 3s 3p 4s 3d 4p 5s 4d 5p, 4f, 5d, 6s, 6p, 5f, 6d,

7s, 7p (including all orbitals up to the last element in the periodic table with Z=118 [29]) with a maximum of two electrons with opposite spin in each atomic orbital, obeying the Pauli exclusion principle [30]. The electron configuration of an atom is then presented by the arrangement of electrons, such as $1s^2$ $2s^2$ $2p^6$ $3s^2$ $3p^6$ $4s^2$ $3d^{10}$ $4p^5$, which corresponds to Bromine (Z=35).

To calculate the wavefunction of a one-electron system, which contains the dynamical information about the electron, the time-dependent Schrödinger equation needs to be used, as expressed in Equation (2.3), where $\hat{H}$ is the Hamiltonian operator defined in Equation (2.4), incorporating the kinetic energy and potential energy terms [31].

$$\hat{H}\ \Psi(r,t) = i\hbar\frac{\partial}{\partial t}\Psi(r,t) \tag{2.3}$$

$$\hat{H} = -\frac{\hbar}{2}\nabla^2 + V(r,t) \tag{2.4}$$

Further details regarding the calculation can be found in references, such as [32]. In these calculations, the Born-Oppenheimer approximation [33] is a crucial concept that is employed. This approximation considers the electronic and nuclear motions as separate entities due to the significant difference in their masses. By treating them independently, the calculations become more manageable, particularly for systems with multiple electrons.

2.3 Light-Molecule Interaction

Molecules are in some ways more complex compared to atoms, and in addition to pure electronic transitions, other processes such as vibration and rotation can be induced. The study of vibrational and rotational spectra is an additional big branch in the research field of molecular physics and is beyond the scope of this work, but generally, these states can be studied for example via the usage of near-infrared light and microwaves, respectively [34].

Light-molecule interactions can initiate chemical reactions through photochemical processes. A process closely related to this work is photodissociation, where photons provide the necessary energy to break chemical bonds, resulting in the formation of two or more fragments. Photodissociation, also known as photolysis or photofragmentation, occurs when the molecule is excited into a higher unbound electronic state, which lacks a minimum in the potential energy curve. Figure 2.5 provides a visualization of the various kinds of potential energy curves calculated for the chiral molecule, 1-iodo-2-methylbutane, investigated in Chapter 5. Photodissociation is a crucial process in

the restructuring of matter and is of great interest in biological, chemical, and physical sciences. The time-resolved investigation of photodissociation on atomic scales, specifically with element or site-specificity, provides valuable insights into various dynamics and pathways, including molecular fragmentation, radiation damage, chemical bond-breaking, and light-matter interaction. These processes evolve to a large extent on femtosecond timescales and require pulsed light sources with durations of exposure in the order of the dynamics of interest or shorter. Ultrafast spectroscopic techniques, such as velocity map imaging (VMI), are employed to access these dynamics directly. Short-wavelength FELs and femtosecond optical lasers are particularly noteworthy in this regard. Their ultrashort and ultrabright pulses allow studying photodissociation phenomena. Within this work, the wavelength-dependent photodissociation of a chiral molecule was studied using circularly polarized FEL light and a VMI. Typically, such studies involve the use of a laser inducing the photodissociation, followed by the ionization of the fragments using a second probe laser for state-selective detection (further details will be provided in the subsequent sections).

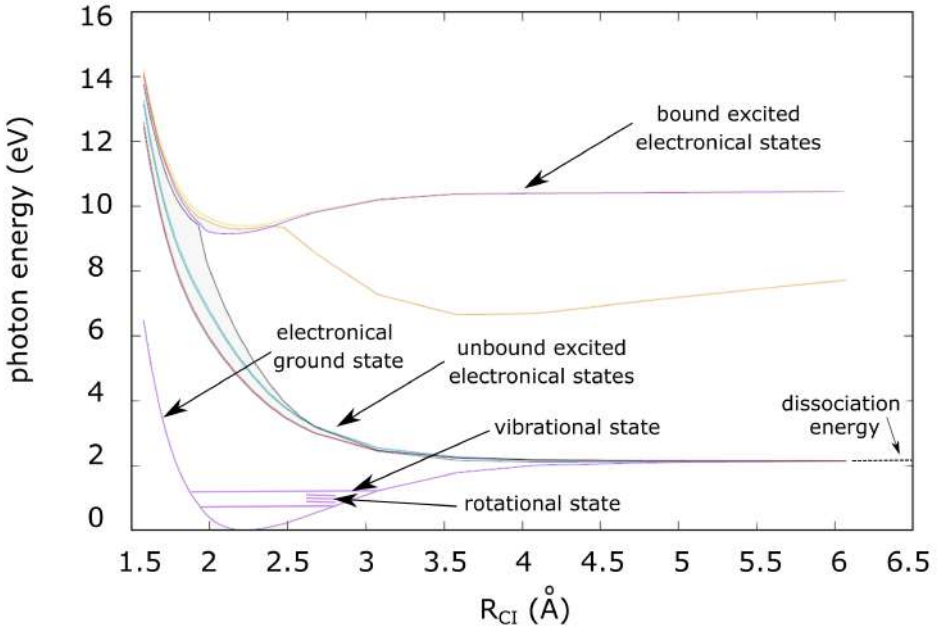

Figure 2.5: Potential energy curves calculated for the internuclear distance between carbon (C) and iodine (I) within the molecule 1-iodo-2-methyl-butane [35]. Visualized are the electronic ground state, the bound and unbound excited electronical states. Vibrational and rotational states were added graphically only for exemplary visualization.

Molecular Orbital Theory

Molecular systems, unlike individual atoms, exhibit a complex electronic structure that is influenced by the presence of neighboring atoms. To describe molecular orbitals, the Linear Combination of Atomic Orbitals (LCAO) theory was introduced by John Lennard-Jones in 1929 [36]. This theory approximates molecular orbitals (MO) as linear combinations of atomic orbitals. The development of MO theory was further advanced by Mulliken [37] and Hund [38], who made significant contributions to its understanding.

Molecular orbitals can be categorized as bonding, antibonding, or nonbonding orbitals [39]. Bonding orbitals (gerade, denoted as g) result from constructive interference of atomic orbitals and have lower energy than the original atomic orbitals. They promote electron density between the nuclei, contributing to the stability of the molecule. In contrast, antibonding orbitals (ungerade, denoted as u) arise from destructive interference of atomic orbitals and possess higher energy than the original atomic orbitals. These orbitals feature a nodal plane between the nuclei, which leads to a destabilizing effect. Nonbonding orbitals predominantly localize electrons on specific atoms and do not significantly contribute to bonding. Figure 2.4 illustrates on the right side the molecular orbital diagram for a diatomic molecule, O_2, displaying the ground state configuration $(1\sigma_g)^2(1\sigma_u)^2(2\sigma_g)^2(2\sigma_u)^2(1\pi_g)^4(3\sigma_g)^2(1\pi_u)^2$, following the Aufbau principle for molecules [40].

To calculate the electronic wavefunction and thus get information about shapes, energies, structure, or even the reactivity of molecules, computational methods are required due to the complexity of the system. Two commonly used approximation methods are the Hartree-Fock method [41, 42] and the Density functional theory [43–45], although they are not discussed in detail here. The choice of method depends on factors, such as size and complexity of the molecule, desired level of accuracy, available computational resources, and specific properties of interest.

In general, valence orbitals play a crucial role in molecular bonding, as they are delocalized over multiple atoms, and their electrons exhibit a higher degree of freedom throughout the molecule. On the other hand, core orbitals are localized on each atom and are often studied because they offer a very distinct view of the evolving system from specific observer sites. The reason why, the PECD from core holes is addressed in the frame of this work. These core orbitals can typically be described as atomic orbitals, albeit with a shift to lower binding energies. This shift is known as the chemical shift, which was also observed in the experimental data presented in Section 5.7.

Cross Section and Angular Distribution

The probability of the photon-electron interaction in a given system is described by the total photoabsorption cross section σ_T. This cross section represents the ratio of the absorbing area of the target to the total area of the target and is typically measured in units such as barn or Mbarn. The value of σ_T depends on the electronic structure of the atom and the energy of the incident photon. Generally, σ_T decreases as the photon energy increases and tends to be higher for atoms with larger atomic numbers. This cross section is specific to the atom and varies across different electronic shells. Photon energies provided by storage rings and FELs can be finely tuned over a wide range, making them suitable for selectively ionizing specific electronic shells in free atoms or bound atoms in molecules. This tunability enables element-specific photoabsorption studies.

$$I_{(p)}(\theta) = \frac{d\sigma^{(p)}(\theta)}{d\Omega} = \frac{\sigma_T}{4\pi} \sum_L b_L{}^{(p)} P_L(cos(\theta)) \tag{2.5}$$

In gas-phase experiments, the angular distributions of emitted photoelectrons in the laboratory frame are given by the differential cross section presented in Equation (2.5). It is the derivative of the partial cross section regarding the solid angle Ω [46, 47] and a measure of the total number of photoelectrons that come out in the solid angle dΩ. For atoms/molecules ionized by a single-photon and 100 % linearly polarized light ($p = 0$, $b_1^{(0)} = 0$, $b_2^{(0)} = \beta_2$), the following equation is valid within the dipole approximation:

$$\frac{d\sigma^{(0)}(\theta)}{d\Omega} = \frac{\sigma_T}{4\pi} \cdot [1 + \beta_2 P_2(cos\theta)] \tag{2.6}$$

if the ionization occurs via the absorption of one circularly polarized or unpolarized photon with helicity p on an achiral target ($p = \pm 1$, $b_1^{(\pm)} = 0$, $b_2^{(\pm)} = \pm\frac{1}{2}\beta_2$), the following equation is valid:

$$\frac{d\sigma^{\pm}(\Theta)}{d\Omega} = \frac{\sigma_T}{4\pi} \cdot \left[1 - \frac{\beta_2}{2} P_2(cos\Theta)\right] \tag{2.7}$$

with $P_2(x)=\frac{1}{2}(3x^2 - 1)$ the second Legendre polynomial, p=$\pm$1 the light's helicity, θ polar angle between the direction (momentum vector $\vec{p}$) of the emitted photoelectron and the polarization of the incident light (electric vector ϵ), Θ polar angle between the light direction (propagation vector $\vec{k}$) and photoelectron momentum $\vec{p}$, and β_2 is the asymmetry/anisotropy parameter, ranging with continuous values from $\beta_2 \in$ [-1,2]. β_2 characterizes the angular distribu-

tion of photoelectrons. An isotropic angular distribution corresponds to β_2=0. The parameters are visualized in Figure 2.6 for the values -2, 1, 0 and -1. The mathematical derivation from the Equation (2.6) to (2.7) can be found in further readings [48]. The general equation for the beta parameter is presented in the work published by Cooper and Zare [46].

For chiral molecules the following equation is valid: [16, 49–51]:

$$\frac{d\sigma^{\pm}(\Theta)}{d\Omega} = \frac{\sigma_T}{4\pi} \cdot \left[1 \pm \beta_1 P_1(cos\Theta) - \frac{\beta_2}{2} P_2(cos\Theta)\right] \tag{2.8}$$

with β_1 the additional dichroic parameter ($b_1^{(\pm)} = \pm\beta_1$), which is non-zero due to symmetry breaking. This parameter describes PECD in chiral molecules and is in comparison to the two cases presented in Equations (2.6) and (2.7) not zero and P_L (L=1,2) are the first two Legendre polynomials.

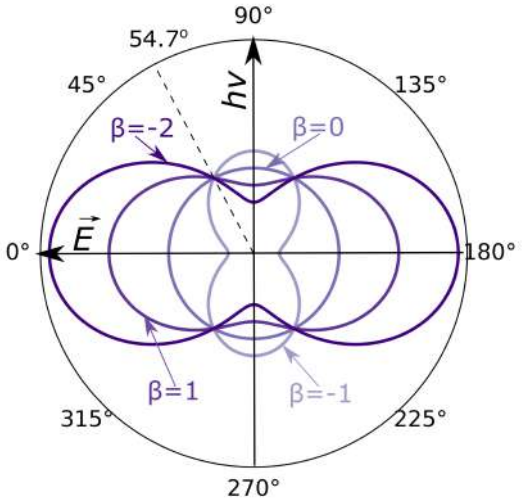

Figure 2.6: 2-dimensional visualization of the anisotropy parameter (β_2), with values of -1, 0, 1 and 2. The photon beam ($h\nu$) is depicted vertically, while the horizontal axis represents the electric field vector $\vec{E}$. A dashed line indicates the magic angle at 54.7 °, which remains constant independent of the value of β_2.

The equations presented above are derived under the assumption of pure dipole contributions, which is a simplified approximation for the analysis of light-matter interactions. In the dipole approximation, the atom or molecule is treated as a small-sized or point-like object possessing an electric dipole moment. This approximation is valid when the size of the atom or molecule is much smaller than the wavelength of the incident radiation, allowing the electric field to be considered constant over the extent of the atom or molecule. Initially, it was believed that the dipole approximation is valid up

to several hundred electron volts. However, experimental observations [52, 53] have revealed that even at lower photon energies within the range of several tens to hundreds of eV, deviations from the dipole approximation can occur. These deviations, known as non-dipole effects, arise from higher-order contributions and more intricate characteristics of the system [54, 55]. To account for these non-dipole effects, Equation (2.6) can be extended by incorporating first-order non-dipole corrections. This extension is typically sufficient to describe light-matter interactions up to the soft X-ray regime.

$$\frac{d\sigma^{(0)}(\theta)}{d\Omega} = \frac{\sigma_T}{4\pi} \cdot [1 + \beta_2 P_2(cos\theta) + (\delta + \gamma cos^2\theta) sin\theta cos\phi] \tag{2.9}$$

The non-dipole effects in light-matter interactions can be described by two non-dipole asymmetry parameters, δ and γ, which introduce a forward/backward asymmetry in the emission of photoelectrons. To mitigate the influence of first-order non-dipole effects, measurements are often conducted in the dipole plane, which corresponds to the plane perpendicular to the photon beam. By performing measurements in this plane, the impact of first-order non-dipole effects is effectively eliminated. This enables the determination of the σ_T and β_2 parameters without interference from non-dipole terms. This consideration is important in the frame of PECD-based chirality studies to distinguish the experimentally observed asymmetries originating from PECD and non-dipole effects. Even small non-dipole contributions can negatively influence the data interpretation of PECD studies.

2.4 Free-Electron Lasers

FELs [56, 57] have brought a revolution in the realm of photon science, since their presented principle by Madey in 1971 [58]. These cutting-edge lasers serve as an immensely powerful tool for investigating atomic and molecular systems with unparalleled time resolution combined with exceptional high intensities. Large-scale FELs aim usually to produce extremely intense radiation and are therefore operated in a so-called high-gain regime [59], which are exclusively elaborated within this work. With their capability to generate ultrashort pulses in the order of femtoseconds or even attoseconds, FELs are ideal for conducting photoionization experiments and thus probing the electronic structure with exceptional temporal and spatial resolution. Moreover, FELs generate high photon fluxes and coherent light, while offering extensive tunability across a wide range of photon energies. Few FELs, such as FERMI [60] in Italy, FLASH [61, 62] and soon European XFEL (EuXFEL) [63, 64] in Germany, even provide control over polarization, a crucial aspect when studying the ultrafast dynamics

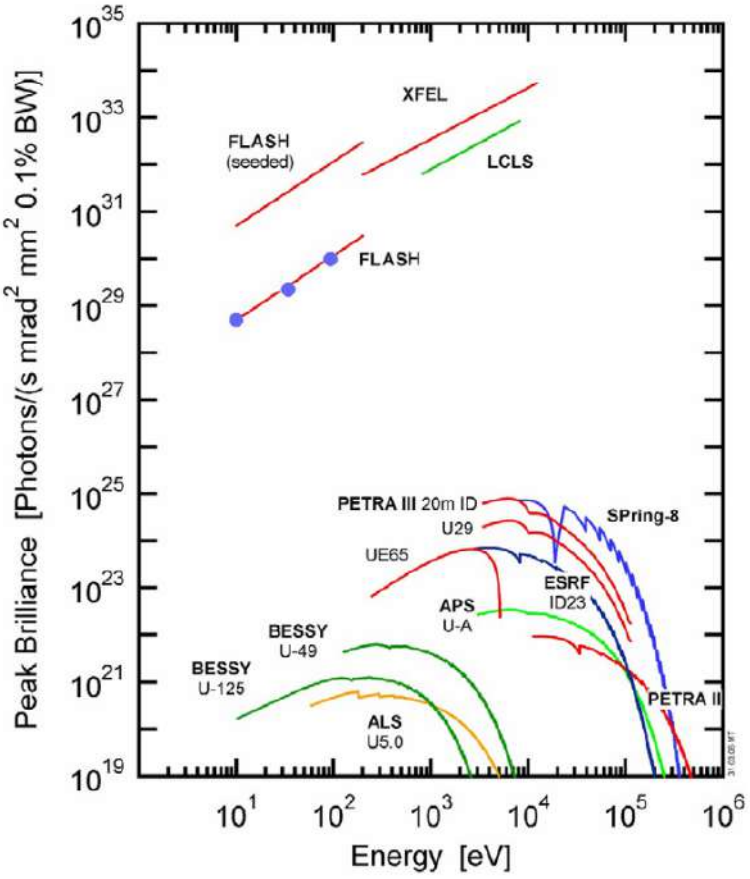

Figure 2.7: Peak brilliance of storage rings and FELs, with the most brilliant source EuXFEL, in the image annotated as XFEL. Image taken from [65].

of chiral systems. Notably, FELs possess outstanding beam quality, making them the brightest available light source in modern times. Brightness, also known as brilliance, is a physical quality factor and is defined by the number of photons per second, hence the flux (F) divided by the beam's divergence (θ), size (σ), and the energy bandwidth ($\frac{\Delta\lambda}{\lambda}$):

$$B = \frac{F}{\theta \cdot \sigma \cdot \frac{\Delta\lambda}{\lambda}} \tag{2.10}$$

Figure 2.7 presents the peak brilliance of today's used and state-of-the-art light sources, the storage rings and FELs, with the highest peak brilliance available at EuXFEL ($B \approx 10^{34}$).

FELs utilize high-energy electron beams passing through magnetic undulators to generate coherent, intense X-ray pulses. In a nutshell, FELs function as follows: Electrons are generated through processes like thermionic cathodes or photoemission. These electrons are then pre-accelerated and injected

into the linear accelerator (LINAC) module, which can be based either on normal or super-conductivity (second technology enables MHz repetition machines as FLASH, EuXFEL and LCLS II [66]), where the electron beam is accelerated close to the speed of light using radiofrequency (RF) cavities. To create coherent light, the electron beam is bunched together into tightly packed bunches and should be characterized by high performance as low emittance, controlled energy modulation, well-defined and stable bunch shape, and a narrow energy spread.

The bunched electron beam, with almost the speed of light, passes through undulators [67, 68], which are magnetic devices with alternating poles (macroscopic periodicity of few centimeters, wavelength defined as λ_u) that cause the electrons due to the Lorentz force to oscillate transversally, resulting in the longitudinal emission (z-axis in Figure 2.8) of synchrotron radiation [69–72], characterized by the wavelength λ. The emission of these short wavelengths is only possible due to relativistic effects. The relativistic electrons see the undulator as a shrunken object, known as the Lorentz contraction. The emitted wavelength in the laboratory frame is further decreased by the Doppler shift. These two relativistic effects lead to the following equation:

$$\lambda \simeq \frac{\lambda_u}{2\gamma^2}\left(1 + \frac{{K_u}^2}{2}\right) \tag{2.11}$$

$$K_u = \left(\frac{eB_0P}{2\pi m_0 c}\right)^2 \tag{2.12}$$

with K_u the undulator parameter, which considers the reduction in the longitudinal velocity of an electron, defined by the elementary charge e, the magnetic field amplitude B_0, the undulator Period P, the electron mass m_e and the speed of light c. The undulator parameter is smaller than 1 for undulators. The desired wavelengths λ of a few Ångströms require γ-values (electron energy divided by its rest energy mc^2) of several thousand, which explains why the electrons are typically accelerated to high energies of several GeV. This explains furthermore the very long LINAC at FEL facilities, with up to almost 2 km, as the case for the EuXFEL, which is also capable of producing, for this work not relevant, hard X-rays. Generally, the wavelength can be tweaked by changing γ or the undulator parameter, lastly can be technically realized by changing the undulator gap [73].

At the beginning of the undulator section, randomly emitted radiation interacts with the co-propagating electron beam (energy modulation), producing the ponderomotive force, which pushes the electrons either into the forward or backward direction (density modulation). It leads to a microbunching of the electrons into the longitudinal direction and a separation of λ between

each electron microbunch. The self-amplified spontaneous emission (SASE) process is triggered, where the radiation from one electron bunch stimulates further emission from neighboring bunches, leading (based on interference) to exponential optical amplification, which is a function of the distance z along the undulator. The general conditions under which an FEL efficiently generates coherent radiation are described by the Madey Theorem [58]. However, this amplification saturates when the electrons are completely microbunched. This is the reason why high-gain FELs facilities, presented here, possess long undulator sections, up to 200 m, as the EuXFEL, to ensure the full exploitation of the optical amplification mechanism and to produce high-intensity FEL pulses. Previously mentioned subprocesses are visualized in Figure 2.8(a)-(e). The process of michrobunching and SASE of high-gain FELs is the key difference to the standard laser, which amplification is caused by stimulated emission and population inversion [74].

Finally, it is important to note that the behavior of SASE FEL radiation is characterized by its chaotic nature, which arises from the random emission of undulator radiation. This stochastic behavior is a result of the spontaneous emission process in the undulator. The individual SASE FEL pulses differ in their intensity, temporal structure and spectral distribution, from shot to shot [75]. An overview of all available FELs worldwide and their different specifications can be found in further readings ([76] and references therein).

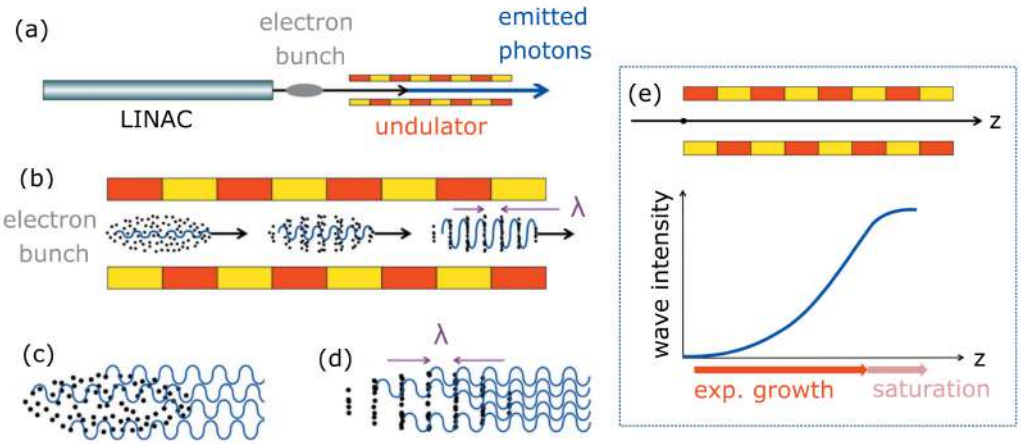

Figure 2.8: (a) LINAC creating the electron bunch passing the undulator modules and emitting the photons, (b) microbunching of the electron bunch along the propagation. Michrobunches separated by one wavelength, (c) destructive interference of electron bunch, (d) constructive interference of michrobunched electrons, and (e) wave intensity as a function of the undulator length for high-gain FELs. Figure adapted from [72].

The electron beam is not reused and is safely disposed of in an electron beam block. Whereas, the amplified radiation, in the form of X-rays or ultraviolet FEL pulses, is directed through the photon beamlines, under ultra-high vacuum (UHV) conditions, towards experimental setups. During the FEL beam transport, several important manipulation and diagnostic tools are utilized to ensure the proper delivery of the FEL pulses to the target placed in the interaction region of the experimental chamber [77–79].

To monitor the FEL beam parameters, various non-destructive diagnostic tools (operated in parallel to the user experiments) are employed along the beamline. Gas Monitor Detectors (GMDs) [80, 81] provide information about the beam's properties, including its energy, intensity, and positioning. They can even measure these parameters on a pulse-resolved basis, which is necessary due to the chaotic nature of SASE-FEL pulses, elaborated also in detail in Section 5.4.1. Additionally, the Bunch Arrival Monitor (BAM) [82, 83] is used to precisely measure the pulse arrival time. This is particularly important for experiments that require precise synchronization with another pulsed light source such as an optical laser, a prerequisite for performing experiments in optical-pump FEL-probe schemes [84, 85]. Another important point is capturing the FEL beam profile. This is significant for excluding distortions on the wavefront and also helpful during the alignment of the beam, thus it's pointing. To monitor the wavefront, invasively scintillating screens, which convert the beam intensity into visible light, can be used. The emitted light is then captured by a camera and can be assessed and optimized. All the above-mentioned feedbacks are crucial for optimizing the beam parameters and ensuring that it meets the desired specifications. Recorded diagnostic data can also be furthermore helpful and used for post-analysis of the data, an indeed crucial step for the following discussed experiments presented in this work.

FEL pulses can be manipulated in various ways to meet specific experimental requirements. Some of them will be briefly mentioned here, following the photon beam path downstream to the experiment. The photon pulses can be directed to different beamlines realized by using long plane mirrors in grazing incidence [86], which are required for total external reflection due to the small wavelength of the X-rays and the very small critical angle. Larger angles than the critical angle for total external reflection would increase the probability of absorption, which can lead to heating or even damage to the mirror. Gas-filled attenuators [87, 88] are commonly used to significantly reduce the FEL pulse energy without modifying the accelerator parameters. They are filled with noble gases allowing to continuously and smoothly precisely adjust the X-ray intensity by "solely" changing the gas pressure. Apertures along the photon beamlines allow for the selective blocking or cutting of portions of the FEL beam. Fast shutters are employed to choose individual FEL pulses, particularly in experiments that require longer intervals between pulses. Under specific conditions, filter foils can be inserted to block unwanted wavelengths of

radiation from the FEL beam or to reduce the FEL intensity. Monochromators [89] are also utilized in some photon beamlines to isolate a specific wavelength of light and better energy resolution for a narrow range of wavelengths, but their use may lead to drawbacks such as reduced photon flux, and elongation of pulse duration. To focus the FEL pulses, toroidal [90], elliptical [91], or bendable mirrors [86, 92–95] are employed, ensuring precise control over the beam's spatial properties for focusing. All these manipulation techniques provide the flexibility to shape and control FEL pulses according to their specific experimental requirements.

Polarization

If the electron beam is perturbed in the undulators transversally only in one axis, the emitted FEL beam is linearly polarized. If the perturbation rotates, elliptically or circularly polarized light or even other related operational modes can be created, which requires different undulators. The novel APPLE X undulators [96, 97] offer these possibilities and will be soon commissioned at EuXFEL [98, 99]. They offer full and precise control of polarization, by controlling symmetrically the radial and the longitudinal movement of all magnetic arrays. Information about previous APPLE-type undulators can be found in further readings ([100] and references therein). FERMI is up-to-date the only FEL, which can deliver circularly polarized light created by undulators, which is realized via APPLE-II undulators [101]. FLASH2 will soon deliver undulator-based helical light by using the APPLE-III undulators [102]. Nonetheless, mirror-based polarizers are as well a suited intermediate option for several FEL facilities containing solely fixed gap undulators, up-to-date also still used at FLASH1 [103]. In the following are a few details presented regarding this technology, due to the usage of such circularly-polarized FEL pulses presented in the experiment in Chapter 5, which was conducted at FLASH1. Even though their performance is not comparable with the creation of circularly polarized FEL pulses via undulators, which are specifically designed to "provide circularly polarized X-rays with a very high degree of circular polarization while preserving characteristics unique to FELs such as high pulse energies and ultrashort pulses" [104]. Mirror-based polarizers are typically designed for a specific wavelength range. They can be limited in generating circularly polarized light across a broad spectral range. In addition, they attenuate the incoming light by reflecting only a specific polarization state. This results in a loss of photon intensity, which can be significant, particularly in the case of FELs that produce intense and short pulses. They also have fixed polarization properties and cannot be easily tuned or adjusted during experiments. Furthermore, they may introduce additional optical path lengths or unwanted dispersion effects, which can complicate the interpretation of time-resolved data or limit the achievable temporal resolution. And lastly, the most critical limitation in the light of chirality studies is their non-ideal polarization efficiency. They

can introduce unintended ellipticity or incomplete suppression of the undesired polarization state, leading to lower fidelity in generating circularly polarized light. This can impact the accuracy and reliability of chirality measurements and analysis and highlights the advantage of the undulator-based creation of circularly polarized light.

Pump-Probe Experiments

Pump-probe schemes at FELs [85] involve using two (or more) synchronized pulses and are mandatory for direct time-resolved studies. The pump pulse is used to excite, ionize or manipulate the sample under investigation, initiating a specific process or triggering a change in its properties. The probe pulse is then delayed and used to measure the resulting changes in the sample. By varying the delay between the two pulses, depending on the chosen pump-probe scheme this can be controlled externally or the time delay is already imprinted within the FEL pulse structure (specified below), it is possible to study the dynamics of the sample with high temporal resolution. The temporal resolution depends on the combined properties of the pulse duration and the precise control of the time delay between the pump and probe pulses. Three, for this work, relevant cases can be differentiated.

1. In the optical-pump FEL-probe experiments, an external laser source is used to generate the pump pulses, typically in the optical or infrared range [105, 106] (entries no. 11 and 17 in the author's publication list). The time delay between the pump and probe pulses is controlled externally. The synchronization between the pump and probe pulses is typically achieved using precise timing control. One common approach is to utilize a timing reference, such as an optical reference signal or an RF signal, which is distributed to both, the laser system generating the pump pulse and the FEL producing the probe pulse. The timing reference signal serves as a common time base, allowing for precise synchronization between the two pulses. It is important to note that achieving precise synchronization in such pump-probe experiments can be a complex and challenging task. It requires careful calibration and optimization of the timing systems to ensure accurate and stable synchronization [107–109].

2. In contrast, intra-SASE pump-probe experiments utilize the inherent characteristics of the SASE-FEL pulses as both the pump and probe pulses [110–114] (entries no. 8, 9, 10, 13, and 18 in the author's publication list). This allows for simultaneous pump and probe capabilities within the same pulse train without the need for an external laser source. Additionally, intra-SASE pump-probe experiments benefit from the inherent synchronization between the pump and probe pulses within the SASE pulse. The time delay between pump and probe pulses is of stochastical nature and can not be adjusted. Thus no pump-probe delay scans are performed as done in the optical-pump FEL-

probe scheme. The time delay is retrieved in post-analysis. Therefore the data is sorted and the time delays are afterward extracted.

3. Lastly, an additional FEL-unique scheme should be mentioned, the one-color or two-color FEL-pump FEL-probe scheme [115–117], which uses two FEL pulses either with the same photon energy or two different photon energies, respectively. The two-color scheme was utilized in the following-mentioned work by Ilchen et al. [118] (entry no. 12 in the author's publication list), the first performed experiment showing FEL-based PECD using the LCLS light source in California and in more detail presented in section 2.5. The generation of these schemes can be achieved by various approaches and includes a variety of technologies, and is out of the scope of this work. One possibility for example is that the electron beam is split into two in space and time separated electron beams, each directed through all undulator sections but lasing only in its own undulator section with different and optimized magnetic settings to produce the desired photon energy. The resulting FEL pulses are delivered to their respective experimental stations with a certain time delay between the two FEL pulses. Generating and controlling multiple FEL pulses at different wavelengths require precise synchronization of the electron beam and undulator sections, which can be technically demanding and resource-intensive.

The choice between the various available pump-probe schemes is usually chosen based on the specific research goals, the dynamics being studied, and the available experimental capabilities.

2.5 FEL-based PECD Study of Chiral Molecules

The interaction of chiral matter with helical light depends on the handedness of the light wave and the chiral object. The coupling between an external electromagnetic field and the chiral properties of the chiral matter can be described mathematically by the radiation/matter coupling Hamiltonian, which consists typically of several components, the electric (I), the magnetic (II) dipole coupling and (III) higher-order multipole contributions [119]:

$$H(t) = -\underbrace{\boldsymbol{\mu} \cdot \mathbf{E}(t)}_{I} - \underbrace{\mathbf{m} \cdot \mathbf{B}(t)}_{II} - \underbrace{...}_{III} \tag{2.13}$$

with $\boldsymbol{\mu}$ the electric dipole moment, $\mathbf{E}$ the incoming electric field, $\mathbf{m}$ the magnetic dipole moment and $\mathbf{B}$ the incoming magnetic field. (I) describes the interaction between the electric field of the electromagnetic wave and the electric dipole moments induced by the chiral structure. The electric dipole moment

arises due to the asymmetric distribution of charges in the chiral system. The interaction between the electric field and the induced dipole moments leads to phenomena such as optical activity and circular dichroism [120]. (II) accounts for the interaction between the magnetic field of the electromagnetic wave and the magnetic properties associated with the chiral material. The interaction between the magnetic field and the magnetic properties of the material leads to phenomena such as magneto-optical activity and magnetic circular dichroism. (III) higher-order multipole moments, which play a significant role in larger systems, systems with strong electric field gradients, or systems with complex charge distributions. Within the dipole approximation, contributions (II) and (III) are neglected.

PECD is a chiral discriminator solely based on electric dipole interactions. In the photoionization process, electric dipole transitions are included, which yield chiral signals purely from electric dipole coupling and which are much stronger in comparison to techniques relying as well on the magnetic interaction, or higher-order coupling contributions [120]. These chiral methods, as well as other exclusively electric-dipole-based techniques [121] are out of the scope of this work. Detailed information can be found in the above-cited further readings.

Here, the focus lies on PECD, which was predicted in 1976 by Ritchie [16] and rediscovered in 1982 by Cherepkov [51]. An effect, which was calculated to have a strength of up to a few tenses of percent [122]. It took more than 20 years until the first experimental observation, reported by Böwering et al. [123]. For randomly orientated chiral molecules in the gas phase, the PECD strength is reduced to lower values in the order of a few percent, due to the integration over all molecular orientations. The photoelectron angular distribution $I(\Theta)$ (abbreviated as PAD and mathematically introduced in Equation (2.8)) of chiral molecules exhibits an asymmetry or directional preference in the emission of photoelectrons. PECD is a normalized differential measure of the asymmetric PADs with respect to the polarization plane, after the photoionization of non-orientated enantiomers by different helicity of the circularly polarized light. This forward-backward asymmetry (schematically presented in Figure 2.9) can be mathematically expressed by:

$$PECD = \frac{I_+(\Theta) - I_-(\Theta)}{I_+(\Theta) + I_-(\Theta)} \tag{2.14}$$

The asymmetry in the photoelectron angular distribution is inverted if the same enantiomer is illuminated by different helicity, as above-mentioned and visualized in Figure 2.9, or when the light helicity is the same, but the enantiomer is switched to the opposite handedness. When both enantiomers are present in a racemic mixture or an achiral molecule, their contributions to the PAD cancel each other out. This results in a symmetric PAD with no

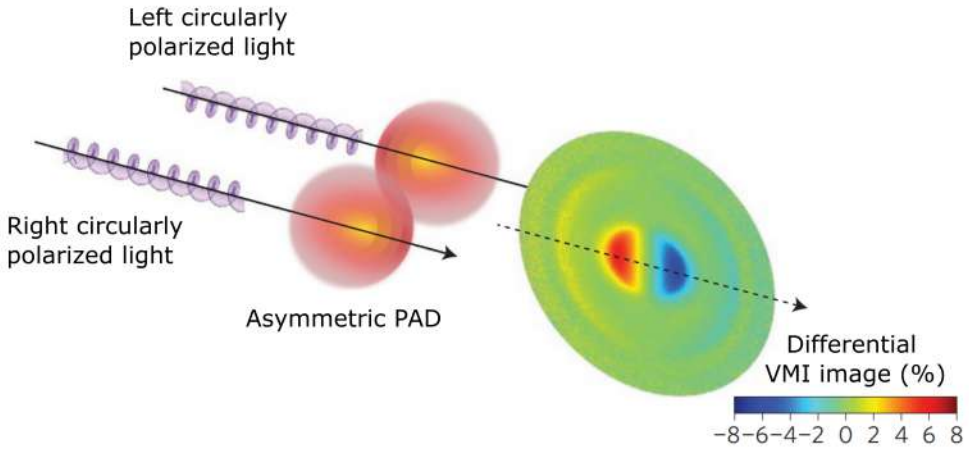

Figure 2.9: PECD principle retrieved from the differential image of the measured asymmetric PADs originating from the same enantiomer and different helicity. Figure adapted from [124].

overall chirality signal.

PECD has furthermore some important characteristics. It obtains a high-signal-to-noise ratio and a sensitivity for conformation [125, 126], isomerism [127], chemical substitutions, initial molecular orbitals, and dynamical final continuum states. PECD is, therefore, a good chiral discriminator in the light of ultrafast time-resolved chiral studies, due to the large modulation in signal during changes in the electronic and nuclear molecular structure [128]. However, it yields a variety of challenges due to its broad sensitivity to these many effects. FEL-based PECD studies are a promising candidate for enabling chiral femtochemistry via time-resolved PECD (TR-PECD).

PECD can be exploited by a variety of light sources and photon energies. Due to its sensitivity to the initial and final states, it can be challenging to disentangle the observed asymmetries, for example, the case when probing valence-shell electrons [129, 130]. Therefore, offering the possibility of addressing via single-photon ionization core shells, which are highly localized, enables solely probing the asymmetries arising from the final continuum state [131, 132], thus addressing more precisely the chiral center in the molecule. Following ultrafast chiral dynamics via FEL-based TR-PECD studies after inner-shell photoionization was not realized so far because their realization is very challenging. The reasons, therefore, are: the small effect of PECD, the limited access to FEL facilities, and in addition, only one undulator-based circularly polarized FEL (FERMI) is currently available. Furthermore, limited repetition rates for synchronized pump-probe experiments at current FELs were an additional challenge. Nonetheless, the first realization of a PECD measure-

ment at FELs on an ionic target was reported by Ilchen et al. [118]. Due to the importance of this work's retrieved result toward future TR-PECD studies, the experiment will be shortly elaborated: The first site-specific PECD of the dissociating chiral cation $C_3H_3F_3O^+$ for one time delay was measured via an experiment performed in a two-color X-ray pump X-ray probe scheme using the XFEL pulses from LCLS [104, 133]. The neutral chiral molecule was singly ionized at the F 1s shell via a linearly polarized X-ray pulse. The cation underwent an Auger-Meitner decay and ended up in a doubly charged molecule, $C_3H_3F_3O^{2+}$. After charge redistribution, the molecule Coulomb exploded. During the fragmentation process, a second circularly polarized X-ray pulse probed the F 1s shell of the singly charged mother fragment $C_3H_3F_2O^+$ at different distances to the ejected F^+ ion. A few eV photoelectrons were detected via a VMI spectrometer. As a side note, in PECD studies, probe photon energies are usually chosen in such a way as to be a few eV above the ionization threshold because PECD vanishes for photoelectrons with high energy. These fast photoelectrons do not have the chance to scatter on the chiral potential of the mother fragment and do not contain imprinted information about the chirality [122]. The performed X-ray pump and probe experiment by Ilchen et al. contained a large complexity of nuclear and electron dynamics, which limited access to TR-PECD. It is, therefore, experimentally potentially more favored to induce a more controlled dissociation at a specific bond, for example, realizable via optical-laser pump pulses. This approach was realized within the performed study presented in Chapter 5 but the objective of measuring the first TR-PECD was unfortunately not achieved.

The results of this PhD work do not present a TR-PECD but contain essential steps toward the future investigation of ultrafast dynamics in chiral systems using free-electron lasers. It presents progress in the underlying challenges as the methodology, the concept, the development and commissioning of suited ultrafast VMI spectrometers, and the understanding of the fundamentals of ultrafast light-matter interaction and nonlinear physics, which was studied during the first experiments performed at the SQS endstation at EuXFEL, which has high potential and is foreseen for future FEL-based chiral studies. The results will be presented in the following chapter.

Chapter Three

Early Science at European XFEL

Brilliant FEL pulses are up-to-date at EuXFEL [63, 78, 134] available on six instruments, which are supplied via the SASE1, SASE2 and SASE3 photon beamlines. EuXFEL started its operation in 2017, delivering hard X-rays through the SASE1 beamline to two experimental stations. The author was working on the beamline transport systems within previous works [92, 135, 136] (entry no. 1 in author's publication list) contributing to the development of X-ray-optical components and characterizing the first X-rays delivered to the SASE1 experiments [86] (entry no. 2 in the author's publication list). 2018, the author joined the Small-Quantum-Systems (SQS) group, a soft X-ray endstation dedicated to studying fundamental processes of light-matter interaction in atomic and molecular systems as well as nanoparticles and clusters [137]. Due to the gained expertise within the Bachelor's and Master's thesis, the author could contribute as well in the calibration of optical components delivering the beam to the SQS instrument through the SASE3 beamline [93] (entry no. 3 in the author's publication list). Furthermore, contributions to characterizing the SQS's beam transport system [138, 139] (entries no. 20 and 21 in the author's publication list) including, the timing between X-ray and optical laser pulses for pump-probe experiments [105] (entry no. 11 in the author's publication list), are recorded. The SQS endstation was built with the purpose of "complete characterization of the ionization and fragmentation process, at least for smaller systems, by analyzing all products created in the interaction of the target with the FEL pulses" [78]. Thus, it will be the chirality endstation for future studies at EuXFEL. It offers the possibility to perform experiments in the gas phase using photon energies in the range from 400 eV to 3000 eV, covering several K-edges of relevant atoms such as nitrogen and oxygen. The involvement in the first SQS experiments [110–114, 140–144] (entries no. 7-10, 13-16, 18 and 19 in the author's publication list), shapes the future regarding future chirality science at EuXFEL. In the following, the main results of these papers will be shortly presented.

3.1 Beam Characterization

Photon beam parameters need to be characterized properly to enable the delivery of the requested beam specifications, which vary in dependence on the experiment and the foreseen triggered physical effects on the target, here specifically on atoms and molecules. As shortly presented in the chapter before, the via SASE produced photons are transported and modified on their way. This modification starts after the undulator section and ends before the interaction region of the conducted experiment, over a distance of more than 1 km. Therefore, properties, such as the intensity, beam shape, beam size and time structure are of utmost importance for the success of experiments and need hence to be studied and characterized properly.

Metrology characterization of ultraprecise bendable mirrors for the European XFEL: from offsite calibration to installation and commissioning, Vannoni et al. (2019) [93] External reflection via grazing incidence has the lowest absorption and therefore highest transmission in the X-ray optic regime. The used angles are in the range of a few degrees and the resulting beam footprint is large, which is accompanied by the usage of optical components. 950 mm long X-ray mirrors are installed at each SASE beam transport system at the European XFEL's underground tunnels. They can be mechanically bent to cylindrical shapes and used to change the focus position of the X-ray beam along the propagation axis, regarding the required experimental setup. These systems were calibrated in the lab with an accuracy of a few nanometers using a Fizeau interferometer to avoid a wrong mirror shape after the installation into the bender system and before the installation into the beam transport system in the tunnel's vacuum chambers. Besides, to measure the change of the mirror curvature in vacuum, capacitive sensors were installed at the back of the mirror and calibrated as well in the lab. Due to the installation work, the lab alignment changes by a few micrometers after placing the complete mirror system into the vacuum chamber. Therefore, beam size measurements were performed at the SASE3 beamline to retrieve the new linear calibration curve. The beam diameter was retrieved from different imagers placed along the FEL beam propagation and the focus was therewith calculated geometrically. The new calibration data was compared to the initial lab calibration. The following results were presented. The distance between the capacitive sensor and mirror changed during the installation, inducing a shift of the calibration curve. The slope of the two calibration curves was also figured out to be different by 15 %, most probably due to the systematic error of the incidence angle between the FEL beam and the mirror surface or some non-linear effects of the capacitive sensor caused by some misalignment during the installation. The observations need to be further investigated in future studies. Nevertheless, the retrieved calibration curve was a good basis for operating the bendable mirrors and delivered reproducible and reliable results during the commissioning and first experiments at the two SASE3 experimen-

tal stations SQS and SCS.

The beam transport system for the Small Quantum Systems instrument at the European XFEL: optical layout and first commissioning results, Mazza et al. (2023) [138] FEL beams entering from the beam transport system of the underground tunnels into the experimental hutch, contain vertical and horizontal intermediate foci (virtual sources), which are displaced by few tens of meters. Kirkpatrick–Baez (KB) mirrors, with a fixed and non-bendable curvature, placed in the experimental hutch compensate these foci offsets and image the virtual sources into the same focal position, typically the place where the experiment takes place. The SQS optical system commissioning results are presented regarding the focusing performance and beamline transmission. Energies per pulse measurements were performed for various possible optical setups using X-ray Gas Monitor (XGM) detectors before any optical elements and after the last mirror in the experimental hutch, covering the photon energy range between 0.25 and 4 keV. "The measured transmission is on average between 10 % and 20 % lower than calculated, likely due to the degradation of the mirror coatings induced by X-ray exposure". The SQS expected focal spot, after all optical elements, was predicted to be 1.5 µm FWHM for 1.05 keV photon energy. It was simulated using the SHADOW code, transporting an extended Gaussian beam source through all mirrors including their polishing error, angles, shapes, and distances. First, the spatial distribution of the beam was measured via a wavefront sensor placed at the end of the experimental hutch, delivering a double Gaussian contribution of an intense beam part with 1.9 µm FWHM and a from the center left-shifted broad background with 8 µm FWHM. Second, Argon atoms were ionized sequentially by multiple photons, and the comparison of the calculated and measured charge-state distributions provided access to the beam size for photon energies between 1200 and 1700 eV. Data from the two experiments reproduced well the simulation result and was even able to show the suitability of the optical system to focus below 1.5 µm with a photon flux of 0.12 to 0.16 $\mathrm{mJ/\mu m^2}$ fulfilling the requirements for performing a broad variety of non-linear studies beyond the previously available possibilities.

Harmonic radiation contribution and X-ray transmission at the Small Quantum Systems instrument of European XFEL, Baumann et al. (2023) [139] Experiments at FELs often exploit a high photon fluence, defined as the number of photons per unit area. For this reason and in addition to the ultrashort pulse durations, the FEL beam needs to be focused tightly, to a few micrometers, and the beamline transmission as high as possible to ensure a high number of photons interacting with the target. Therefore, the total energy of FEL shots was investigated via "the photoionization of a dilute gas" or "temperature changes induced by the X-ray radiation in an absorber" using XGMs and a compact room-temperature bolometric radiometer (CBR), respectively. The results deliver the transmission of the FEL beam, in the photon energy range between 650 eV to 2400 eV, after passing one specific setup

of the optical system, including the first two tunnel mirrors and the bendable KB system in the SQS hutch. Each mirror reaches a maximum reflectivity of 90 % depending on the photon energy and incidence angle of the beam. XGM data from the single-shot FEL energy was measured first directly at the end of the undulator and second at the end of the SQS's KB system. Relative measures of the two XGMs delivered an absolute and usable transmission between 65 % and 75 %. The absolute averaged FEL energy at the end of the beamline, delivered by the CRB, was 75 % to 80 % (for incidence angles of 9 mrad for the first two mirrors in the tunnel). A change to 20 mrad incidence angle reduced the transmission to 50 %. Nevertheless, these angles are advantageous if the transmission is still sufficient, but contributions from harmonic FEL radiation, which "were determined to be a few percent for the third and 0.1 % to 0.3 % for the second harmonic", need to be removed (possible for photon energies up to 1500 eV). The measured transmission values were lower than the calculated values, which can be caused by slight misalignment or even additional radiation damage on the mirror coating.

Timing and X-ray pulse characterization at the Small Quantum Systems instrument of the European X-ray Free Electron Laser, Grychtol et al. (2021) [105] Time-resolved experiments are commonly performed in a pump-probe scheme, meaning that a reaction is triggered via a pump pulse and observed by the temporally shifted probe pulse. SQS commissioned and characterized its available optical laser (OL) pump - XFEL probe system in terms of temporal resolution, which depends mainly on the pulse durations and the timing jitter between both pulses. A crucial point is the accurate temporal synchronization of both pulses to minimize the timing jitter. The synchronization was performed via "stabilizing the pulse train of the OL seed oscillator regarding the RF driving the electron bunches in the XFEL accelerator". The timing performance was quantified by a timing jitter of 58±1 fs (FWHM), by measuring 4000 single timing jitters (difference of optical laser and FEL beam arrival time) with the Photon Arrival time Monitor (PAM). Besides proper synchronization, fluctuation, drifts of the accelerator components, the SASE processes, vibrations along the OL path, and temperature and humidity instabilities lead to some additional induced timing jitter. Nevertheless, the retrieved values are comparable to other XFEL light sources. Furthermore, the average X-ray pulse length τ_{XFEL} was first characterized by performing X-ray/optical cross-correlation measurements performed in an XFEL-pump OL-probe scheme on Neon. The XFEL pulses generated Auger electrons with a kinetic energy of 804.3 eV, which were afterward "dressed along its polarization axis, changing their kinetic energy and thereby giving rise to a characteristic sideband structure" due to the presence of the intense OL field. The laser-assisted Auger-Meitner decay electron spectra were recorded via a time-of-flight spectrometer of the AQS chamber. Sidebands up to the 3rd order were measured. The highest sideband was integrated and fitted with a Gaussian function, delivering a cross-correlation time of $\tau_{cc} = 72\pm4$ fs. An analytical Gaussian convolution using τ_{cc} and $\tau_{OL} = 38.1\pm02$ fs delivered for

the X-ray pulse length a value of $\tau_{XFEL} = 38 \pm 2$ fs, which was confirmed as well by additional time-dependent Schrödinger equation (TDSE) simulations.

3.2 First Experiments at SQS

The targeted areas of research of the SQS experiments are non-linear processes, time-resolved ultrafast dynamics, and coherent imaging experiments in the gas phase. For each experimental purpose, versatile experimental chambers were built: AQS (Atomic-like Quantum Systems), REMI (Reaction Microscope), and NQS (Nano-sized Quantum Systems), including various spectroscopic tools. In the following, the first experiments performed at AQS and REMI, with strong contributions by the author and co-authorships, are presented.

All presented conducted experimental studies supported the characterization of the FEL radiation of the EuXFEL. High-repetition rate, ultraintense and ultrashort pulses, which are tunable over a wide range of photon energies, enrich the portfolio of the current available FELs worldwide. The series of beamtimes demonstrated the first commissioning, operation, and possible applications of the new instrumentation at SQS. These novel experimental schemes can be used for future pioneering experiments. The experiments provided insight into complicated multi-photon interactions with matter, targeting atoms and small to medium-sized molecules, which are an important prerequisite for pump-probe studies on chiral molecules. Furthermore, the experimental studies showed promising time-resolved results under various pump/probe schemes, i.e. using intra-SASE X-ray pump/X-ray probe or OL-pump/X-ray probe, chosen to conform to the time scales of the processes under investigation.

The author's contribution, within the collaborations and the earlier science phase of SQS (over the first year of the PhD studies), involved various tasks, such as apparative work before or during beamtimes, scientific work, as precalculation of some optical parameters, i.e. beam size at different positions along the beam transport system, and also the analysis of experimental data during or after the experiment. Furthermore, adapting middle layer devices in the Karabo software [145] to facilitate the control of specific components within the GUI and operating the SQS beamline, for instance, aligning the beamline before starting an experiment, were also a big part of the PhD work.

AQS

High-resolution electron time-of-flight spectrometers for angle-resolved measurements at the SQS Instrument at the European XFEL, De Fanis et al. (2022) [140] For the investigation of electronic structures, electronic states, and relaxation processes, electron time-of-flight (eToF) spectrometers are widely used. Their capability to detect electrons at high repetition rates makes them, especially at FELs, which are operated at MHz, a favorable tool. These spectrometers are built to collect electrons from a narrow solid angle through an entrance aperture, here with an opening angle of $\pm 10°$, which is optimized for the applications at SQS because of the possibility to observe the same interaction point with more than one spectrometer. Electrodes supplied with high static voltage, create an electrostatic lens, which influences the electron trajectories so that all electrons reach the detector and thus do not collide with the detector walls. The trajectories can be parallel or cross each other within some intermediate focus. To increase the energy resolution, these electrostatic fields decelerate the electrons in the drift tube. The detection and signal out coupling are realized via MCPs and an anode, either in single electron mode or analog mode (multiple electrons at the same time). Before the installation of such six foreseen eToF spectrometers at the SQS instrument, one prototype was commissioned at the PETRA III P04 beamline at DESY in Hamburg using FEL similar pulse separations of $\sim$200 ns and resonant Auger spectroscopy. A photon energy of 867.11 eV was used to study the decay of the core-excited Ne $1s^{-1}3p$ state. Auger lines $2s^1 2p^5(^{1,3}P)np$ and $2p^4(^3P,^1D$ or $^1S)np$ with n = 3 or 4 (kinetic energy ranges 770 eV to 790 eV, and 800 eV to 816 eV, respectively) were measured delivering a line width of $\Delta E < 100$ meV and hence a resolving power of $\Delta E/\mathrm{E} > 10000$. Furthermore, the set of eToFs was tested after the successful installation at SQS, performing the same experiments as before. Demonstrated was also the possibility to extract angular distributions, which delivered the expected angular distribution anisotropy parameter β_2 close to 0 and for the photoline $2s^{-1}$ (E_{kin}=818 eV), and β_2=1.1 for the photoline $2p^{-1}$ (E_{kin}= 845 eV). As presented, AQS opens the door to measuring versatile physical observables, but in addition, it opens the door to studying the breakdown of the dipole approximation thus non-dipole effects, which "can arise when the laser wavelength is comparable with the size of atoms". This effect leads as well to a forward/backward asymmetry in the photoelectron angular distribution and should be distinguished from the PECD.

Mapping Resonance Structures in Transient Core-Ionized Atoms, Mazza et al. (2020) [110] For the investigation of ultrafast time-resolved and nonlinear processes, transient electronic states play an important role and partly determine furthermore the dynamics of the evolving system. XFELs are suited to study a new kind of these femtosecond short-lived states due to their high intensity of up to 10^{18} W/cm^2, their energy tunability, and their kHz

repetition rates. Within this work, resonant Auger spectroscopy was performed on a highly transient system, to map the "high-lying np-Rydberg resonances of the transient Ne^+1s^{-1} ion". Neon was first core-ionized (K-shell) via one photon of the FEL pulse (pulse energy 2 mJ, pulse duration 25 fs, repetition rate 10 Hz, and focus FWHM 1.5 x 1.5 µm^2), creating a single-core hole (SCH) in the 1s shell. The ejected electron has a binding energy of $E_{Bin} = 870.2$ eV. This state typically relaxes via an Auger-Meitner decay within 2.4 fs. Before the ultrafast relaxation occurs, a second photon resonantly excited the second and more tightly bound 1s electron ($E_{Bin} = 995.2$ eV) into a valence orbital by creating a so-called (resonant) double-core hole (DCH): $Ne^+1s^{-1}2s^22p^6 + h\nu \rightarrow Ne^{+*}1s^02s^22p^6np$. The photon energy was varied in the range between $h\nu$= 970 to 1000 eV in steps of 1 eV (ranging from the first unoccupied Rydberg state 3p to the continuum). Electron spectra were measured using one electron ToF spectrometer of the AQS chamber. The data delivered a 2D resonance map. It was figured out, that the spectator transition $Ne^+1s^02s^22p^6np \rightarrow Ne^{2+}1s^12s^22p^4np$‘ (n = n‘) is the dominant decay channel for all resonances. Contributions from shakeup (n < n‘) and shakedown (n > n‘) processes were significantly different for the investigated np resonances (n = 3, 4, and 5). One of the open and interesting questions, regarding PECD, is how it develops in a transient state and how additional localized charges close to the chiral center may affect its signal amplitude. Therefore, DCH studies, similar to the presented experiment, offer the possibility to probe the PECD of a very short-lived transient singly ionized state of the chiral molecule before any nuclear dynamics start to evolve and alter the PECD signal.

REMI

Double Core-Hole Generation in O_2 Molecules Using an X-ray Free-Electron Laser: Molecular-Frame Photoelectron Angular Distributions, Kastrike et al. (2020) [111] DCH spectroscopy is a sensitive tool to investigate the bonding properties of molecules. K-shell electrons can be emitted via sequential photoabsorption of two photons either from the same atom within a molecule, called single-site double core-hole (SSDCH or K^{-2}) or from two different atoms, termed two-site double core-hole (TSDCH or $K^{-1}K^{-1}$). Small diatomic molecules, as the here studied O_2, typically have DCH lifetimes of less than 5 fs, defining the time window to create the two K vacancies. The classical measurements of photoelectron energies and laboratory frame electron angular distributions can be expanded via molecular-frame photoelectron angular distributions (MFPADs), which are an advanced tool to probe the molecular geometry and potential. In the presented work, first MFPADs of the second O_2 photoelectrons with ∼30 eV and ∼110 eV, respectively emitted after SSDCH ($O_2 + 2h\nu \rightarrow O_2^{2+}(K^{-2}) + 2e^- \rightarrow 2O^{2+} + 4e^-$) and TSDCH ($O_2 + 2h\nu \rightarrow O_2^{2+}(K^{-1}K^{-1}) + 2e^- \rightarrow 2O^{2+} + 4e^-$), were identified. The data was retrieved via the performance of multi-particle (two-electron-two-ion)

coincidence measurements using the Reaction Microscope (REMI) endstation at SQS and FEL photon energy of 670 eV (pulse duration 25 fs, pulse energy 30±5 µJ, focus size ∼0.9 x 1.6 µm^2 and repetition rate of up to 420 Hz). The experimental results were compared with theoretical frozen- and relaxed-core Hartree-Fock approximations. The first approximation implies, that "the orbitals of the remaining electrons are modeled as frozen in their configuration before the photoionization" of the second K photoelectron. The second one includes "a relaxation of these orbitals to the potential of the core-ionized molecule". The calculations show good agreement for the TSDCH case. For SSDCH one of the two models, the frozen-core Hartree-Fock approximation, fails due to the occurrence of a σ-shape resonance at ∼40 eV. DCH spectroscopy is a tool with high chemical sensitivity and element specificity, which makes it an appealing technique for chirality studies on molecules.

Photoelectron Diffraction Imaging of a Molecular Breakup Using an X-ray Free-Electron Laser, Kastrike et al. (2020) [112] In the presented work ion-ion-electron coincidence measurements of the charged fragments of O_2 molecules were performed during the X-ray-induced fragmentation. Due to the high flux of the FEL X-ray pulses, sequential core-shell ionization can be realized within a single X-ray pulse. Here, a two-photon intra-SASE pump-probe scheme using a 670 eV FEL pulse[1] is presented. The first K-shell ionization occurs on one oxygen atom within the O_2 molecule. The singly charged molecule fills the K-shell vacancy via an Auger-Meitner decay (AMD) and results in O^+/O^+, which fragments via Coulomb explosion. The dissociative intermediate state is again K-shell ionized via a second X-ray photon at random delay times, which contains information about the elongation of the molecular bond. The emitted second photoelectron (e^-_{ph2}), multiply scatters on the molecular potential while it propagates away from the host atom and "illuminates the molecular structure from within". A subsequent AMD results in the state O^+/O^{3+}, which continues the dissociation (1. $O_2 + h\nu_{pump} \rightarrow O_2^+ + e^-_{ph1} \xrightarrow{AMD} O^+/O^+ + e^-_{ph1}e^-_{AM1}$, 2. $O^+/O^+ + h\nu_{probe} \rightarrow O^+/O^{2+} + e^-_{ph2} \xrightarrow{AMD} O^+/O^{3+} + e^-_{ph2}e^-_{AM2}$). The singly and triply charged atomic oxygen ions were measured in coincidence with the second photoelectron e^-_{ph2}, resulting in polarization-averaged MFPADs (PA-MFPADs), which are electron diffraction patterns in polar coordinates, that reveal information about the increase in the internuclear distances during the breakup of the molecule. The assumed internuclear distance was "computed from corresponding kinetic energy release (KER) values" of the ions and showed good qualitative agreement with theoretical calculations for KER values between 28 eV and 36 eV. For O_2 molecules, studied under this specific setup (same experimental conditions as in the previously presented paper [111]), the molecular bond was elongated by 1.2 a.u. within the duration of the one X-ray pulse (∼25 fs) and represents the first case of internuclear distance-resolved photoelectron diffraction patterns studied in the gas phase. This work is a further step in the way of realizing time-resolved pump-probe photoelectron diffraction imaging

and molecular movies with XFELs. As well, a valuable tool for time-resolving investigations for chiral molecules in the gas phase.

Investigating charge-up and fragmentation dynamics of oxygen molecules after interaction with strong X-ray free-electron laser pulses, Kastrike et al. (2022) [113] PA-MFPADs do not only offer the possibility to extract geometrical information, for example, the molecular bond elongation, as presented in the previous work by Kastrike et al. [112]. The analysis can be extended to trace femtosecond charge-up and fragmentation dynamics. This approach is presented within this work, using the experimental data of the oxygen molecule presented before [111, 112]. By irradiating the molecule with X-ray FEL pulses[1], three break-up channels appear with different relative strength: O^{3+}/O^{2+} : 1 (channel of interest within the work), O^{3+}/O^{1+} : 0.66 and O^{4+}/O^{1+} : 0.14. These final states correspond to different processes involving photoionization (P), Auger-Meitner decay (A), and an additional shake-off event during photoionization (P_s). The main process sequences for the final states are P_sAPA ($O_2 \xrightarrow{P_sA} O^+/O^{2+} \xrightarrow{PA} O^{3+}/O^{2+}$), PAPA and PAP$_s$A, respectively. Charge transfer (CT) can occur at short internuclear distances during the molecule's fragmentation. This leads to an additional satellite channel for the final state O^{3+}/O^{2+}, which follows from a PAP$_s$A sequence and additional charge-transfer ($O_2 \xrightarrow{PA} O^+/O^+ \xrightarrow{P_sA} O^{4+}/O^{1+} \xrightarrow{CT} O^{3+}/O^{2+}$). To verify the two different routes yielding O^{3+}/O^{2+}, the backward-forward ratios of PA-MFPADs of the second 1s photoelectron were analyzed and in good agreement with the calculations. The two channels could be distinguished since the main channel yielded only the photoelectron (high KER range 80 - 110 eV) and the satellite channel two electrons, originating from the shake-off photoionization (low KER range 55 - 80 eV). Furthermore, the temporal evolution of both dissociating intermediate states, O^+/O^+ and O^+/O^{2+}, during a single X-ray pulse was investigated. It was figured out, by theory, that it takes 18 fs to yield KER values lower than 40 eV, which corresponds to an O-O bond elongation of 5 a.u. and 7 a.u for the two intermediate states in this sequence.

Inner-Shell-Ionization-Induced Femtosecond Structural Dynamics of Water Molecules Imaged at an X-ray Free-Electron Laser, Jahnke et al. (2021) [114] Characterized and presented are fragmentation dynamics of H_2O molecules, including structural and time information. The molecules were core-ionized via an XFEL pulse (photon energy 1 keV, pulse energy 4.4 mJ, beam size 1.6 $\times$ 1.4 µm^2, and pulse duration 10 - 25 fs). The first photon-absorption at the time t_1 and the subsequent AMD leads to water dications H_2O^{2+}. The molecule undergoes structural changes, i.e. it starts dissociating. At some random time delay t_2 within the pulse duration, a second photon, within the same XFEL pulse, is absorbed by the dications probing differ-

[1]The experimental data was retrieved within the same beamtime as in Kastrike et al. (2020) [111]. Hence, the beam parameters, such as beam size, repetition rate, pulse energy, and pulse duration are the same.

ent fragmentation channels in H_2O^{2+} via triple ion coincidence measurements ($O^{2+}/H^+/H^+$). Two fragmentation pathways could be identified, which depend on the delay time between the two photoabsorptions. For small delays, an unbent three-body break up of H_2O^{2+} into H^+, H^+ and O^{2+}, with protons emitted at an angle larger than 150° was observed. At a delay time larger than 5 fs, large HOH bond angles were calculated, and after approximately 10 fs HO bond asymmetries were identified, resulting in an asymmetric two-body fragmentation into HO^+ and H^+. The experimental data are in good agreement with calculations done via the XMOLECULE toolkit. Extracting information about the bond angles and bond elongations is also an important step in studying chiral systems, in which chirality is generated dynamically, for example, Formamide, which is planar in the ground state, but the chirality can oscillate between two enantiomers after the excitation with non-ionizing near-UV light [146].

Resonance-enhanced X-ray multiple ionization of a polyatomic molecule, Li et al. (2022) [141] The photoionization of CH_3I molecules is localized at the iodine side, due to a larger cross section in comparison to the methyl group. This molecule and the atomic counterpart of iodine (Z=53), Xenon with Z=54, were exposed to XFEL pulses (pulse duration 25 fs, beam size $\sim$1.4 µm^2 and repetition rate of experiment 700 Hz), resulting in resonant excitation and X-ray multiphoton ionization. The experiment was conducted for three different photon energies 2 keV, 1.5 keV, and 1.2 keV (1 mJ, 1.6 mJ, and 2.4 mJ, respectively). "Resonant excitation enables the creation of extremely high charge states which are otherwise not reachable" solely via X-ray multiphoton ionization. Charge state distributions (CSDs) of the molecule were retrieved via ion pair coincidence measurements of iodine and carbon cations. CSDs of Xenon result from time-of-flight spectra recorded under identical experimental conditions. CSDs from the total molecule and iodine alone were compared with Xenon CSDs. The following findings were presented: 1. Higher carbon charge states are more likely detected with higher iodine charge states due to charge redistribution from iodine to the methyl group. 2. Yields for higher charge states are larger for lower photon energy, caused by the larger pulse energies and photoabsorption cross sections (2 keV $\rightarrow$ I^{30+}, 1.5 keV $\rightarrow$ I^{37+} and 1.2 keV $\rightarrow$ I^{40+}). 3. "For all three photon energies, the total molecular CSD extends to higher charge states than that of Xenon, and the yield of the highest charge states is enhanced in the molecular case relative to the atomic CSDs". This can be explained by charge-rearrangement-enhanced X-ray ionization of molecules (CREXIM), which shows that this effect, originally observed in the hard X-ray regime, is also applicable to soft X-ray experiments. Furthermore, the effect is more prominent at lower photon energies. 4. "The region of resonant enhancement shifts to higher charge states with increasing photon energy". Resonant excitation with intense X-ray pulses is the first step in XFEL-based techniques, and therefore a process that can be relevant as well for a variety of FEL-based chirality studies.

Coulomb explosion imaging of small polyatomic molecules with ultrashort X-ray pulses, Li et al. (2022) [142] Multiply to highly ionized molecules, which rapidly charge up via nonlinear sequential and direct photoabsorption, obtain a large Coulomb repulsion leading to the molecule's fragmentation, also known as Coulomb explosion. A sufficient number of electrons is removed quickly, to avoid undergoing structural rearrangements of the molecule. The exposure time of XFELs, ideally in the few-femtosecond regime, is well suited for this purpose. This process can then be used to retrieve individual geometrical images of an even unknown molecule by measuring cations in coincidence. Within this paper, the molecule CH_3I was studied via Coulomb explosion imaging (CEI) induced by X-ray pulses (photon energy 2 keV, pulse duration 25 fs, beam size $\sim$1.4 µm^2 and 0.8 mJ pulse energy). For the CEI analysis, a full-fragmentation channel is required, i.e. the here used [I^{9+}, C^{3+}, 3 × H^+] channel. Data is retrieved out of four/five-ion coincidence measurements, detecting the cations I^{9+}, C^{3+}, 2 - 3 × H^+. The full 3D molecular-frame ion-momentum distribution shows, that the iodine and carbon ions appear in a back-to-back emission with a high momentum. Perpendicular to it, the hydrogen ions are evenly distributed on a circle and show a small absolute momentum. To complete the geometrical image of the molecule, C-I and C-H bond lengths and I-C-H bond angles were calculated theoretically. The reason, therefore, was, that the time for the charge build-up process, hence the "competition of sequential ionization, AMD deexcitation, and charge redistribution, taking place within the timescale of the XFEL pulse length", was unknown. This time was calculated to be $\sim$10 fs and delivered bond lengths $l_{C-I} = 2.1 \pm 0.2$ Å, $l_{C-H} = 1.1 \pm 0.4$ Å and the bond angle $107° \pm 3°$. These values are in agreement with the molecule being in equilibrium. CEI can be used to determine the 3D structure, thus the molecule's handedness, of single chiral molecules.

X-ray multiphoton-induced Coulomb explosion images complex single molecules, Boll et al. (2022) [143] CEI was considered to be unfeasible for complex molecules. The complexity increases once drastically with the size of every single atom within the molecule and second it depends on the molecular geometry, for example, bond angles. Studying such molecules was expected to be still unfeasible in the gas phase, due to the lack of statics while recording all molecular constituents in coincidence. Nonetheless, within this work, the planar molecules 2-iodopyridine (C_5H_4IN) and 2-iodopyrazine ($C_4H_3IN_2$) were imaged entirely via CEI, i.e. including the hydrogen atoms. Furthermore, detailed information about their ultrafast intramolecular electron rearrangement is presented without measuring all atoms of the molecules in coincidence. The molecules were exposed by 2 keV XFEL pulses (energy 0.8 mJ, duration 25 fs, up to 570 pulses per second, and a focus size of 1.4 x 1.4 µm^2), and the 10 and 11 atoms charged up within only a few femtoseconds within one X-ray pulse, which led to momentum images of good quality, imaging the molecular geometry close to the equilibrium, as desired within CEI. Detecting only a few generated ions, via partial coincidence, generally implies a loss of in-

formation. The key technological feature for the successful measurement was the high-repetition rate of the EuXFEL, which delivered a "sharp momentum distribution" that "provides direct insight into the fragmentation dynamics". In this work, fourfold coincidence events of charged ions (one H, one C, one N and one I) were used to retrieve the experimental data. Calculations were additionally performed via the theoretical toolkit XMDYN, which is a Monte Carlo scheme including "charge transfer between the atom pairs based on a classical over-the-barrier model". They were in good agreement with the measured data. The results revealed that hydrogen evolves first and during the X-ray pulse. They showed small momenta ($|p_H| \approx 55$ a.u.) and "the average C–H distance increases by almost a factor of two within the first 5 fs after the pulse center", confirming that the protons were ejected before the full charge up of the molecule. The movement of heavier fragments started after the illumination with the X-ray pulse. "Distances of the C–C and C–N bonds elongated as expected". Lastly, the distance between the iodine and neighboring carbon ion (I–C) decreased first by almost a factor of two, with a minimum after 30 fs and was larger than the equilibrium distance after about 50 fs. "91 % of all the photoionization events take place at the iodine site", resulting in iodine ions up to charge state I^{25+}. The additional detection of H^+, C^+ to C^{4+} and N^+ to N^{3+}, indicated that "ultrafast electron rearrangement occurs within the molecule".

Photon-recoil imaging: Expanding the view of nonlinear X-ray physics, Eichmann et al. (2020) [144] The interaction of light and matter is a nonlinear process, which is accessible via XFELs due to their high pulse intensities. One possible standard tool to study electronic and vibrational excitations in solids, liquids, and gases is stimulated X-ray Raman scattering (SXRS). The usual way is to detect the scattered photons. Here, a new experimental approach was presented, which detects scattered neutral atoms. Therefore, photon-recoil imaging (PRI), defined as the momentum transfer from photons to the atoms, was used to study SXRS of metastable neutral neon atoms (Ne*). This method is in comparison to direct SXRS free from background caused by the primary radiation. Neon atoms were injected via a supersonic beam and were resonantly K-shell excited via 867.3 eV XFEL pulses ($Ne[1s^{-1}3p]$). The lifetime of the state is ∼2.5 fs and deexcited predominantly via an AMD. "About 2 % of the excited atoms decayed radiatively, predominantly by the 2p → 1s transition at ∼849 eV" ($Ne[2p^{-1}3p]$) and decayed after a few nanoseconds again to long-lived metastable neon atoms ($Ne^*[2p^{-1}3s]$), which were detected at an MCP detector of the REMI endstation, showing the deflection of the particles. Atoms, which were excited without a momentum transfer, were detected as a line, that represents the interaction region of the atoms with the photon beam". Whereas, atoms with a momentum transfer, acquired a "recoil velocity of ∼14 m/s along the direction perpendicular to its original velocity". These atoms were displaced by approximately 5 mm on the detector and belong to the stimulated X-ray Raman scattering process. Atoms from the spontaneous X-ray Raman scattering process showed an isotropic mo-

mentum transfer due to atoms with a large spread of velocities, delivering a blurred image of the interaction region. The SXRS process was identified and studied under the variation of the incident XFEL radiation, i.e. the intensity, photon and pulse energy, and monitored via PRI. The results indicated that PRI offers the possibility to explore SXRS, which can be used as a tool to study nonlinear physical processes.

EuXFEL offers with the scientific instrument SQS various spectroscopic techniques, emphasizing at this point the relevance and benefit of the demonstrated coincidence spectroscopy in various applications via the experimental station REMI. It enables to measure electrons and ions simultaneously, to capture the ultrafast time evolution of the electrons in real time, technically capable of pushing the frontier even to the attosecond regime, and to cover the full system by including the ions as a relevant part of the reaction products.

Attosecond pulses at EuXFEL, which are a prerequisite for such future studies, were demonstrated in a recent experiment in June 2022 by Helml, Ilchen et al. (to be published), using angular streaking [147, 148] to characterize non-invasively all ultrashort X-ray pulses delivered to the SQS instrument. This measurement technique provides the exact temporal shape of a single FEL pulse. Free-electron laser sources are driven by a stochastic generation process that produces the SASE pulses, leading inherently to spiky spectral profiles and time-dependent intensities. Single-shot information is therefore an important measure for understanding and analyzing other observables of the experiment. This new sub-fs time regime opens new possibilities to perform time-resolved coincidence spectroscopy measurements at EuXFEL.

In light of PECD studies, a core motivation to facilitate with within this PhD thesis, the main tool for chiral sensitivity, velocity map imaging spectrometers are the common and widely used technique within the research community. VMIs, are in comparison to REMI, not limited to small particles and low count rates. The reason for the limitation is, that REMI measures information in the momentum space. To retrieve the position space information, complex reconstructions, which are until now limited to small to mid-size molecules, need to be applied. Covariance spectroscopy can be performed by simultaneously detecting the target's emitted electrons and ionic fragments and applying multi-particle correlation approaches. For such studies at EuXFEL, the VMI of the AQS end station will be extended within the Röntgen-Ångström Cluster, a German-Swedish research collaboration, the funded project "Structural Dynamics of Chiral Molecules at the Time-Scale of Electron Movement Explored with Free-Electron Lasers" (German PI M. Ilchen and Swedish PI V. Zhaunerchyk). Furthermore, within this PhD work, a portable double-sided VMI spectrometer was built and commissioned, which was specifically conceived to follow the charge migration and subsequent chiral molecular breakup via time-resolved inner-shell PECD at FELs, and can be used for experiments at SQS and will be elaborated in detail in the following chapter of this work.

The next steps toward chirality-science at EuXFEL will be the polarization commissioning of the SASE3 AppleX undulators [96] after the installation within the winter shutdown in 2023. The very first experiments with the new undulators will create highly intense, circularly polarized FEL radiation and will open the door to scientific perspectives for PECD studies toward the goal of investigating even sub-fs dynamics in complex and chiral molecules with high-repetition rates via intra-SASE pump/probe attosecond pulses, as proposed by M. Ilchen et al. [118].

To sum up, the basis for chiral science was set by the presented technical, methodological and scientific achievements. Future circularly polarized EuXFEL and FLASH2 pulses pave the way for investigating site-specific chiral dynamics down to the attosecond frontier and potentially recording the first molecular movie of how electron dynamics transfer into stereochemistry from different observer perspectives.

Chapter Four

Double-sided Velocity Map Imaging Spectrometer

4.1 Working Principle

1997, the year of the invention of the simplest approach of velocity map imaging by Eppink and Parker [149], using a three-plate assembly. Eppink and Parker's presented single-sided spectrometer was built by three plates, so-called electrodes, whereas the first one is the repeller electrode, the second the extractor and the last the ground electrode (see Figure 4.1). The purpose of such a setup is to focus charged particles with an electrostatic lens. Therefore, the three electrodes are put on different voltages to create a static electric field $\vec{e_z}$ in the direction of the spectrometer axis z. The target can be injected via a molecular jet [150]. The molecular beam passes the spectrometer parallel to the XY plane, entering between the repeller and extractor electrode. Along the photon propagation axis y, charged particles are created. The crossing between the photon and target beam is the interaction region and in the center between the repeller and extractor electrode. Within this region, a 3D ion or electron cloud is formed. Particles, with the same initial velocity vector, $\vec{v_i} = (\vec{v_{x_i}}, \vec{v_{y_i}}, \vec{v_{z_i}})$ are accelerated along the spectrometer axis z and mapped at the same point on the 2D position-sensitive dual-stacked microchannel plate (MCP) detector (fast high-gain amplifier for electrons and ions, explained in more detail in Section 4.3), capturing information on kinetic energy, angular distribution and signal intensity. The focusing capabilities, and hence the overall energy resolution, are very sensitive to the exact vertical position of the interaction region. Besides, the resolution is limited by the fact, that the particles are created in some finite volume, due to the size of the molecular beam and second due to the photon beam size, which ionizes the gas phase targets as atoms or

molecules. The image will be blurred by the area of the ionization volume. To minimize the blurring of the image, small molecular beams and focused photon beams along the spectrometer axis y, are advantageous. Detectable kinetic energy ranges of the particles are determined by the electric field $\vec{e_z}$, which is set by the geometry, distance and voltage of the electrodes. Only one of these three parameters, i.e. the voltage, can be changed and adapted during the experiment. The other two, geometry (such as opening and shape of the electrodes) and distance (electrode to electrode or electrode to detector), are typically fixed during the experiment and need therefore to be conceived and designed properly to suit the planned experimental campaigns, considering the light source specifications (repetition rate, etc.) and the energy range of the detectable particles.

Instead of detecting only ions or electrons separately, simultaneous measurements of electrons and ions over the full solid angle of 4π are interesting as a tool to deeper investigate electron processes and photodissociation dynamics [151]. One possibility is to switch the polarity, hence the electric field of the single-sided VMI spectrometer after the detection of electrons, which are detected first because they are faster than the ions [152]. Advantageous are the lower costs of the apparatus, and the independent extraction fields. A fallback of high-voltage switching is the in coupling of the electronic ringing of up to several microseconds to the signal readout, which makes the detection of ions with short flight times difficult. Double-sided VMI (dVMI) spectrometers are also capable of performing such experiments and recording many observables in parallel [153, 154]. Even though the operation is more complicated, they are nowadays widely used, attributable to detecting a wide kinetic energy range of electrons and ions simultaneously. The most compact dVMI contains 4 electrodes, which is the minimum requirement. Nevertheless, modern spectrometer designs contain additional electrodes to help to compensate field distortions. It offers furthermore the possibility to create flat equipotential surfaces and to run the dVMIs in the time-of-flight (ToF) mode [155], where the arrival times of the charged particles, which depend on the mass-over-charge ratios, are measured. The data analysis approach is in principle the same for all VMI spectrometers. The 3D ion or electron cloud is projected as a 2D "pancake" onto the detectors, and the resulting 2D images are imaged via phosphor screens and cameras. To reconstruct the 3D particle cloud and its information about kinetic energy and angular distribution, inversion methods are used, for example, the Abel inversion.

The 3D ion or electron cloud is also called the Newton sphere, with the distribution $I(r, z)$ when cylindrical symmetry exists, which is usually the case for VMI spectroscopy. The 2D projection is measured at the detector plane, defined as $P(y, z)$. Both functions are mathematically related by the Abel transform [156]:

$$P(y,z) = 2\int_{y}^{\infty} \frac{I(r,z)r}{\sqrt{r^2-y^2}}\,dr \tag{4.1}$$

Image reconstruction methods are required to calculate the quantity of interest, here $I(r,z)$, which can be calculated by the inverse Abel transform and is given by:

$$I(r,z) = -\frac{1}{\pi}\int_{r}^{\infty} \frac{dP(y,z)}{dy}\frac{1}{\sqrt{y^2-r^2}}\,dy \tag{4.2}$$

Solving Equation (4.2) is a computationally expensive calculation, and it magnifies noise. The results are often not reliable. Therefore, various computational methods to perform the inversion are nowadays available. An overview of several numerical methods and their performance can be found in further readings ([157–159] and references therein). The method of choice for this work was rbasex [159]. It can handle even and odd angular orders, and it can be used to invert a wide range of images. In addition, it is a fast, accurate, and a versatile Abel inversion method that is easy to use.

One focus of this PhD work was the usage of dVMI spectrometer for the "investigation of ultrafast dynamics in chiral systems using FELs". Meaning that the processes, which need to be investigated are bond breaking (dissociation) or bond formation, energy transport within molecules, or rearrangement of the molecules themselves. These structural changes usually take place in the femtosecond timescale regime. Ultrashort photon-pulse sources as free-electron lasers, which obtain high repetition rates, are therefore required. The use of such light sources defines additional boundary conditions. Planned spectrometers need to be designed to detect ions with a few tens of electron volts and electrons of up to several hundred electron volts of kinetic energy. The length of the drift tubes on both sides needs to be according to the required energy ranges. With higher kinetic energy of the particles, the drift tube will be shorter. Too long drift tubes result in longer travel times of the particles and will not suit the high repetition rate of FELs. Too short ones would lead to worse energy resolution. Some exemplary flight times (a few microseconds) were calculated and are presented in the following, in Figure 4.8. All these mentioned aspects need to be considered during the design phase of such an experimental apparatus. To check the design, charged particle trajectory simulations are recommendable.

Generally, the empirical relation between expansion speed ν, time-of-flight t and radius R of the image ring is [149]:

$$R = N\nu t \Longleftrightarrow \nu = \frac{R}{Nt} \tag{4.3}$$

with N the magnification factor. For the kinetic energy of the particles, follows:

$$E_{kin} = \frac{1}{2}m\nu^2 = \frac{1}{2}m\left(\frac{R}{Nt}\right)^2 \propto R^2 \tag{4.4}$$

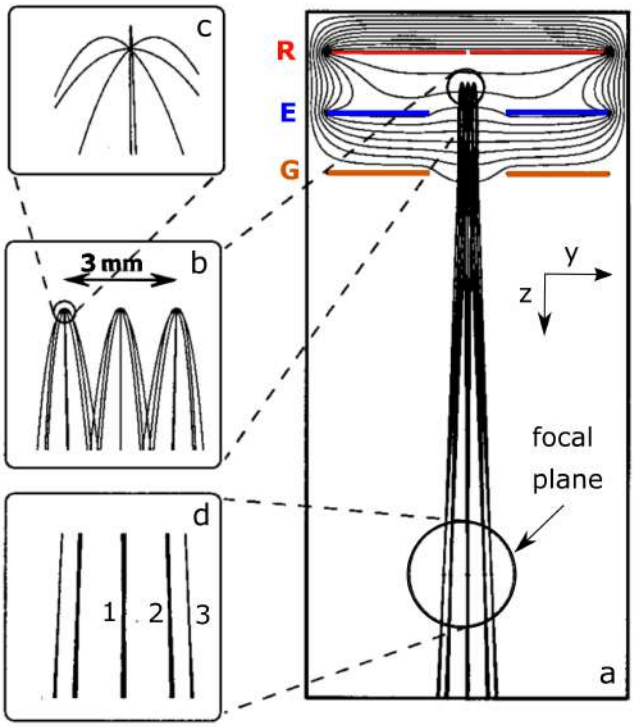

Figure 4.1: Eppink and Parker VMI spectrometer: (a) Simulated three-plate spectrometer with its electrostatic lens and the charged-particle trajectories. The repeller electrode (R in red) pushes the charged particles toward the extractor (E in blue) and ground (G in orange) electrode. Particles are created at several points along the y-axis (b). The zoom of one of the three source points is shown in (c). Here, 8 particles are ejected into different directions and particles with the same velocity and angle are focused into the same point in the focal plane, regardless of their source point along the y-axis (d). Figure adapted from [149].

4.2 Vacuum System and Molecular-Beam Setup

One main part of this PhD project was the design adaptation, complete construction and commissioning of an experimental endstation containing a double-sided VMI for spectroscopic studies of ultrafast processes in chiral molecules via PECD.

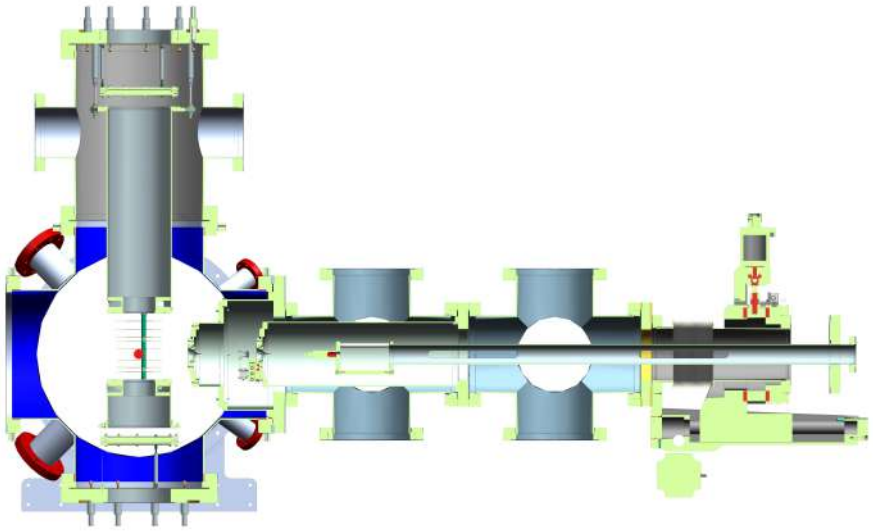

Figure 4.2: Cross section of the experiment. The target is injected at the end of the manipulator (right side) via a pipe (not visible here) into the nozzle of the molecular jet. The arm of the molecular jet ranges until the middle of the second CF160 cross. The target passes two skimmers before entering the interaction region (red dot). The foreseen operation mode is, that created cations are accelerated to the top and electrons to the bottom. The particles hit the detectors and are captured out of the vacuum with a CCD camera on each side.

For such kinds of studies, isolated and cooled molecular targets are required. The first requirement was satisfied by the transfer of the target into the gas phase. The second by a continuous or pulsed supersonic target injection through the nozzle. Molecular beams can be obtained by supersonic expansion of a gas mixture with a pressure of several bars (1 - 10 bar) through a nozzle with a diameter of a few tens of micrometers. Larger nozzles are easier to handle because smaller ones tend to be blocked by already small particles. In contrast, nozzles with larger diameters require more efficient pumping, due to the larger gas load. The here-presented spectrometer was equipped with a continuous supersonic molecular beam source. Figure 4.2 shows the complete setup. The spectrometer was embedded in the main vacuum chamber

(left side). Generally, ultra-high vacuum (1×10^{-8} mbar) is required to enable undisturbed collisions of the target, i.e. molecule, with the photon beam. Hence, collisions with background gas atoms or molecules are minimized, and the background signal in the data is less with a better vacuum. One important general aspect of reaching ultra-high vacuum is a clean working environment in a clean tent, where the clean parts are mounted with clean tools [160]. This was considered and pursued during the build-up. To remove additional water vapor from the inside of the chamber walls, the experiment can be baked up to 120 °C temperature, which is the allowed maximal bake-out temperature for vacuum pumps. For the commissioning of the experiment, a bake-out to achieve the best possible vacuum was not realizable due to time constraints but can be considered for further experiments if needed. For the creation of the vacuum, two Agilent scroll pumps (model IDP-10) and six Agilent turbomolecular pumps (TwisTorr 84/304/404 and 804 FS) were used, which are oil-free and non-magnetic. The first pump property is essential to avoid damaging the MCP detectors. The second property is of utmost importance to ensure the magnetic field is uniform in the interaction region. Magnetic fields should not be perturbed by any ferromagnetic material. Thus, all used materials in and outside the chamber were chosen to be non-magnetic. In the here presented experimental setup, three differentially pumped chambers existed (from right to left): (i) the first molecular beam expansion CF160 cross chamber, which was equipped with one 700 l/s (top) and one 400 l/s (bottom) pump. The continuous supersonic molecular beam was mounted on a motorized CF100 xyz-manipulator (right side in Figure 4.2) and consisted of a stainless-steel tube terminated by a 100-micrometer-sized nozzle. Due to the gas inlet, this region noticed the highest gas load, and needed, therefore, the highest pump power. At the end of this section, which reached geometrically already the entrance of the main experimental chamber, the expanding molecular jet, containing the target, was collimated by passing through the first skimmer [161] with an opening of 250 µm. (ii) in the second molecular beam expansion CF160 cross chamber, a second skimmer with an opening of 500 µm was placed a few centimeters away from the first one and pumped with one 700 l/s pump at the top. (iii) the main experimental chamber was the third pumping section and pumped via a 300 l/s and 80 l/s pump mounted at the top. The pressures were measured with four Agilent Pirani gauges (FRG 730). The double-sided VMI spectrometer, placed in the main chamber, was fixed on the top CF250 flange, which contained a window to image the phosphor screen via a camera and 9 high-voltage (HV) feed-throughs for the connection of the electrodes, drift tubes, and detector components. The ion detector was fixed at the same flange. A second flange of the same kind was mounted on the bottom side of the main chamber, which contained as well 9 HV connectors and on which the electron detector (MCPs plus phosphor screen) were mounted.

On the left side of the main chamber, a Residual Gas Analyzer (RGA) and an additional 80 l/s pump were mounted (not included in this CAD model, but visualized in the "real setup" picture shown in Figure 4.21 at the end of

this chapter).

The photon beam can enter the main chamber through the CF400 flanges (perpendicular to the molecular beam), marked with a red dot. The beam direction is here either into or out of the plane, depending on the experimental environment. After passing the interaction region, the photon beam should end in a beam block, which can be, for example, a small piece of metal reflecting the beam ideally by 45 degrees. Back reflections into the main chamber should be thereby blocked. For pump-probe experiments, one or more additional time-delayed optical lasers can be shot into the chamber through several additionally available ports on one of the CF400 flanges.

4.3 Spectrometer Design and Performance

The sketched double-sided VMI spectrometer (Figure 4.3) contains 8 plane electrodes, 4 meshes, an electron -and ion drift tube and a detector on each side. Electrodes and meshes are made of copper. The detectors are built of three parts: First of chevron microchannel plates, which are two plates stacked in chevron configuration with small tilted micro channels respectively to the surface of the MCP (active area 120 mm, pore size 25 µm, pore distance 32 µm, temporal resolution 2.5 ns FWHM, imaging quality). The charged particles hit the first MCP (front) and generate electrons, which are accelerated by a bias voltage of about a few hundred volts to the second MCP (back), where they generate again electrons by hitting the wall of the channels and amplifying the signal up to an order of 10^6. An electron avalanche is generated, which is then accelerated to the phosphor screen (P47), the second part of the detector. A light dot is caused by the electrons hitting the phosphor screen. The light emission wavelength of the used P47 phosphor screen is 400 nm and has a decay time of 100 ns. The last detector part is a camera with additional magnifying optics. The emitted light is captured outside the vacuum via cameras and transferred to the data acquisition (DAQ) system. All mentioned spectrometer components are foreseen to run under high voltage and therefore separated by thermoplastic PEEK insulators. For the measurements presented in Section 4.3.2, the dVMI was equipped on each spectrometer side with a Basler acA1440-73gm GigE vision camera with a readout of 73 Hz and a Basler lens C23-0824-5M-P f8mm (focal length 8 mm).

Generally, the main challenge is the appropriate voltage setting for fixed electrode diameters and distance between the electrodes. The here presented dVMI is conceptually based on the LAMP dVMI [162] but possesses some modifications: 1. The inner 4 electrodes (no. 2, 10, 11 and 12) were changed from a conical to plane shape because no simultaneous detection of scattered photons and thus no use of large-angle imaging detectors [163] is planned, i.e.

the original reason for installing conical electrodes is not relevant in this case. Furthermore, the closed electrode geometry around the interaction region offers better confined and homogeneous extraction fields. 2. Detectors with a larger active area were installed to increase the detectable kinetic energy range and improve the energy resolution over a given energy window.

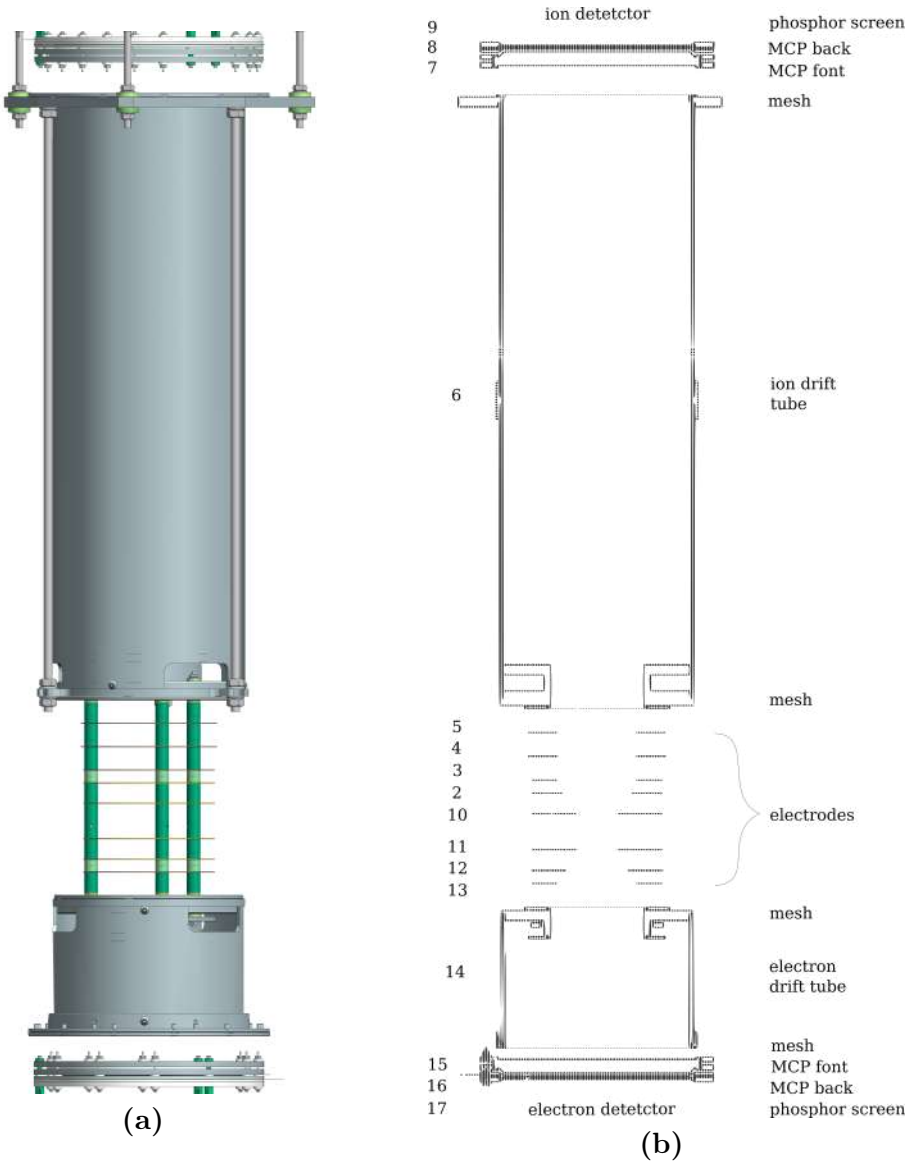

Figure 4.3: (a) 3D CAD rendering of the built dVMI spectrometer. The first element on the bottom is the electron detector. Followed by the electron drift tube (short side) and the electrodes. From the geometrical middle to the top, the ion drift tube is shown. The last element on the top is the ion detector. (b) 2D cut through the center of the dVMI spectrometer (YZ plane) used for the SIMION simulations. High-voltage components 2 - 10 are annotated on the ion side and 11 - 17 on the electron side. Electrodes 2 - 5/10 - 13, 6 and 14 are the particle drift tubes, and 7, 8, 9 and 15, 16, 17 are the particle detectors.

3. Hence, the flight tube diameters were enlarged, to enable a complete illumination of the 120 mm detectors. 4. The detector on the ion side was changed from a delay-line anode [164] (usually used for few-particle detection) to a phosphor screen because the detection of high count rates of several hundred or more charged particles is foreseen, to enable partial covariance analysis [106].

Based on the Eppink-Parker-Design [149], 3 electrodes on each side of a dVMI are sufficient for the VMI mode. To achieve a ToF mode, a homogeneous electric field is needed. This electric field can be produced by using more electrodes. Therefore, the here presented and within this work built dVMI spectrometer can be used, with its 8 electrodes, in the following four electric field configurations: 1. Double-sided VMI, 2. Double-sided ToF, 3. Top VMI & bottom ToF and 4. Top ToF & bottom VMI. Even though it is foreseen to perform the experiments in the double-sided VMI mode, this instrument offers versatile electric field configurations and enables therefore various experimental applications.

4.3.1 SIMION Simulations

To ensure a reliable spectrometer performance, adequate charged particle trajectory simulations are indispensable. Especially for a double-sided VMI spectrometer where the electron and the ion side share a common extraction field. Their performance is interdependent, and hence the right voltage setting is mandatory. Within this PhD research work, the ion and electron optics simulator, called SIMION [165], was used to execute this work. The results of such a computational study ensure the suitability of the dVMI spectrometer for the commissioning and experiments.

In the following, simulations for the four above-mentioned electric field configurations are presented. The electrode resolution in SIMION was set to 0.5 mm per grid unit. Electrons (5 eV, 55 eV and 105 eV) and positively charged ions (5 eV, 25 eV and 45 eV) were chosen to fly in the dVMI spectrometer for the electrode voltage optimization. Charged particles in these kinetic energy ranges are expected, for the foreseen experimental studies. The particle momentum directions (to the right from the center) were set to 45 and 135 degrees regarding the spectrometer axis, initially created at the spectrometer center (0 mm), -2 mm and 2 mm off-axis (y-direction). Red, blue and green lines respectively visualize the particle trajectories over the full solid angle of 4π originating from these source points. Due to the rotational symmetry to the x-axis of the spectrometer and for simplicity, the particle trajectories are visualized only on the right side of the spectrometer. Transverse and longitudinal magnetic fields were not considered in the simulations.

For each electric field configuration, different voltage settings need to be found and used. Hence, the voltages of each component, ranging from number 2 to 17 are mostly different for each of the four cases. The voltages of the MCPs and phosphor screen need to be adapted as well to suit either the VMI or ToF mode. The following detector voltages were used: ion detector $7 = -2300\,\mathrm{V}$, $8 = 5\,\mathrm{V}$, $9 = 425\,\mathrm{V}$ (ToF mode)/ $9 = 3000\,\mathrm{V}$ (VMI mode) and electron detector $15 = 200\,\mathrm{V}$, $16 = 2200\,\mathrm{V}$, $17 = 2500\,\mathrm{V}$ (ToF mode)/$17 = 5000\,\mathrm{V}$ (VMI mode). These and the optimized electrode voltages are additionally listed in Table 4.1.

The first simulated dual mode is the double-sided VMI mode, which produces an inhomogeneous field (forms an Einzel lens) and ensures thus focusing cations and electrons simultaneously on both sides of the spectrometer. Corresponding voltages can be found in the first green column in Table 4.1. The SIMION simulation results are represented in Figure 4.4(a) -(e). Positively charged ions are detected on the top detector and electrons on the bottom one. The top and bottom zoomed-in trajectories are illustrated in Figure 4.4(b) and 4.4(e). Particles with the same initial momentum but different starting locations along the y-axis, visualized in Figure 4.4(d), hit the same spot on the detector, with a maximal tolerance of 0.3 mm. Respectively to the chosen particle energies, which are ascending from left to right in the shown figures, three foci can be seen on each side of the dVMI.

The energy scaling for the dVMI mode is presented in the following. The voltage settings are the same as in Figure 4.4(a). All particles start in the spectrometer center. Cations with energies of 5 eV, 13 eV, 21 eV, 29 eV, 37 eV and 45 eV are filled to the top detector. Electrons with energies of 5 eV, 25 eV, 45 eV, 65 eV, 85 eV and 105 eV fly to the bottom side of the spectrometer. All particles exhibit a momentum to the right. Figure 4.5(b) and 4.5(c) show the corresponding energy scaling with R^2. The following equation is valid for the particle energy:

$$E_{kin} = \frac{\sqrt{p_x^2 + p_y^2}}{2m} = k \cdot R^2 \tag{4.5}$$

with the calibration factor k. The initial particle energies are plotted on the y-axis and the squared radii of the position where the particles hit the detector on the x-axis. In both figures, a linear relation can be seen, as it needs to be the case under "real" dVMI conditions. The k factor can be retrieved via a linear fit and is for the cations and electrons under this specific voltage setting $k_i = 1.40 \times 10^{-2}\,\mathrm{mm^2/eV}$ and $k_e = 1.51 \times 10^{-1}\,\mathrm{mm^2/eV}$, respectively.

Such energy scaling simulations and k-factor calculations are usually additionally performed after the measurement to retrieve for the used voltage settings the pixel-to-energy calibration, which enables transforming the radial distribution measured in pixels into the corresponding binding energies of the measured charged particles. This approach was as well applied in Section 5.5.1 of this work and the result can be found in Figure 5.16.

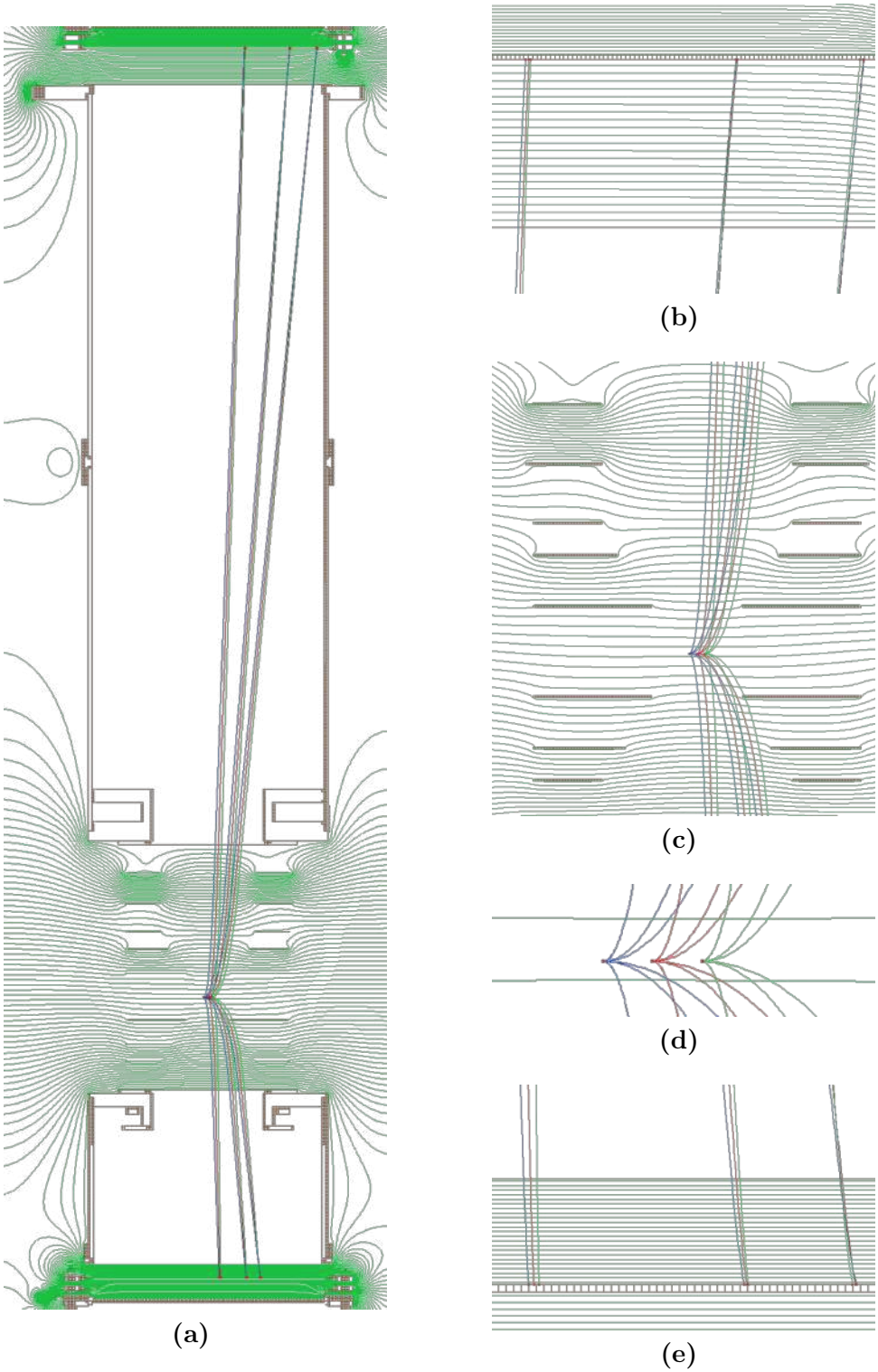

Figure 4.4: Double-sided VMI mode: (a) shows the results of the SIMION simulation. The electric field potential is visualized with green lines. The particles start in the interaction region between electrodes 10 and 11. (b) and (e) depict the collision of the cations/electrons on the detectors. (c) and (d) illustrate in more detail the interaction region and the in y-direction displaced particle creation: −2 mm (blue), spectrometer center at 0 mm (red) and 2 mm (green).

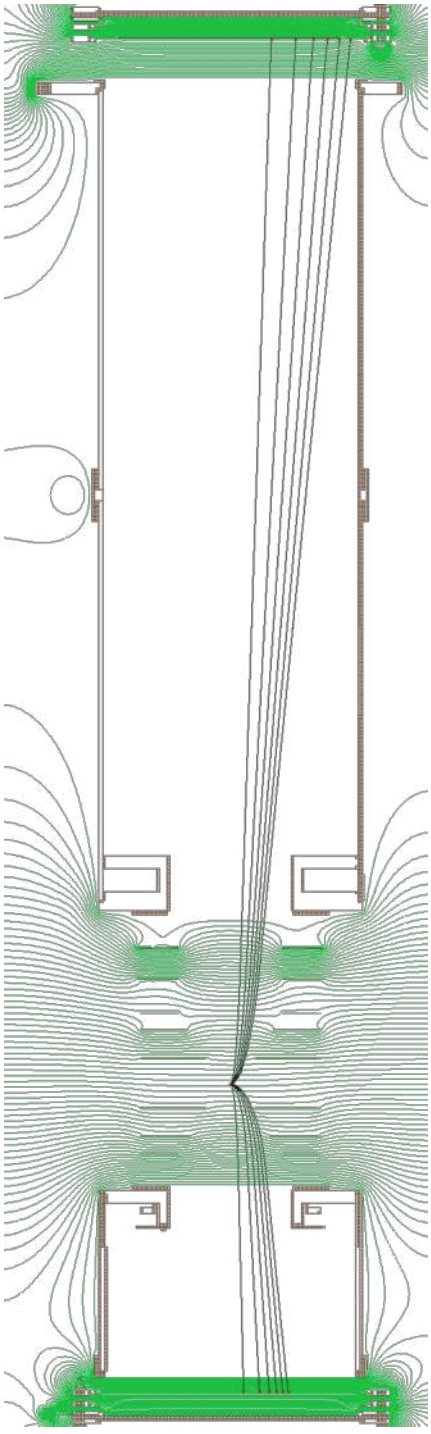

(a)

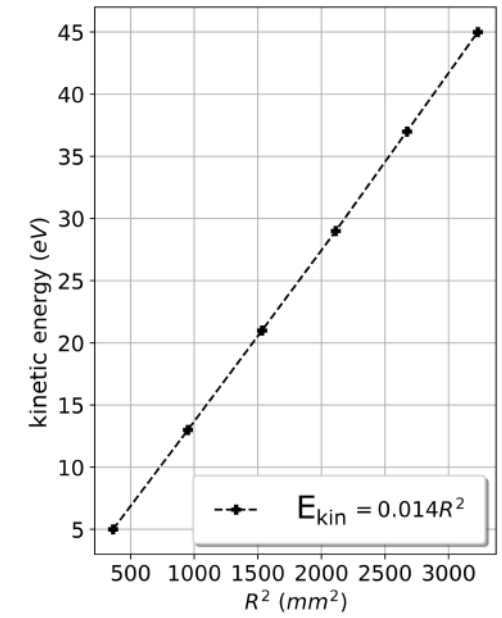

(b)

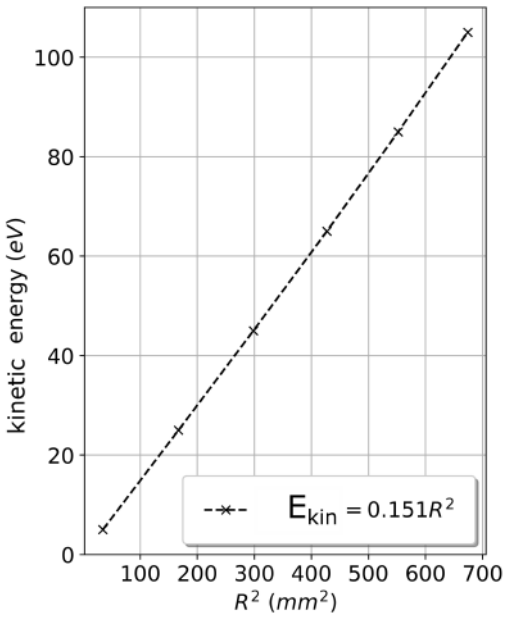

(c)

Figure 4.5: Energy scaling with R^2. (a) shows cations with 6 different kinetic energies hitting the top detector (5 eV to 45 eV, energetically distributed in 8 eV steps) and the electrons focused to the bottom detector (5 eV to 105 eV with an energy separation of 20 eV). (b) represents the ion energy scaling with R^2 and (c) the electron scaling.

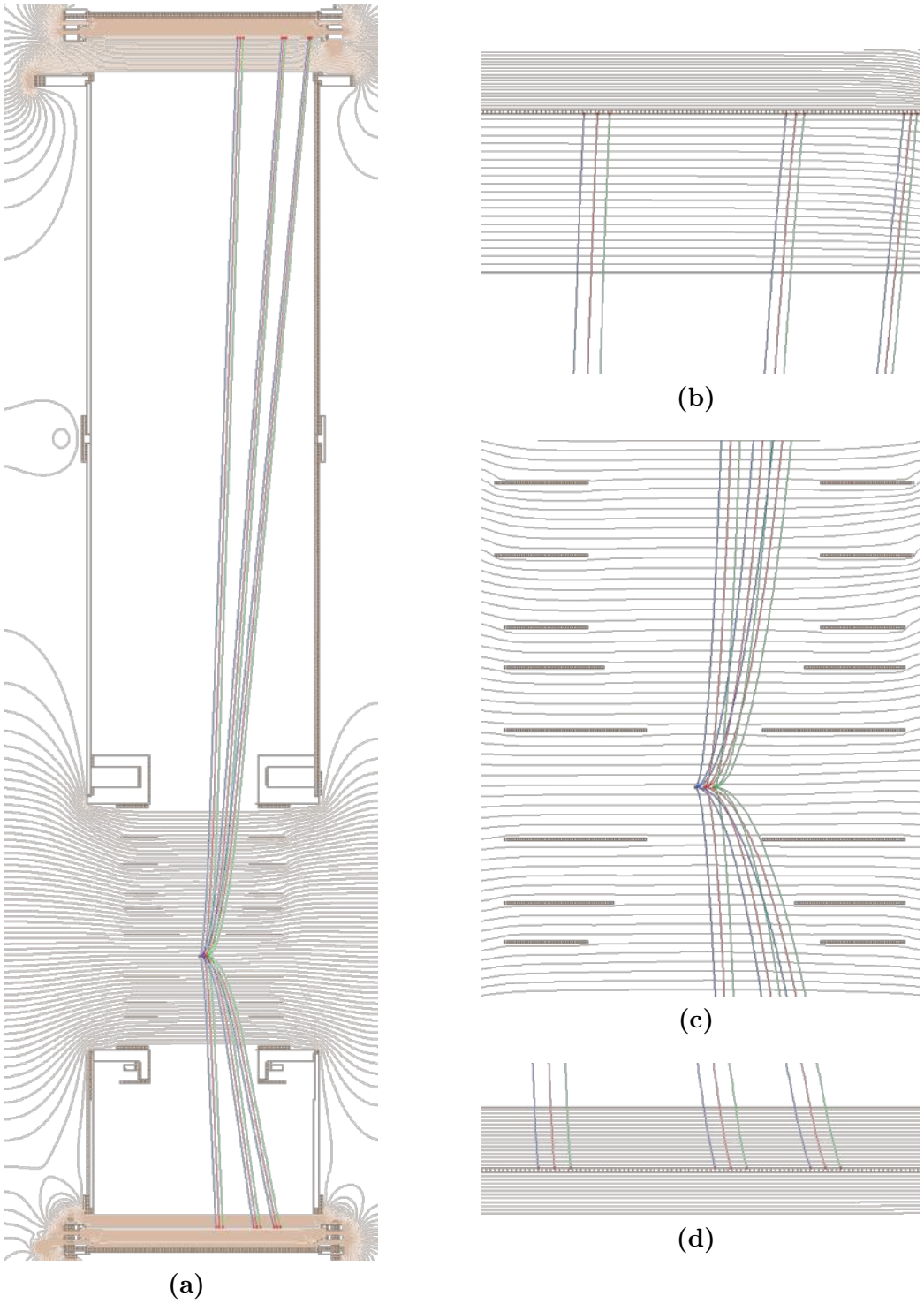

Figure 4.6: Double-sided ToF mode. (a) shows the complete simulation result, showing the whole spectrometer. (b) and (d) are the zoom-ins of the in this case transversally parallel ion/electron particle trajectories hitting the detectors. (c) depicts the interaction region and the homogeneous electric field potential (brown lines) created by the electrodes and corresponding voltages.

The second case, the double-sided ToF mode (dToF), is represented in Figure 4.6(a). The voltages (see Table 4.1, column number 2 in brown) were optimized to create a transversally uniform electric field through the whole spectrometer, visualized with brown lines. Hence, the particles with the same initial momentum, but different starting locations, fly in parallel without any sign of focusing (Figure 4.6(b) and 4.6(d)). In this case, the transverse initial beam spread is exactly mapped onto the detector (XY plane). Thus, the ionizing photon beam becomes visible. This mode is therefore also called spatial imaging mode. The longitudinal initial spread induces due to the differences in flight times only a slight spread on the detector. At the detectors, the largest distance between particles of the same energy is 2 mm with a 0.5 mm tolerance.

For this specific set of voltages, one concrete example for flight times was calculated and is shown in Figures 4.7 - 4.11. Flight times for different cations (singly charged C^+, N^+, O^+, Xe^+, $C_5H_{11}I^+$ and highly charged Xe^{20+} isotopes) with an initial kinetic energy of 10 eV were simulated. The flight times were extracted from the SIMION simulations. For each time of flight, a Gaussian peak with a Full Width at Half Maximum (FWHM) of 5 ns was plotted. This FWHM corresponds to the experimentally expected time response of the 120 mm Chevron MCPs, from where the time-of-flight spectra can be extracted during future experiments. All the time of flights can be resolved, except those for the Xe^{20+} isotopes, which are separated by a mass of 1 atomic unit. This can be seen in the multi-Gaussian fit of Figure 4.7 (red line in the zoom-in) over all four Xe^{20+} isotopes. The two Gaussian peaks for the isotope 131 (filled in light green) and 132 (filled in light gray) are summed up. They are not distinguishable, and will therefore be detected as one single peak. In this specific example using this set of reference voltages, a resolution limitation is reached because the xenon isotopes are not completely resolvable. Nevertheless, the presented voltages were chosen and optimized in such a way that a wide range of singly charged atoms/molecules can be detected and resolved at the same time. To resolve highly charged atoms or molecules, for instance, the Xe^{20+} isotopes, the voltages need to be adapted properly. Taking this example, the electrode voltages on the ion side of the dVMI spectrometer can be reduced by 90 % of the initial values (electrodes no. 2 - 6 and 10, column 2 in Table 4.1). This voltage reduction leads to trajectories that are shifted to the outer part of the detector, thus to longer particle trajectories and longer and better-separated flight times. Thus, the Xe^{20+} isotopes 131 and 132 overlap less. The multi-Gaussian fit shows four separated peaks, which can be resolved (see Figure 4.8). With the low voltage setting, the other cations, which were shown as well in Figure 4.7, are cut out and are not detected anymore. This set of low voltages is hence suited for the investigation of a narrow range of highly charged xenon isotopes. This example shows again the importance of proper simulations before the experiment to get a good starting point for the voltage settings to enable the detection of particles with an energy range, which is expected and of interest within the planned experiment.

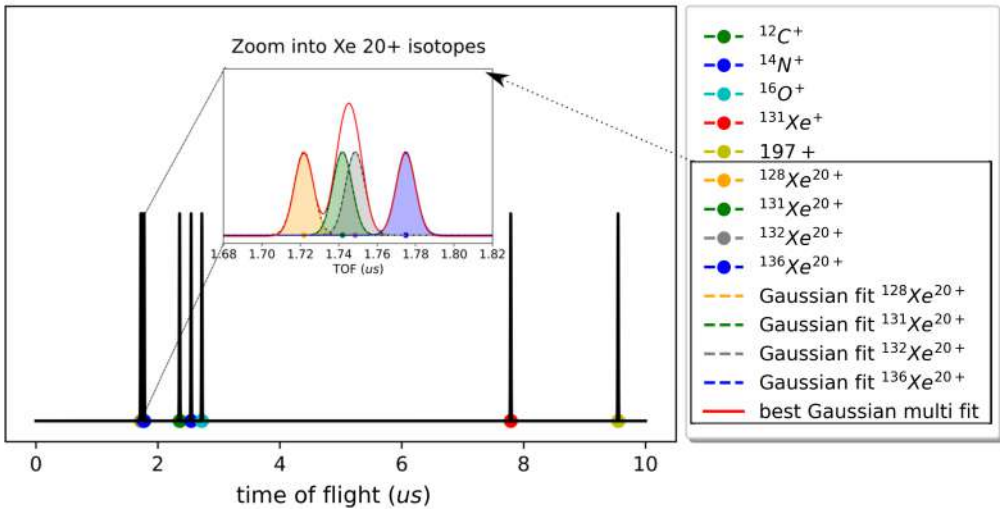

Figure 4.7: Calculated time of flights for different cations with an initial energy of 10 eV using the optimized voltages for the dToF mode (see Figure 4.6(a) and corresponding brown column in Table 4.1). A wide range of cations can be detected and resolved. The peaks in this time-of-flight spectrum are Gaussian peaks with an FWHM of 5 ns, corresponding to the time response of the MCPs. Isotopes with a mass separation of 1 a.u., namely $^{131}Xe^{20+}$ (light green) and $^{132}Xe^{20+}$ (light gray) cannot be detected separately. This is visualized by the multi-Gaussian fit (red line) in the zoom-in figure.

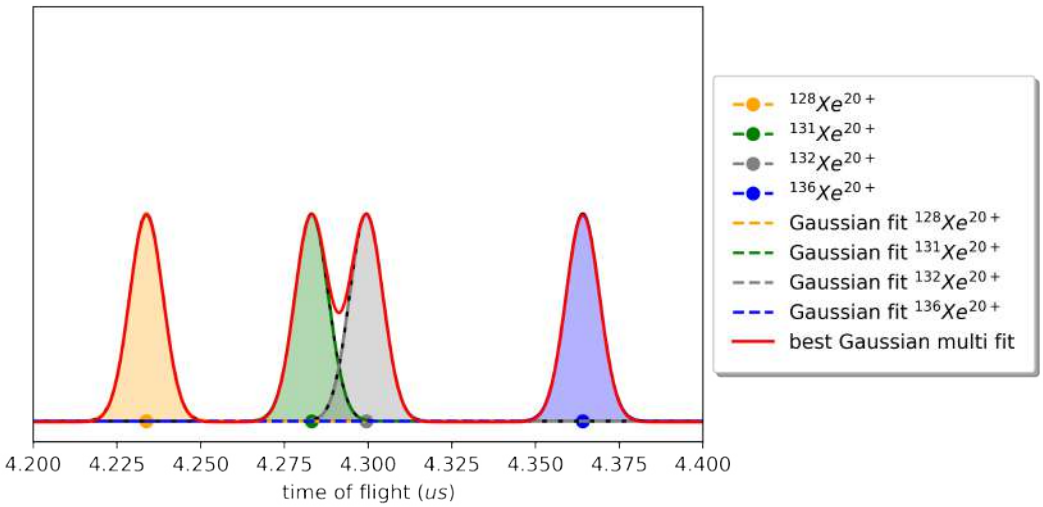

Figure 4.8: Simulated flight times of the Xe^{20+} isotopes exposed to lower voltages on the ion side of the dVMI spectrometer. Electrodes number 2, 3, 4, 5, 6, and 10 were reduced by approximately 90 %. The Xe^{20+} isotopes with a mass difference of 1 a.u. can be resolved.

Time-of-flight spectra can be converted into mass spectra by applying appropriate calibrations. The spectrum in Figure 4.7 was converted into the mass spectrum presented in Figure 4.11. To retrieve the calibration from the time of flight to mass over charge the following step was done. Each time-of-flight value was plotted against the $\sqrt{m/z}$ for the singly charged cations (Figure 4.9) and for the multiply charged xenon isotopes (Figure 4.10). Looking into the two zoom-ins in Figure 4.11, it is noticeable that all the masses, of the singly charged and highly charged atoms/molecules can be resolved. The presented examples are a small inside into the possibilities of the spectrometer in the dToF mode.

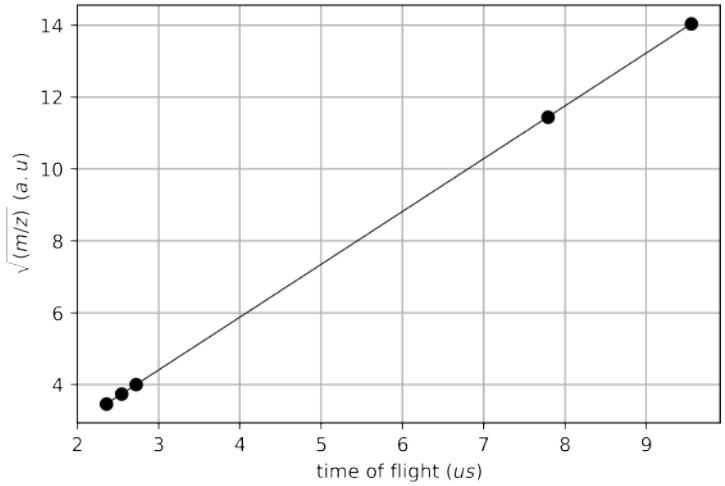

Figure 4.9: The mass-over-charge calibration function is visualized for the singly charged cations C^+, N^+, O^+, $^{131}Xe^+$ and iodomethylbutane $C_5H_{11}I^+$, plotted in Figure 4.7.

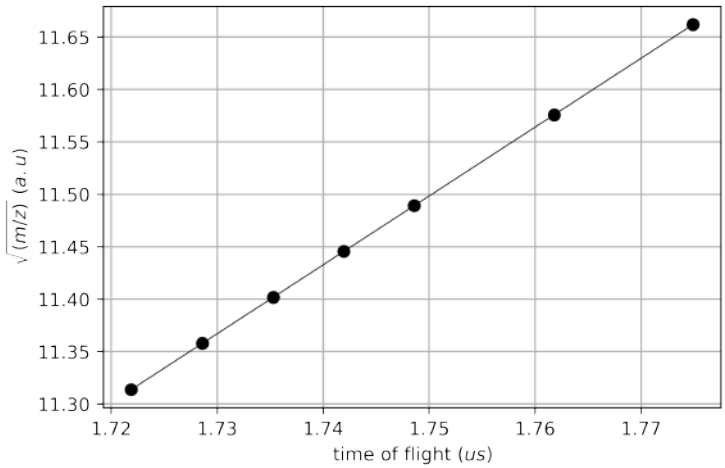

Figure 4.10: Mass-over-charge calibration function for the highly charged Xe^{20+} isotopes 128, 129, 130, 131, 132, 134 and 136, plotted in Figure 4.7.

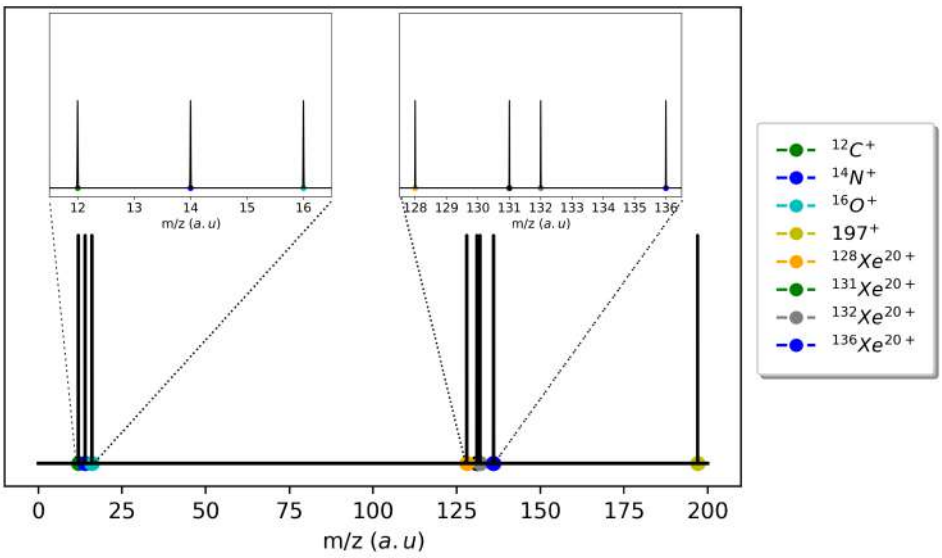

Figure 4.11: Mass-over-charge spectrum for the time-of-flight spectrum presented in Figure 4.7. The two zoom-ins visualize that all the cations can be resolved.

The third case of using the built spectrometer is a combination of the two previous operation modes. Here, the top side detects the cations in the VMI mode. Figure 4.12(b) depicts the top zoom-in trajectories, cations with the same initial momentum, but different starting locations along the y-axis. They fly to the same spot on the detector with a tolerance of 0.4 mm. The bottom zoomed-in electron trajectories show that electrons with the same initial momentum fly in parallel (Figure 4.12(d)). At the electron detector, the largest distance between electrons of the same energy is kept at 2 mm with a 0.1 mm tolerance. To achieve this mode, the electric field needs to be on the bottom side homogeneous (between electrodes 11 and 14) and on the top side inhomogeneous (range between electrodes 10 and 6). Figure 4.12(c) visualizes this effect. The used voltages can be seen in the red column number 3 (Table 4.1). For this operation mode, good simulations are significant due to the interplay of the homogenous and inhomogeneous electrical fields in the interaction region. On the bottom electron side, only three electrodes are available, which are to some extent a boundary because they do not offer many voltage parameters to smooth possible field distortions. This scenario is therefore the most tricky one to realize under real experimental conditions.

Lastly, the fourth case was simulated. Basically, the inversion of case three. The cations are filled in parallel to the top side detector with a maximum separation of 1.5 mm and 0.2 mm tolerance (Figure 4.13(b)).

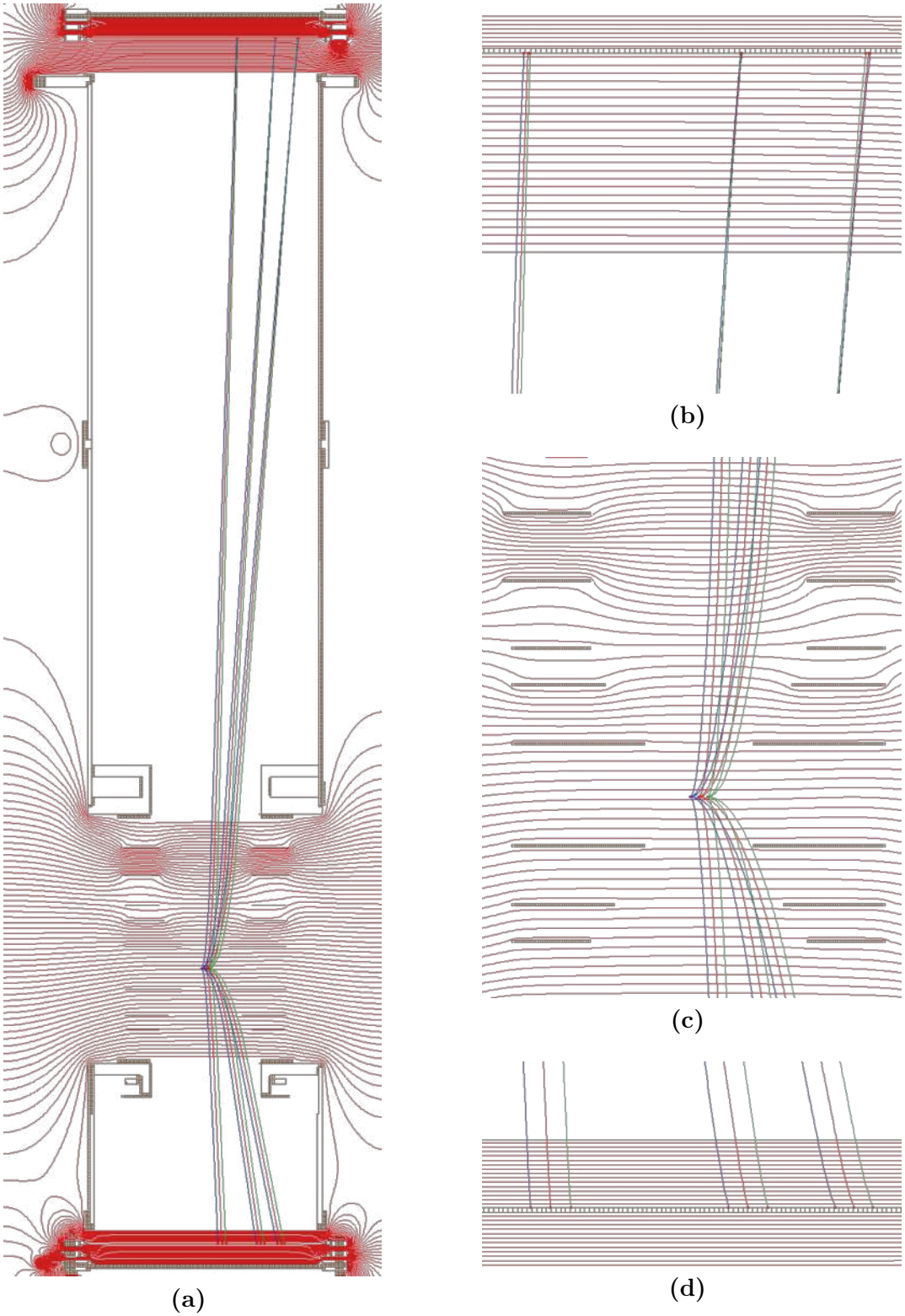

Figure 4.12: Top VMI and bottom ToF mode. Cations with the same initial momentum are focused toward the top ion detector, and electrons fly in parallel to the bottom electron detector. The mixture of homogeneous and inhomogeneous electric fields can be seen in (c).

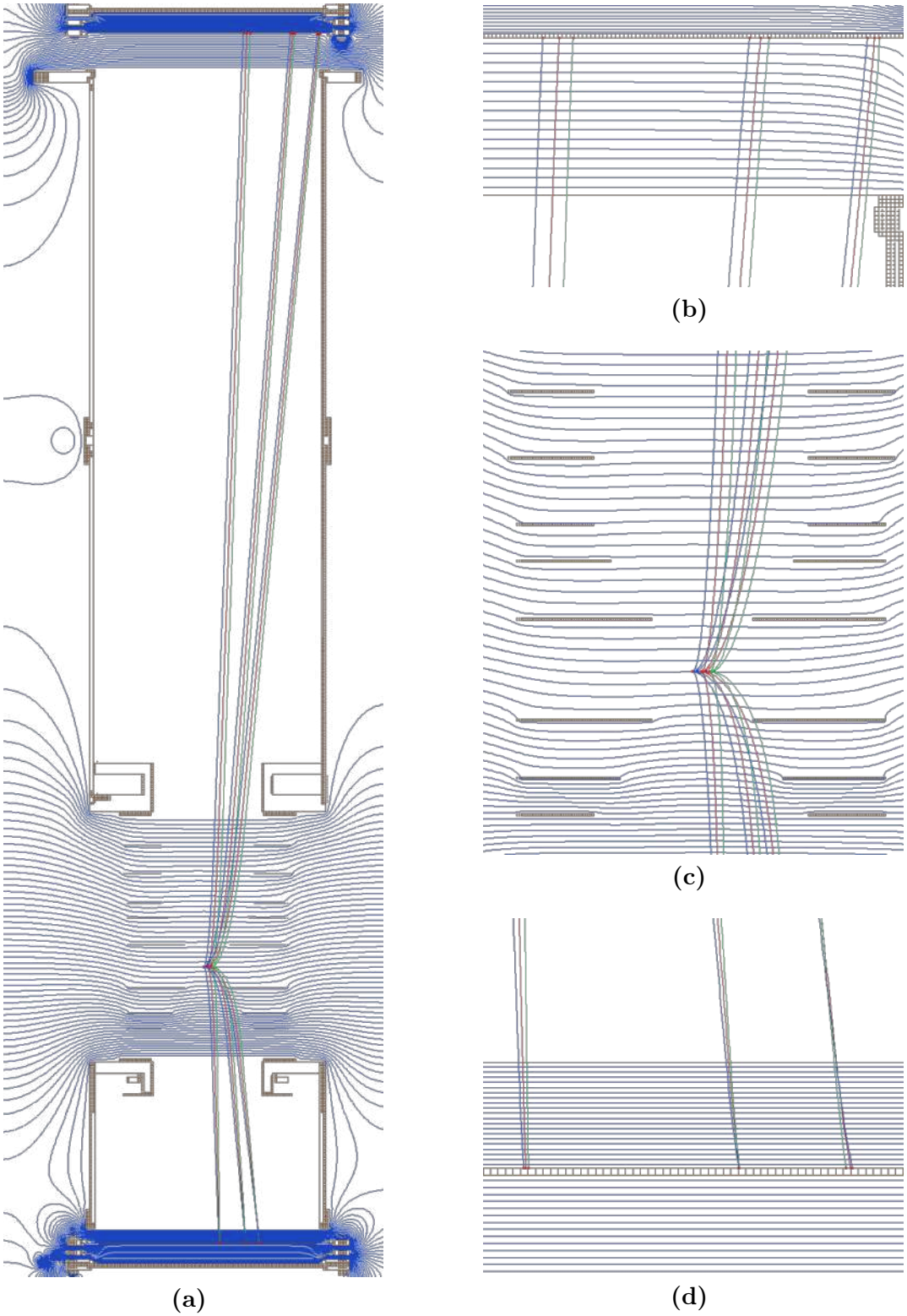

Figure 4.13: Top ToF and bottom VMI mode. (c) the electric field potential is homogenous at the top and inhomogenous at the bottom. Thus, the cations fly in parallel (b) and the electrons are focused (d).

By the production of an inhomogeneous electric field at the bottom side, electrons with the same initial momentum are focused into the same detector point with a tolerance of 0.3 mm (see Figure 4.13(d)). The corresponding homogeneous and inhomogeneous electric fields can be seen in Figure 4.13(c). Due to more electrodes on the ion side, the homogenous field can be achieved more easily in comparison to case no. 3.

To get some first "experience" with the performance of such a spectrometer, it can be helpful to change some voltages manually in SIMION, which was also done within this work. It provided insight, into the sensibility of the electrode voltages, thus which electrodes have the biggest impact on the static electric field and hence the particle trajectories. This simulation step was also valuable for the performed commissioning of the experiment because the voltage fine-tuning was done as well by changing the high voltages manually. This certain performed approach will be elaborated in detail in the next section. But generally, finding voltages from scratch or optimizing them should be performed programmatically. This approach is much more effective, faster, and delivers more precise results. Nevertheless, writing the script and running it, is as well a process with a certain degree of complexity. Here, collaboratively developed (with AMO experimentalists at LCLS) Python codes were used to perform the voltage optimization. An exemplary script can be found in the appendix of this work, presented in Chapter 7.

Electrode no.	**Voltages [V]**			
	1. dVMI	2. dToF	3.t-VMI & b-ToF	4.t-ToF & b-VMI
6	-1454	-1555	-1378	-1116
5	-1434	-1435	-1238	-1000
4	-1034	-1178	-878	-893
3	-944	-1000	-818	-790
2	-934	-900	-776	-730
10	-734	-745	-600	-638
11	-554	-466	-372	-483
12	-474	-304	-243	-370
13	- 294	-201	-161	-233
14	-9	-2	-1	-25
7, 8, 9	-2300, 5, 425 (ToF) / -2300, 5, 3000 (VMI)			
15, 16, 17	200, 2200, 2500 (ToF)/ 200, 2200, 5000 (VMI)			
d = double-sided, t = top and b = bottom				

Table 4.1: Exemplary voltage settings for all four electric field options. Column 0 contains the electrode numbers. Column 1 in green the double-sided VMI mode, which is also correspondingly represented in Figure 4.4(a)-(e) with a green equipotential surface. The double-sided ToF mode is represented in brown in column 2 (Figure 4.6(a)-(d)). Column 3 in red is a combination of the two previously presented voltage settings, top VMI and bottom ToF mode (Figure 4.12(a)-(d)) and the blue column number 4, contains the voltages for the top ToF and bottom VMI mode (Figure 4.13(a)-(d)).

4.3.2 Characterization and Commissioning

The dVMI spectrometer and its complete experimental environment were commissioned at the Metrology Light Source [166] of the Physikalisch-Technische Bundesanstalt (PTB) using the U125 insertion device beamline [167]. All components were first used and the functionality and performance were tested, including the dVMI spectrometer, vacuum system, molecular jet, and the complete periphery (see the image of the experiment, visualized in Figure 4.21). Demonstrated was the ability to perform the spectrometer in different modes on each spectrometer side, the spatial imaging, meaning ToF mode, and the VMI mode (Figure 4.17). Furthermore, it was shown, that two of the four dual modes, presented as well in the simulation chapter, were successfully demonstrated (Figure 4.20).

Mass Spectra and Voltage Tuning

For the performed experiment, cations and electrons were generated by shooting the focused 1 mm x 0.5 mm (hxv) 40 eV XUV beam of the PTB into the main chamber (pressure 1×10^{-7} mbar) and ionizing first the residual gas. Argon was afterward separately injected into the interaction region perpendicular to the XUV beam through the molecular jet with a backing pressure of 65 mbar. The molecular jet contained a 6 mm swagelock pipe and 100 µm molecular jet nozzle, and two skimmer sections of 250 µm and 500 µm, respectively (see Figure 4.2). Both molecular beam skimmers were made of nickel and model 1 from Beamdynamics [161]. The molecular jet alignment was done by moving the xyz-manipulator in such a way to maximize the argon signal measured via the RGA (model: mks microvision 2, mass range 1 - 100 amu). An additional increment of the argon signal was achieved by slightly incrementing the backing pressure of the gas. The common approach, which was also performed here, is to dose the gas until a pressure of 1×10^{-5} mbar is measured in the first molecular jet expansion chamber, i.e. the first CF160 cross holding the first skimmer.

The two mass spectra, delivered by the RGA, are presented in the following two figures. Represented are, the chamber composition, meaning the residual gas (Figure 4.14) and the mass spectrum with the molecular jet turned on, hence additionally injected argon (Figure 4.15). Each mass spectrum is normalized to its highest peak, in both cases the water peak at 18 m/z. Water adheres much more to chamber walls than other gases, for example, nitrogen, oxygen or argon, and is, therefore, worse to pump out of the chamber. Generally, water can be reduced substantially by a bake-out of the chamber, which was not performed due to the short preparation time. Different in both figures is the prominence of the H_2^+ peak at 2 m/z. This can be explained by the different time sequences of measurements, meaning that the chamber was not

pumped for the same amount of time. Usually, after closing the vacuum chamber, the most prominent peaks are nitrogen, oxygen, and water. After some pumping time of several hours, RGA retrieved mass spectra show in general more H_2^+ cations. The mass spectrum in Figure 4.14 was recorded after venting the chamber and obtains, therefore, a lower H_2^+ ion yield. All other peaks, C^+, Ne^+ and O_2^+, are in both figures less abundant. The Ar^+ peak appears only in the mass spectrum, where argon was added on purpose. The ratio of O_2^+ and N_2^+ is 0.015 and 0.016 in the mass spectrum without and with argon, respectively. A leak in the chamber would lead to ratio values of $\geq$0.25, which is not applicable here. From the RGA data, solely information about the types of charged ions can be extracted. This data was used to tune the signal and to check the functionality of the molecular jet. It is an important tool within the commissioning process and during the preparation time of an experiment. During the measurements, the RGA was switched off, due to the high amount of additionally produced charged particles, which would otherwise lead to an increased and disturbing background.

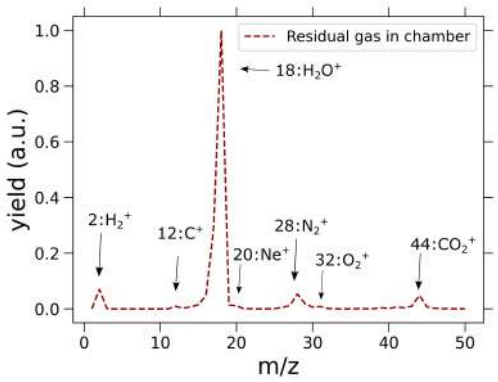

Figure 4.14: Mass spectrum retrieved via the RGA. All peaks represent the components of the residual gas in the chamber.

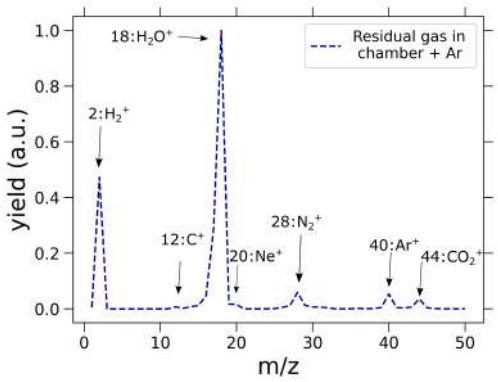

Figure 4.15: RGA mass spectrum with argon. Argon was injected additionally via the molecular jet into the experimental chamber.

After characterizing the target composition via the RGA, voltages on the electrodes of the dVMI were applied to detect cations and electrons. Therefore, the simulated voltages, shown in Table 4.1, were used as a starting point. These values delivered a good start, which was indispensable due to the large parameter room of 12 voltage parameters (see Figure 4.3(b)). Nevertheless, fine-tuning was done manually by changing the electrode voltages. The adjustment of the electrode voltages was started by changing firstly one of the two inner electrodes, number 10 or 11, which act as the extractor electrodes and are the closest ones to the interaction region. The electrostatic field created by all dVMI electrodes, changes the most, by the voltage change of these two innermost electrodes. Afterward, the next closest electrode of each spectrometer side was optimized. Small voltage changes influence the particle trajectories significantly and result in a better or worse imaging condition. In the figure se-

ries of Figure 4.16 the change of the electric field and consequently the particle trajectories via the two inner electrodes is visualized.

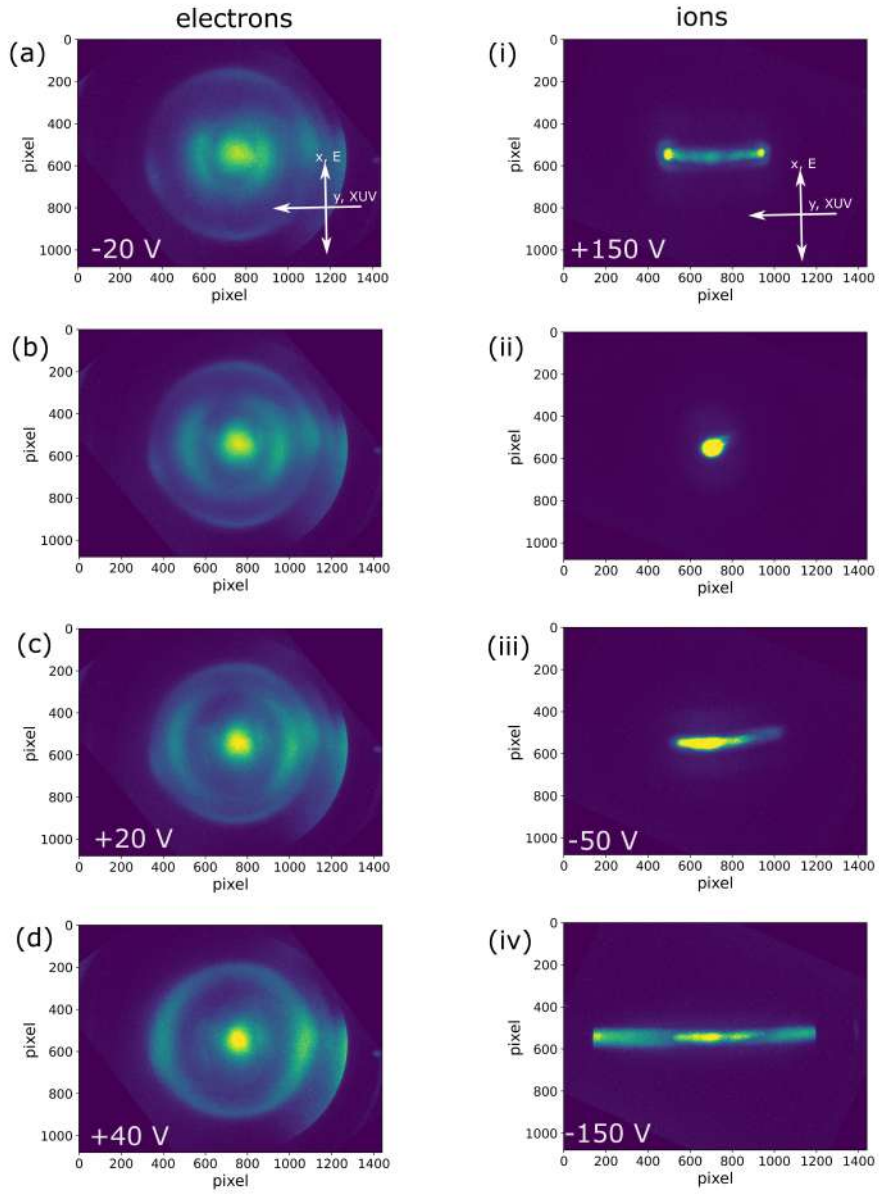

Figure 4.16: Detuning examples: (a-d) electron defocusing by changing the first electron lens no. 11. The starting voltage conditions delivered the in (b) visualized focused electrons. (i-iv) represent the cations, which are defocused from the optimum, visualized in (ii), by changing the voltage of electrode no. 10.

Each presented image, within Figure 4.16 and all other recorded images presented next within this section (Figure 4.17 - 4.20), contain x and y-axes

in the unit pixel and include a white cross, which shows the linearly polarized XUV beam path and the direction of the corresponding electric field $\vec{E}$ of the XUV beam. These images show how easily the conditions can be detuned by small voltage changes. The second image of each column, (b) and (ii), represent exemplary the optimized starting condition within each measurement series, even though the electrons in (b) were not focused perfectly within this measurement. The two column-wise presented measurement series, were performed independently. Hence, each spectrometer side was optimized and run separately.

In the case of the electrons (left column of images, Figure 4.16(a)-(d)), only the voltage of electrode number 11 was changed in 20 Volt steps. The decrement of 20 V induced a smearing or so-called defocusing of the particles, see (a). This can be seen by comparing the inner dot and the two half circles around the dot of (a) and (b). On the contrary, the increment of the voltage by 20 V or 40 V led to the movement of the two inner half circles to the outer part of the detector, which is depicted in (c) and (d), respectively. In the case of the cations (right column of images, Figure 4.16(i)-(iv)), solely the voltage of electrode number 10 was changed by -50 V and $\pm$ 150 V. This example shows that the modification of one voltage enables even a mode change, from the optimized VMI conditions shown in (ii) to for example the spatial imaging mode (iv) or a combination of both modes, (i) and (iii). Finding optimal voltage settings is not trivial.

Spectrometer Operation in the Single Mode

One important step of the commissioning was to test the performance of each side of the spectrometer independently, meaning that only voltages for one side were optimized. Figure 4.17 shows the feasibility of performing each side either in VMI or spatial imaging conditions. The cations are represented in Figures (a) and (b) and the electrons in (c) and (d). The orientation and direction of the XUV beam along the y-axis and its perpendicularly electric field along the x-axis are visualized in the bottom-right corner of (a). Besides, the XUV beam orientation can be identified in the spatial imaging mode (b) and (d) and is here additionally marked with the gray dotted arrow in (b), defined as $\phi = 0$. This angle ϕ lies in the detector plane XY. The spatial imaging mode in (b) and (d) was used to adjust the beam into the middle of the dVMI spectrometer by steering the XUV beam and thus moving the line in the middle of the detector. Furthermore, the bright hello in Figure (d) comes most probably from additional electrons, which are produced by the at the beam block back-reflected and a much larger XUV beam. This back-reflection led to a larger background in Figure (c) and was corrected by mirroring the left half of the image. The averaged and uncorrected image can be found in Figure 7.1 in the appendix in Chapter 7. All presented images within this

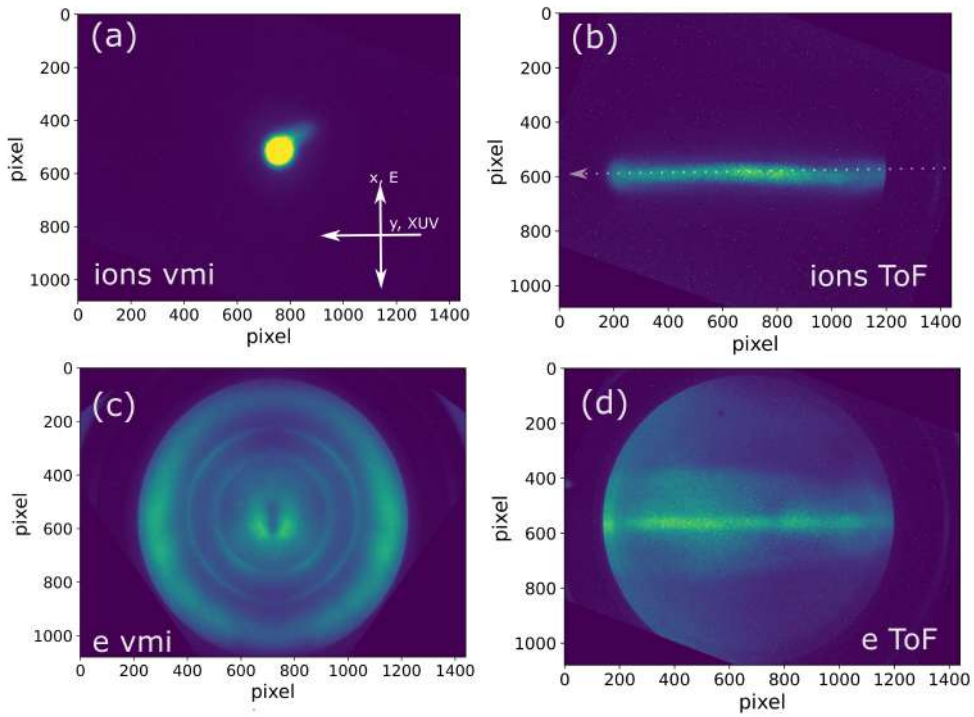

Figure 4.17: Demonstrated single-mode operation of the spectrometer. Top: (a) cations under VMI conditions and (b) cations in the spatial imaging mode. Bottom: (c) electrons under VMI conditions and (d) in spatial imaging mode.

chapter are already corrected regarding rotation. They were rotated within the data analysis by an angle of $\phi = $-21 degrees, which was induced by the randomly orientated camera, which was not avoidable due to fixed holes in the window flange. An additional angle, of approximately $\phi = 2$ degrees, was used intentionally and corrected as well within the image processing. The reason for the usage of this intended angle was to avoid a collision of the XUV beam with the PEEK insulator rods passing through each electrode (see Figure 4.3(a)), meaning, that the XUV beam entered the experimental chamber not perfectly perpendicular to the molecular beam axis.

Before all measurements, the camera positioning and lens focus were adjusted and checked on both spectrometer sides, doing the following steps: The lens, which was directly attached to the camera, was firstly mounted approximately 8 cm away from the outer non-vacuum edge of the CF250 window flange with the HV connectors (see Figure 4.2). This number was calculated by considering 1. the focal length of the lens, 2. the size of the phosphor screen and window flange, and 3. the relative distance between the phosphor screen and the outer edge of the window flange. Moreover, the cameras were implemented in LabVIEW, which was used as a DAQ system, offering online analysis (visualizing and averaging images) and the possibility to record

the camera images. The lens aperture was completely open. The complete fine-tuning procedure was performed using the visible light from the experimental hall, which entered through all window flanges. The camera itself was shielded, and thus only light from the window flanges was acquired. The phosphor screen and the surrounding holding could be imaged via the camera. The lens was moved slightly manually in such a way as to be parallel to the phosphor screen, which was checked by looking at the camera image, which imaged the edge between the phosphor screen and its holder (plane to plane offset of 3 mm). The tilt was performed so long until the complete phosphor screen edge (360 degrees) seemed to appear similarly sharp. Afterward, the lens focus was moved slightly manually to achieve the best focus at the phosphor screen edge and the complete chamber, including all window flanges, was shielded against the light coming from outside. The cations (Figure 4.17(a)) were focused into a dot with a diameter of 129 x 136 pixels^2. 1 mm are 8.84 pixels, which delivers a 14.59 mm horizontally and 15.38 mm vertically large beam. All positively charged ions were focused around the center due to their initial low velocity. This image represents an example of good VMI conditions. Generally, on the top side of the spectrometer, foreseen for the ion detection, also a smaller detector could be used, due to the usually small kinetic energy range covered by the particles. This can be considered for further experiments, especially in the light of the tremendously increased prices for spare parts.

In the following, two exemplary measurements, performed in the single-side mode, and their analysis will be presented in more detail. First, Figure 4.18 shows further analysis of the electrons under velocity map imaging conditions, which were already shown in Figure 4.17(c). Second, presented in Figure 4.19 is an additionally recorded measurement for cations in the VMI mode.

Electron Data

For the electrons in the VMI mode (Figure 4.17(c)) one exemplary more in-depth analysis was performed, and the result is presented in Figure 4.18. First, the averaged image, which contains the 2D electron momentum distribution, was rotated additionally by 90 degrees, to ensure that the XUV beam path is orientated along the vertical image axis. Second, the image was centered properly. Afterward, the Abel inversion was calculated out of the 2D projection of the image, using the PyAbel library and the inversion method rbasex in Python. The inverse Abel transformation (right-half of upper left Figure 4.18) visualizes one 2D slice of the calculated 3D cylindrical symmetric distribution. The upper-right plot shows the normalized radial speed distribution, which is a horizontal slice at pixel position 0 of the Abel-inverted image. By zooming into the plot (not shown here), two peaks can be seen in the radial pixel range between 310 and 350. Nonetheless, in the averaged image (left-half of the upper-right image) no indication of two rings can be seen and the difference in

intensity is small. These two peaks are most probably an artifact. The angular distribution is therefore calculated for the radial region between 325 and 340 pixels (marked via blue-dotted lines in the top-right image) covering both peaks and is presented in the two bottom figures. Once represented in Cartesian coordinates (bottom left) and second in polar coordinates (bottom right). The data results in a beta parameter of $\beta_2 = -0.08$. Due to machine problems, it was not possible to change the photon energy. Therefore, no check was performed to see if the ring is energy-dependent and if so to which element it belongs. Nevertheless, this beta parameter could correspond to our best knowledge to O_2^+. The used photon energy of 40 eV was high enough to photoionize several components of the residual gas. But only the molecular oxygen $2\sigma_u$ orbital with a binding energy of $E_{bin} = 29.82$ eV [168] has an anisotropy parameter β_2 close to 0 [169] and agrees with the here analyzed and retrieved experimental results.

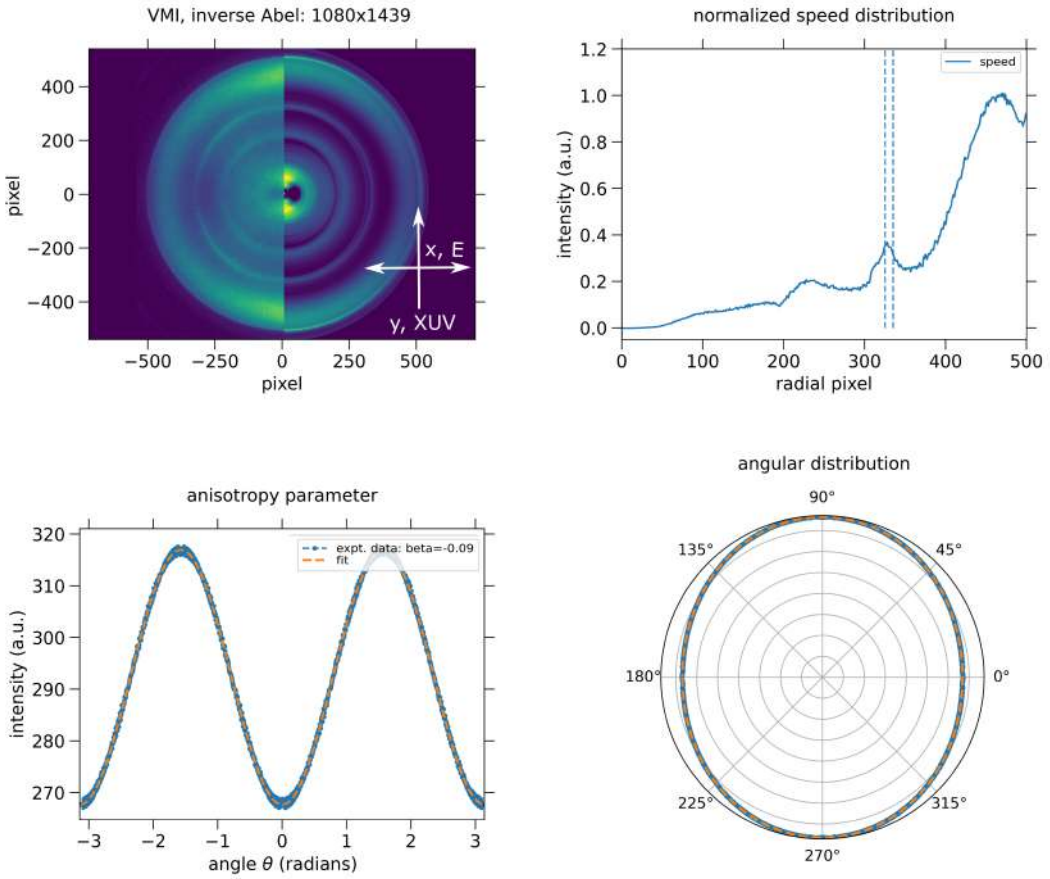

Figure 4.18: Abel inversion of electrons detected at the bottom side of the dVMI spectrometer during single-mode operation. Upper left: 2D projection (left half) and the via PyAbel retrieved 2D slice of the calculated 3D distribution (right half). The radial distribution is plotted in the upper right. The angular distribution of the blue-dotted lines marked region is represented in the bottom subplots, in Cartesian and polar coordinates (left and right, respectively).

Ion Data

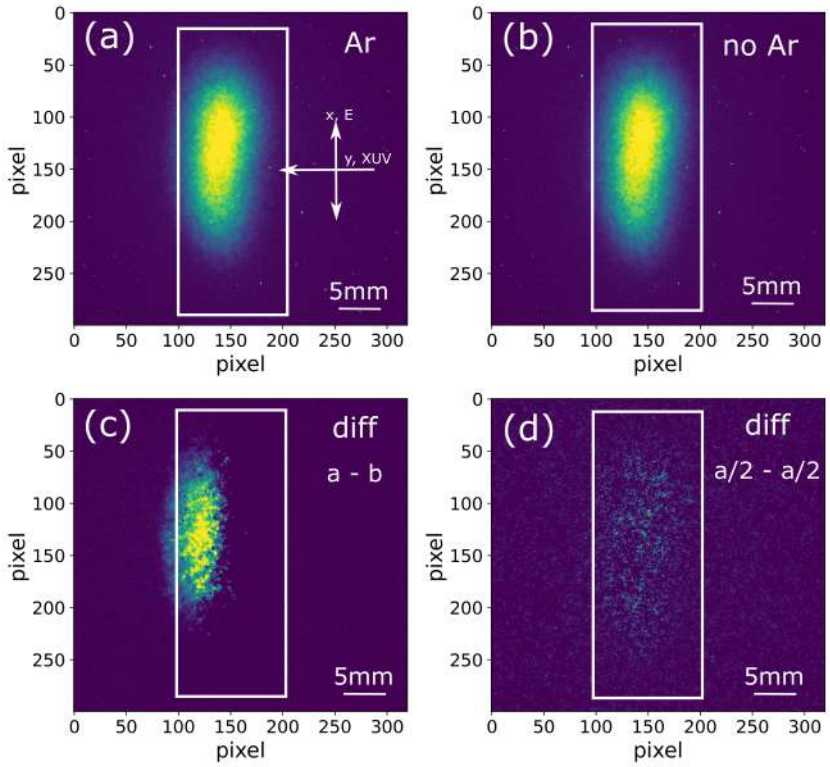

Figure 4.19: Argon cations: (a) shows the detected cations of the residual gas and the via the molecular jet in addition injected argon. (b) with the closed molecular jet, hence no argon. (c) shows the difference of both upper images, which visualizes only the argon cations. (d) shows the difference between the first half minus the second half of the images of (a).

One additional ion measurement was performed in the VMI single-mode operation, using the molecular jet with argon. Data were recorded first with an open and second with a closed molecular jet, see Figure 4.19(a) and (b), respectively. The images were normalized in time and against the ring current of the MLS as a directly proportional value for the intensity on the target. Generally, by subtracting both images of each other, only focused argon cations should be seen. This is the case for the presented data, the argon cations can be separately imaged, as shown in (c). As a cross-check, the first and second half of the images of Figure (a) were taken and subtracted from each other. The difference is shown in (d) and counts a few hits, which are randomly distributed and obtain the same center of mass as Figures (a) and (b). Figure (c) stands out by a left-shifted center of mass. This can be explained by the fact, that the argon cations were focused into a different point due to their larger velocity gained from the supersonic expansion within the molecular jet.

Dual-mode Operation of the Spectrometer

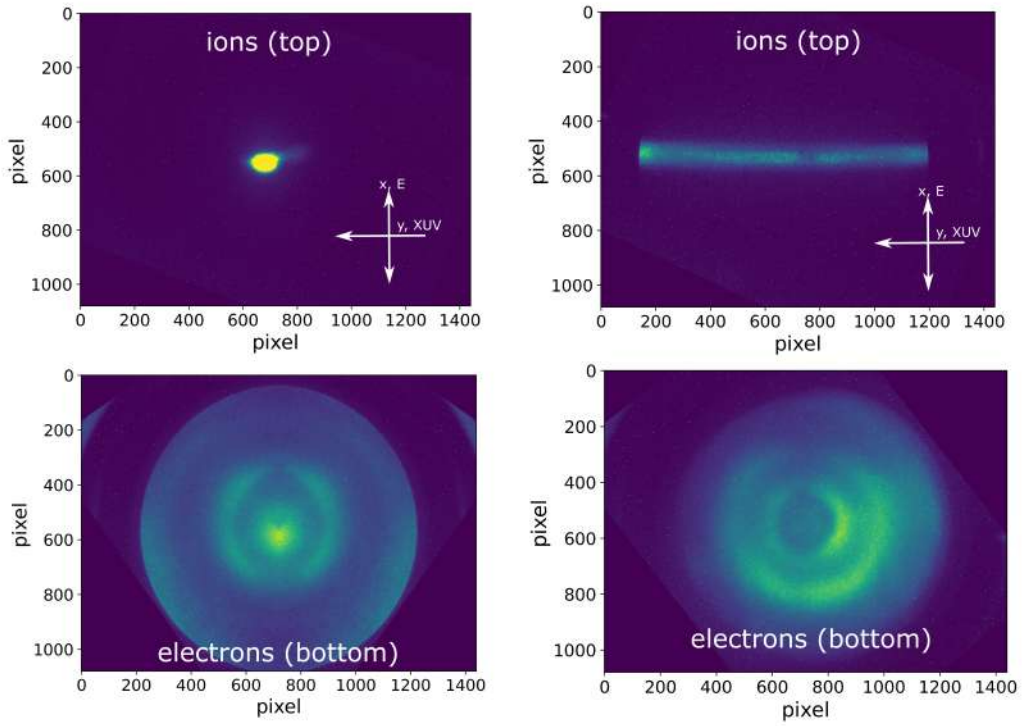

(a) double-sided VMI **(b)** top ToF and bottom VMI

Figure 4.20: Dual-modes: (a) cations and electrons are focused on each side of the spectrometer. This is the experimental demonstration of the simulated case number 1, the dVMI mode and the main operation mode of the spectrometer. (b) cations are detected in spatial imaging mode and the electrons under VMI conditions (simulated case number 4).

The main goal of the commissioning was to perform the dVMI spectrometer in dual-mode operation, meaning that the voltages on both spectrometer sides are optimized to detect the cations and electrons simultaneously within one measurement. As already shortly mentioned before, two of four possible dual-mode operations were successfully demonstrated and are shown column-wise in Figure 4.20. Figure (a) shows VMI conditions on both spectrometer sides and represents case one of the simulation series, which is as well the foreseen standard operation mode of the spectrometer. Figure (b) on the right side visualizes the recorded data for the cations in the spatial imaging mode, detected on the top and the electrons under VMI conditions, detected on the bottom. This operation mode corresponds to the fourth simulated case. Noticeable here, for both VMI electron images, are circles with a broadening. This is a hint for improvable voltage settings. Better focusing was, for example, achieved in Figure 4.18. Furthermore, the under a different

angle back-reflected XUV beam, which was identified already above in Figure 4.17(d), induces again an asymmetric background, which can be identified in the electron image of Figure 4.20(b). Here, the intensity, on the bottom-right side of the image, shows increased values. This effect was corrected in the electron image of Figure 4.20(a) via mirroring the left half of the image, due to a much higher prominence. The averaged, and uncorrected image can be found in Figure 7.2 in the appendix in Chapter 7.

Due to time limitations, further voltage optimizations were not possible. Besides, the usual procedure to check the origin of focused particles, which enables moreover to perform a pixel-to-energy calibration in the post-analysis, is to change the photon energy. This was as well not doable because of an emergency shut-down of the complete MLS facility during the beamtime.

All above-presented results of the first performed commissioning of the dVMI spectrometer, include recorded and analyzed camera images and RGA mass spectra. It should be noted, that for further studies, the additional extraction of the time-of-flight spectra for cations and electrons out of the MCPs, which can be realized by using the already available out-coupling boxes, is recommendable. It delivers useful information about all detected particles during performing the measurement. However, RGA data represents only the composition of ions and cannot be used during the measurement because of the large amount of additionally created particles, which over-saturated the detectors and increased the background signal tremendously. The reason for not recording the time-of-flight data during the here-performed experiment was the too-high repetition rate of the MLS of 550 MHz, which would deliver an overlap of single traces of several hundred spectra. To record the electrons and cations, repetition rates lower than approximately 2 MHz and 100 kHz, respectively, would be required.

To sum up, the spectrometer is not fully commissioned, but the presented results highlight the basic functionality. All components are operational. The experiment's molecular jet is fully functional. Performing the spectrometer on both sides in single mode was proven, and the apparatus can therefore be used as well as a classical velocity map imaging spectrometer detecting electrons or cations separately. Besides, the simultaneous measurement of electrons and cations, using the dual VMI mode, was presented. This correlation operation paves the way to partial covariance methodology without any limitations. The complete portable experiment does not need any modification, so far, and is ready for the next experiment.

Image of the Experimental Setup at the PTB

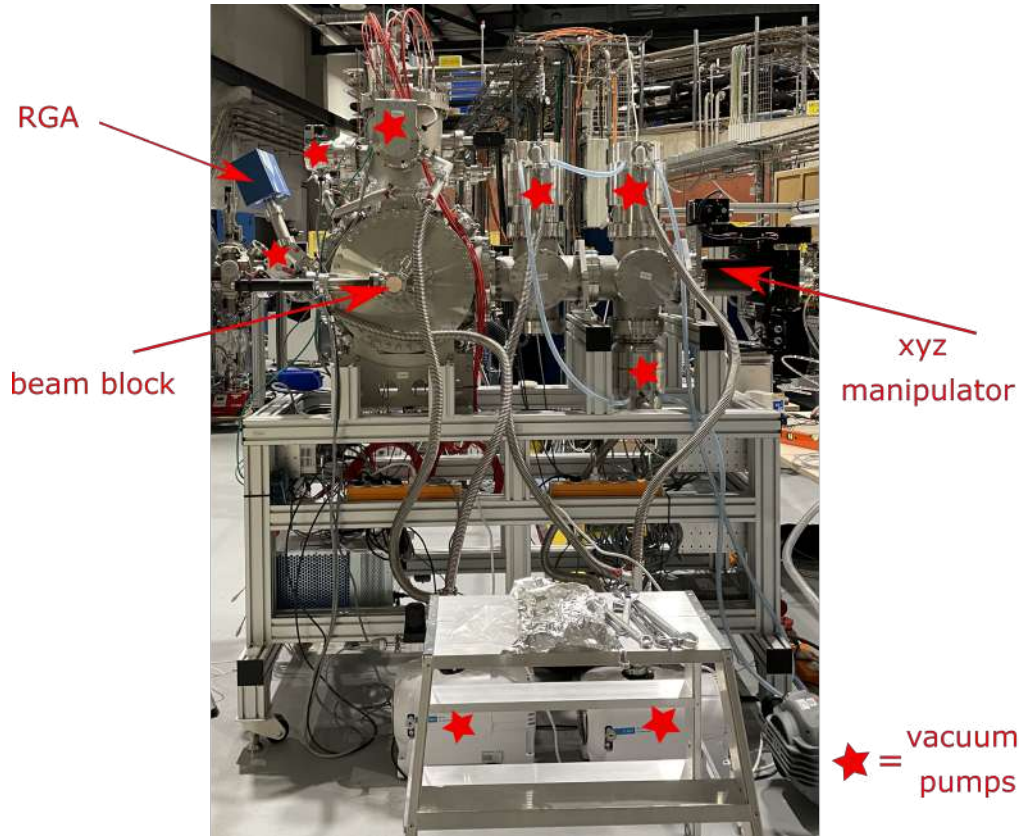

Figure 4.21: Image of the experiment at the PTB (upstream view). Visible are the manipulator, the two molecular beam expansion chambers, the main experimental chamber, red high-voltage cables, the beam block, RGA, vacuum pumps, water cooling/vacuum periphery, and the Rose+Krieger experimental stand containing the vacuum pump controller and high-voltage supply.

Chapter Five

Optical Laser and FEL Pump-Probe Study on Iodomethylbutane

Parts of this chapter will be submitted for publication in Music. V et al., "Wavelength-Dependent Photodissociation of Iodomethylbutane", App. Sci. 2024. Another part has been published by Allum F. et al. in "A localized view on molecular dissociation via electron-ion partial covariance" (Communications Chemistry 5, 42, 2022) [106] with the author of this thesis in a co-leading role. Furthermore, all here presented plots, if not explicitly otherwise declared, were programmatically analyzed solely by the author of this PhD thesis.

5.1 Introduction

Intense optical laser pulses can be used to excite ground-state molecules and thereby induce electronic and/or structural changes in the molecule. Experiments performed via an OL-pump FEL-probe scheme [85] allow for probing individual OL-induced dissociation dynamics with a time-delayed FEL-probe pulse. Depending on the chosen molecule and OL wavelength, intensity, and bandwidth, various fragmentation channels can be addressed. These various channels, reduce the probability and measured signal of the channel of interest and create additional complications in the already complex data analysis. It is therefore advantageous, to induce predominantly a controlled dissociation channel via the OL, for example by dissociating a specific (unique) element governing the fragmentation dynamics, which is then specifically probed at

different times during the fragmentation process via the FEL pulses. Neutral dissociation via distinct resonance excitation, thus where both, the dissociating atom (element of choice) and its mother-fragment, mainly stay in their neutral ground states, can be a particularly intriguing mechanism in this regard, since it is less complex and thus, theoretically, well accessible.

Here presented are, the investigation and comparison of OL-induced fragmentation patterns of the chiral molecule 1-iodo-2-methly-butane ($C_5H_{11}I$) resulting from UV (267 nm, 4.6 eV) or NIR (800 nm, 1.6 eV) pulses in order to obtain a broad basis for future studies of chiral dynamics in this prototypical molecule with free-electron lasers. For both OL wavelengths, intensity-dependent ion yields have been obtained to identify different regimes of fragmentation into neutral and charged fragments. In a subsequent step, specific dynamics were predominantly selected via the experimental conditions in terms of FEL photon energy and intensity, as well as OL intensity and wavelengths. The spectroscopic technique of velocity map imaging allows for ion and electron yield measurements and also kinetic-energy and angle-resolved data interpretation. The FEL photon energy was chosen to predominantly ionize the iodine 4d shell of the neutral and the charged molecule and the respective fragments. The respective changes have been investigated for their ultrafast time evolution using two different XUV-FEL photon energies, i.e. 63 eV and 75 eV.

Mainly, two cases were distinguished in this study, i.e. dissociation of a neutral and a charged iodine atom from the remaining mother fragment C_5H_{11}. In the neutral case, the transition from bound iodine in the molecular environment to its isolated atomic form leads to binding energy changes of the 4d electrons by ~ 1.7 eV [106]. For the fragmentation forming singly-charged iodine cations, a binding energy change of the iodine 4d-electrons of about 12 eV from the neutral molecule to the isolated iodine cation was calculated via ΔCASSCF modeling (averaged over the two spin contributions). The FEL energies were chosen such that the emitted photoelectrons in both cases match roughly the same kinetic energy, which potentially allows for the comparison of stereochemically induced emission asymmetries. Most importantly, in both probing scenarios, the 4d ionization will be followed by an Auger-Meitner decay that creates an additional charge at the iodine. The radiative decay of the inner-shell vacancy via fluorescence cannot be detected in this experimental scheme and is neglected for this study.

The original goal of the here presented and proposed study was to measure the time-resolved photoelectron circular dichroism of the prototypical chiral molecule close to the I 4d edge as observer site during OL-based fragmentation, the increasing internuclear distance between the photoelectron source, i.e. the observer of the system (iodine), and the remaining molecular structure, using circularly polarized FEL photons. Even though the experiment was prepared and performed in the light to detect the PECD-strength changes, no asymmetries could be identified, most probably due to the low

repetition rate of 10 Hz, resulting in lacking statistics that hindered an unambiguous determination.

5.2 Specifications and Photochemistry 1-iodo-2-methyl-butane

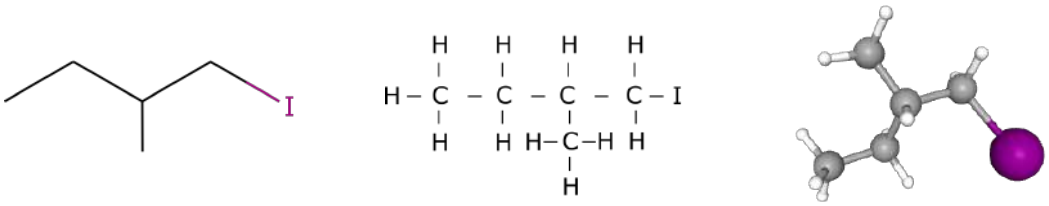

(a) **(b)** **(c)**

Figure 5.1: Chemical representations of 1-iodo-2-metyl-butane ($C_5H_{11}I$): (a) skeleton diagram, (b) Lewis structure and (c) the 3D conformer in the ball-and-stick model, taken from [170].

1-iodo-2-methyl-butane is an organic component with the structural formula $CH_3CH_2CH(CH_3)CH_2I$, and molecular formula $C_5H_{11}I$. Three chemical representations are shown in Figure 5.1, the skeleton (a), Lewis structure (b), and a 3D ball (single atoms) and stick (chemical bonds) model (c). This molecule represents a prototypical chiral system and is, therefore, an attractive candidate in the scope of this work. As already mentioned before, FELs offer the possibility of element-selective inner-shell photoionization. To fully exploit this property of the light source, a suited choice, additionally, to the scientific interest, should be considered as well from a technical point of view. Hence, choosing a target molecule, which contains a large difference in the absorption cross section (σ_T) among their elements. Therefore, molecules, that have halogens attached to alkyl groups, such as iodine-containing molecules, i.e. iodomethane CH_3I [171–175], or bromoiodomethane CH_2BrI [176], were and are an appreciated target choice. Besides, they have inner-shell binding energies that can be conveniently reached with the photon energy range of FELs. Furthermore, 1-iodo-2-methyl-butane is a non-toxic, easily accessible and handleable molecule.

In the case of the here chosen molecular target $C_5H_{11}I$, the iodine atom has a slightly higher absorption cross section in comparison to the rest of the molecule, the hydrogen and carbon atoms. Iodine has a giant resonance at the

4d edge and was, therefore, in the past extensively studied. Within the scope of this work, which will be elaborated in the following sections in more detail, the neutral and singly charged iodine was addressed via the FEL pulses above the 4d edge using 63 eV and 75 eV, respectively. Neutral and singly charged iodine, I and I^+, have an absorption cross section of 3 Mbarn [177] and 13 Mbarn [177, 178], and 4d binding energies of approximately -59 eV and -70 eV, respectively.

The electronic configuration of the atomic iodine in the ground state can be described by:

$$1s^2 2s^2 2p^6 3s^2 3p^6 4s^2 3d^{10} 4p^6 5s^2 4d^{10} 5p^5 = [Kr] 5s^2 4d^{10} 5p^5$$

with the outer shell $5p^5$ equivalent to $5p^{-1}$, which means five electrons in the O-shell (principal quantum number n=5). The corresponding azimuthal quantum number l is 1, which follows from l = 0, 1, 2, 3 which corresponds to the s, p, d, and f, respectively. The total spin quantum number s is always $\frac{1}{2}$ for electrons. This leads to a total angular momentum of $j = \frac{3}{2}$ and $j = \frac{1}{2}$ ($j = l + s, j = l - s$).

In many-electron atomic systems, the total orbital angular momentum L is given by the Clebsch-Gordan series (CGS) $L = l_1 + l_2, l_1 + l_2 - 1..., |l_1 - l_2|$ [32]. For iodine, only one electron is in the outer shell, hence $L = 1$ applies. The values $L = 0, 1, 2, 3...$ are converted into upper-case Roman letters S, P, D, F..., respectively. The total spin angular momentum quantum number is calculated again via the CGS and is here $S = \frac{1}{2}$. Lastly, the total angular momentum, due to the spin-orbit interaction, delivers $J = L + S = \frac{3}{2}$ and $J = L - S = \frac{1}{2}$ ($J = L + S, L + S - 1, ..., |L - S|$). The term symbol, defined as ${}^{2S+1}L_J$, delivers the two possible doublet states ${}^2P_{3/2}$ and ${}^2P_{1/2}$. "The ${}^3Q_0$ state correlates asymptotically to the excited iodine fragment in ${}^2P_{1/2}$ configuration (I*)" [106], which can be reached by the usage of an optical pump laser, i.e. with 267 nm (4.6 eV) via a one-photon absorption or with 800 nm (1.6 eV) via a three-photon absorption. These two OLs were used to pump the molecule, hence triggering its excitation. "The ${}^1Q_1$ state corresponds to the iodine in its ${}^2P_{3/2}$ ground state" [106].

The potential energy curves along the C-I bond are presented in the following Figure 5.2. The ground state (GS, black) and the first two possible excited states in the A-band annotated via the Mulliken notation (${}^3Q_0$ in dark gray and ${}^1Q_1$ in light gray), were calculated by the theory (for details, see [106]). Under this scheme, the OL-pump pulse excites the molecule predominantly into the state ${}^3Q_0$ that evolves in time. A population transition into the ${}^1Q_1$ state (${}^2P_{3/2}$) at the conical intersection, was calculated to be at 2.4 Å, which corresponds approximately to 10 fs [106] and enables the production of ground-state iodine atoms (neutral dissociation channel). Depending on the time delay between the OL and the FEL-XUV probe pulses, the two different states can be addressed. For small time delays, the detection of iodine in the molecular environment before channel closing is more probable, and thus for

larger time delays, where the internuclear distance of the C-I bond increases, the iodine can be detected in its atomic environment showing due to the chemical shift, higher binding energies. This dissociation pathway and the evolution from the molecular into the atomic environment could be shown in the case of UV-pump XUV-probe experiments, which will be elaborated in detail in Section 5.6.1 and 5.7.

The same states can be reached as well via NIR pulses. This process requires absorption of at least three NIR photons, why the intensity of the NIR pulses was chosen about 3 orders of magnitude higher. However, as a consequence of the high NIR pulse energy, they furthermore allow for additional access to more Rydberg resonances via multiphoton absorption and thus a larger variety of dissociation channels (visualized via the three dots in Figure 5.2). The results of the NIR-pump XUV-probe experiments, presented in the following, revealed that the identified photoinduced dissociation dynamics originate most probably from Rydberg states. A detailed overview and explanation are given in Section 5.6.

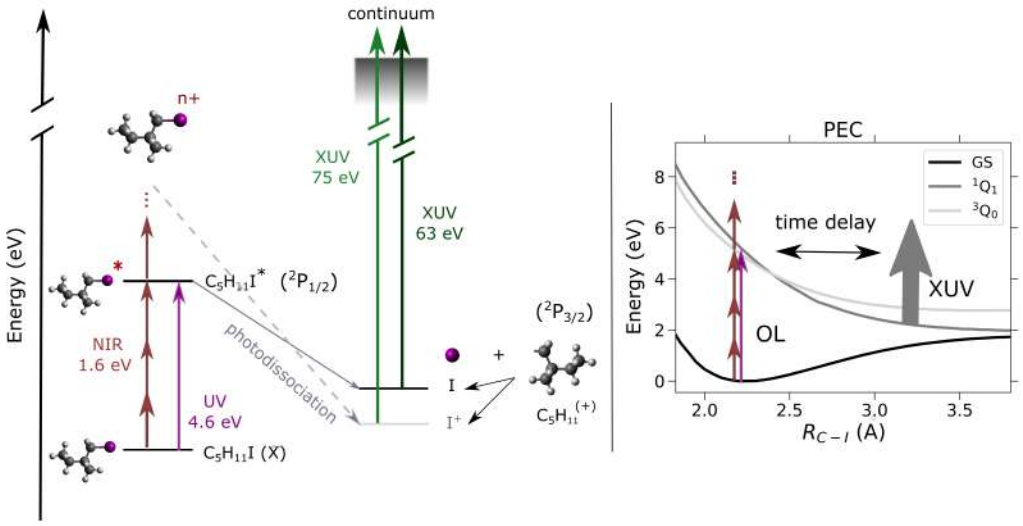

Figure 5.2: Left: Simplified schematic representation of the main contributing energy levels. The OL excites the molecule into the $^3Q_0$ state ($^2P_{1/2}$) and transits during the photodissociation of the C-I bond into $^1Q_1$ state ($^2P_{3/2}$), which is then probed via XUV-probe pulses. Right: Calculated potential energy curves for the ground and the possible excited A-band states of the molecule along the C-I bond. The UV pulses excite the molecule via a one-photon absorption into the triplet state $^3Q_0$ (purple arrow). The same excited state or higher-lying Rydberg states can be reached via three-photon or multi-photon absorption of NIR pulses, respectively (bordeaux arrows).

5.3 Experimental Setup

The experiment was conducted at the Free-Electron LASer in Hamburg (FLASH) [61, 62], which is a 315 m long operated FEL in the XUV and soft X-ray regime at DESY in Hamburg with two operated FEL lines FLASH1 and FLASH2 [94]. The double-sided VMI spectrometer of the CAMP endstation [179] at the BL1 beamline of FLASH1, was used to measure simultaneously cations and electrons produced by photodissociation- and subsequent ionization of the chiral iodoalkane molecule $C_5H_{11}I$ and its fragments, with a predominant scope on addressing the I $4d_{3/2}$ and I $4d_{5/2}$ vacancy states in different charge 56 environments, thus involving different ionization potentials. As sketched in Figure 5.3, a continuous supersonic molecular jet was injected into the interaction region (in blue), and hit by a 267 nm UV or 800 nm NIR pump laser (in red), and time-delayed XUV pulses of FLASH1 (in green).

The liquid molecular sample, which contained one of the two enantiomers R/S-1-iodo-2-methyl-butane, was stored in a cylinder and was heated up to 80 °C with a typical container temperature at more moderate temperatures around 45 °C. To avoid the condensation of the evaporated sample, it was seeded in helium carrier gas at 1 bar backing pressure and transported into a heated nozzle of the molecular jet (90°C). All temperatures were measured via PT1000 resistance temperature detectors. The continuous and supersonically expanded molecular jet was first downsized by the expansion through the nozzle with a diameter of 30 µm and was then passed through two skimmer regions with chamber pressures of 10^{-4} mbar and 10^{-6} mbar, and holding orifice diameters of 150 µm and 350 µm, in this sequence. Lastly, the molecular jet was narrowed by an aperture for differential pumping with an opening of 4 mm in the vertical and horizontal direction, placed approximately 35 cm away from the interaction volume.

In the interaction region of the main chamber, the center of the double-sided VMI spectrometer, with a vacuum of 10^{-9} mbar, the $C_5H_{11}I$ molecular jet was crossed with the UV or NIR pump laser pulses inducing as a possible path the molecule's photoexcitation mainly into the $^3Q_0$ state via single-photon absorption or three-photon absorption, respectively. This excitation resulted dominantly in the dissociation of the molecule's C-I bond and thus a neutral iodine and neutral mother fragment. Second, by applying high OL-pulse intensities, as it was the case with NIR pulses, most probably Rydberg resonances were reached as well. Both used optical laser pulses were generated using an 800 nm Ti:Sapphire laser [180] (Coherent Inc., Hidra-25), and linearly polarized along the x-axis, parallel to the molecular beam propagations. 800 nm are the fundamental wavelength of several commercially available laser systems. They are the standard available optical-laser sources at FEL facilities and, therefore, nowadays widely used in pump-probe experiments. These pulses can be delivered to the experiment, without any pulse conversation, resulting

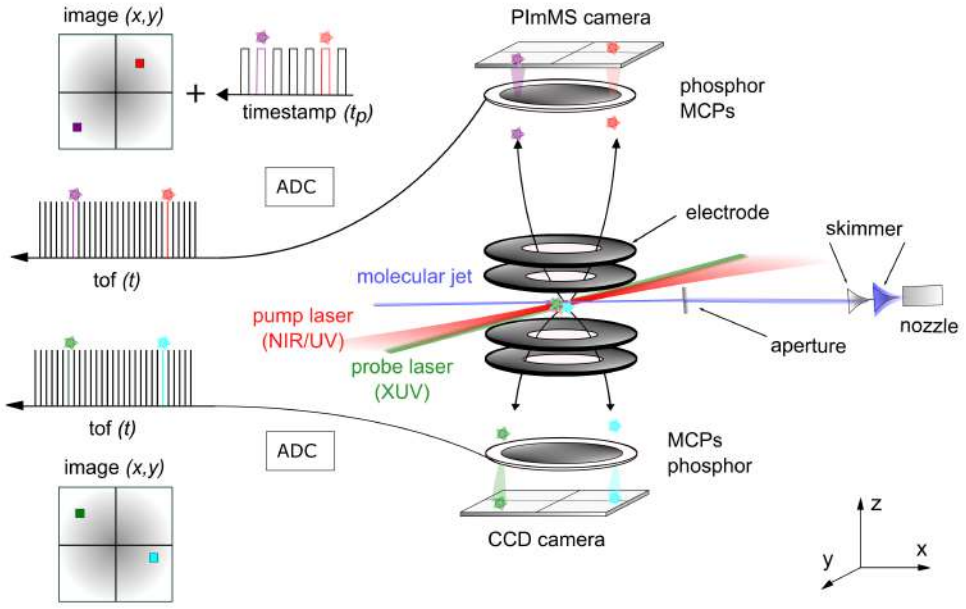

Figure 5.3: Sketch of the experimental setup: the molecules (blue beam path) were injected via a nozzle, and the molecular beam narrowed by passing through two skimmers and an aperture. In the interaction region, the molecules were hit by a UV or NIR pump laser, inducing the photodissociation of the molecules (red beam path). A time-delayed XUV probe laser (green beam path) resulted in inner-shell photoionization of the molecule. The created charged particles, cations and electrons, were imaged on position-sensitive detectors, and the particle position in pixel coordinates (x, y) was pictured via a PImMS or Allied Vision Pike F-145 CCD camera on the top and bottom side of a double-sided VMI spectrometer, respectively. ToF information was on both spectrometer sides extracted by the MCP's current readout (t). The PImMS camera delivered an additional timestamp (t_p).

in contrast to frequency-converted OL pulses in a better time resolution and shorter pulse lengths. Here, the 800 nm (1.6 eV) fundamental wavelength was driven at 10 Hz with a pulse duration of 70 fs FWHM. The NIR pulses, with a maximum energy of 1.8 mJ (100 % laser transmission), were focused to a spot size with a diameter in the order of 60 µm. The 267 nm (4.6 eV) pulses were created by third-harmonic generation using a BBO crystal (β-BaB_2O_4) [181], obtaining a maximum pulse energy of 176 µJ (100 % laser transmission), a focus diameter of about 100 µm, and a pulse duration of about 150 fs FWHM. The following intensity ranges were covered by the UV and NIR pulses used in this experiment; $(0.4-5.2)$ x 10^{12} W/cm^2 and $(1.3-4.1)$ x 10^{14} W/cm^2, respectively. The UV and NIR pulse durations were estimated during the beamtime using the BL1 autocorrelator. In contrast, the beam size diameters and pulse energies were not measured or fully documented during the beamtime and

therefore extracted via post-analysis. The approach and data are presented in the following section.

During the OL-induced dissociation along the C-I bond, the sample was photoionized at the 4d shell by time-delayed circularly polarized XUV probe pulses [103], produced by a mirror-based polarizer and entering almost collinear to the pump laser [85], i.e. at an angle of 1.5°. The pump and probe lasers are usually almost collinear to ensure that the spot of the probe laser is entirely within the spot of the pump laser [182]. The XUV polarization was chosen to be circular to provide additional information into the chiral response of the target and had a polarization degree of ∼80 % (for 63 eV) and ∼66 % (for 75 eV) [103]. The XUV pulses were generated by the FLASH1 FEL line with a repetition rate of 10 Hz (single bunch mode) as the maximum achievable synchronization rate between OL and FEL, under the given experimental conditions. To site specifically probe the different fragmentation channels, two different XUV photon energies were used. 63 eV (19.7 nm) addressing neutral iodine above the 4d edge ($E_{bind} \approx 59$ eV and $\sigma_T \approx 3$ Mbarn) and 75 eV (16.5 nm) for addressing additionally singly charged iodine above the energetically shifted 4d edge ($E_{bind} \approx 70$ eV and $\sigma_T \approx 13$ Mbarn). The XUV pulses were focused via nickel-coated KB mirrors into a spot with a diameter of about 10 µm. The pulse energies of the XUV pulses were chosen to be relatively low in order to minimize XUV-driven nonlinear effects on the sample and were 10 µJ (attenuated using a 420 nm Al filter) for the setting using 63 eV and 20 µJ for 75 eV. The pulse duration was about 80 fs FWHM for both settings.

The experiment aimed to characterize the target, and its dissociation dynamics, and to measure the time-resolved PECD under the given conditions for neutral and charged iodine fragments using electron and ion velocity map imaging as well as time-of-flight spectroscopy. The created ionic fragments and electrons were simultaneously extracted to the top and bottom along the spectrometer's z-axis by negative and positive static electric fields, respectively. Such experiments are insensitive to neutral fragments. Voltages on the plane electrodes of the double-sided VMI were chosen such that charged particles with the same initial velocity were focused along the z-axis into the same point on the detector (working principle already in detail presented in the previous Chapter 4). On both spectrometer sides, the particles hit 80 mm position-sensitive chevron-stacked MCPs, and electron avalanches were created, which were accelerated to P47 phosphor screens and the created light flashes lastly either detected by a Pixel Imaging Mass Spectrometry (PImMS) camera [183] on the ion side (324 × 324 pixels^2) or an Allied Vision Pike F-145 CCD camera on the electron side (1388 x 1038 pixels^2) delivering the particle's position coordinates (x, y). Due to the contribution of background electrons, produced by FEL stray light, the electron detector was gated with HV Behlke switches (model HTS 31-GSM), which defined a temporal window of operation for the MCPs. Ions and electrons were furthermore independently detected by the MCP's current read-out (ADC traces) via capacitive out-coupling, providing

high-resolution time-of-flight information (t) with a precision of a few hundred picoseconds. The PImMS camera delivered an additional timestamp (t_p) with a timing precision of a few tenses of nanoseconds. This camera system is so far only available through collaborations with the University of Oxford (UK). Different colors of the particles in Figure 5.3, i.e., violet and red, represent the different arrival times.

To pave the way toward the time-resolved PECD, data were recorded for 3 different target forms (racemic mixture and the two enantiomers), different time delays between OL and FEL pulses, and for left- and right circularly polarized FEL radiation.

5.4 Pre-Analysis

In this chapter, the pre-data analysis is presented, which was performed to check some FEL and optical laser parameters. This data was further used for normalization and calibration. Presented first, in Section 5.4.1, the correlation check between the measured signal yield and FEL pulse energies retrieved via the Gas Monitor Detectors (GMDs). The reason for this check is, that with higher FEL pulse energy, the signal yield in the ADC traces increases as well. These correlations ensured the appropriate assignment of GMD values to the ADC traces because the GMD data was later on used to normalize the signal yield on a single-shot basis. Second, in Section 5.4.2, the ADC traces, which are in principle the mass-over-channels yield of the detected cations, were calibrated to be represented in mass over channel. Third, as shortly mentioned before in the previous subsection, two relevant optical laser parameters, pulse energy and pulse shape, were retrieved as well in the post-analysis. The results are presented in the following Section 5.4.3 and 5.4.4, respectively.

5.4.1 GMD and ADC Trace Correlation

GMDs are photodetectors that are based on the photoionization of a gas at a low target density and non-invasively reveal information about the FEL's photon-pulse energy and photon-beam position. The FEL pulses pass a chamber filled with gas and ionize the gas. Produced ions and electrons are extracted via homogenous electric fields and detected simultaneously on opposite sides of the GMD. The fast photoelectron detection allows single pulse-to-pulse readout, i.e., pulse-resolved measurements. In contrast, the slower ions are read out by a slow averaging ion-current measurement, which is not affected by any time structure of the radiation. Thus, they provide information about the average FEL pulse energy. Such kind of diagnostic is required because the

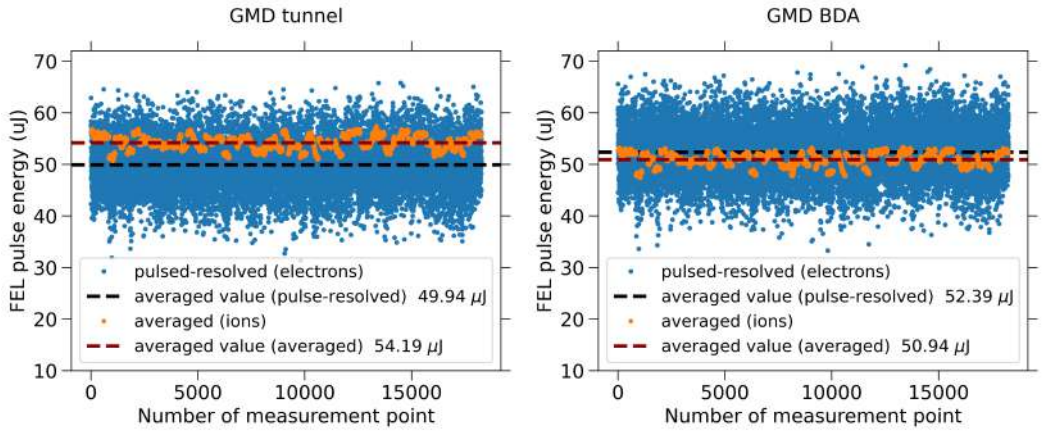

Figure 5.4: FEL pulse-energies extracted first from the photoelectrons (pulse-resolved, blue) and its mean value of it (black-dotted line) and second from ions (averaged, orange) and its mean value (red-dotted line) for one exemplary run. On the left for the GMD in the tunnel and on the right for the BDA GMD, placed more downstream, thus closer to the experiment.

FEL pulses are stochastically generated at SASE-FELs, meaning that they possess inherent statistical shot-to-shot intensity fluctuations. Experiments, performed at FELs, require therefore a pulse energy analysis on a shot-to-shot basis. Hence, GMDs are permanent parts of online photon diagnostics at practically all FEL facilities. The here-mentioned GMDs are conceived for the vacuum ultraviolet (VUV) and soft X-ray regime at FLASH, which are in use since the operation started in 2005 [80]. At hard X-ray FELs, for example at EuXFEL, upgraded GMDs, the X-ray gas monitors (XGMs) [81], are used, to compensate for the lower photoionization cross sections [184]. The XGMs are in comparison to GMDs principally "only" longer and deliver therewith a longer path for the creation of charged particles, which enables a higher number of detectable ions and electrons. XGMs are characterized to perform at FELs over a broad spectral range covering VUV, extreme ultraviolet (EUV), and soft and hard X-rays.

Figure 5.4 shows the FEL pulse energy data retrieved via GMDs for one complete measurement run. On the left side, the data extracted from the GMD in the tunnel is shown, which is placed at the end of the accelerator tunnel. On the right side, data from the GMD BDA, which is placed at the beginning of the experimental hall, thus after the tunnel GMD, is shown for the same run. This specific run contains more than 18000 measurement points (potted on the x-axis). Corresponding FEL pulse-energy values are plotted on the y-axis, in micro Joule. The single pulse-resolved FEL pulse energies are plotted in blue, and the mean value is visualized via a black-dotted line. The averaged pulse energy is shown in orange, with the marked mean value at the horizontal red-dotted line.

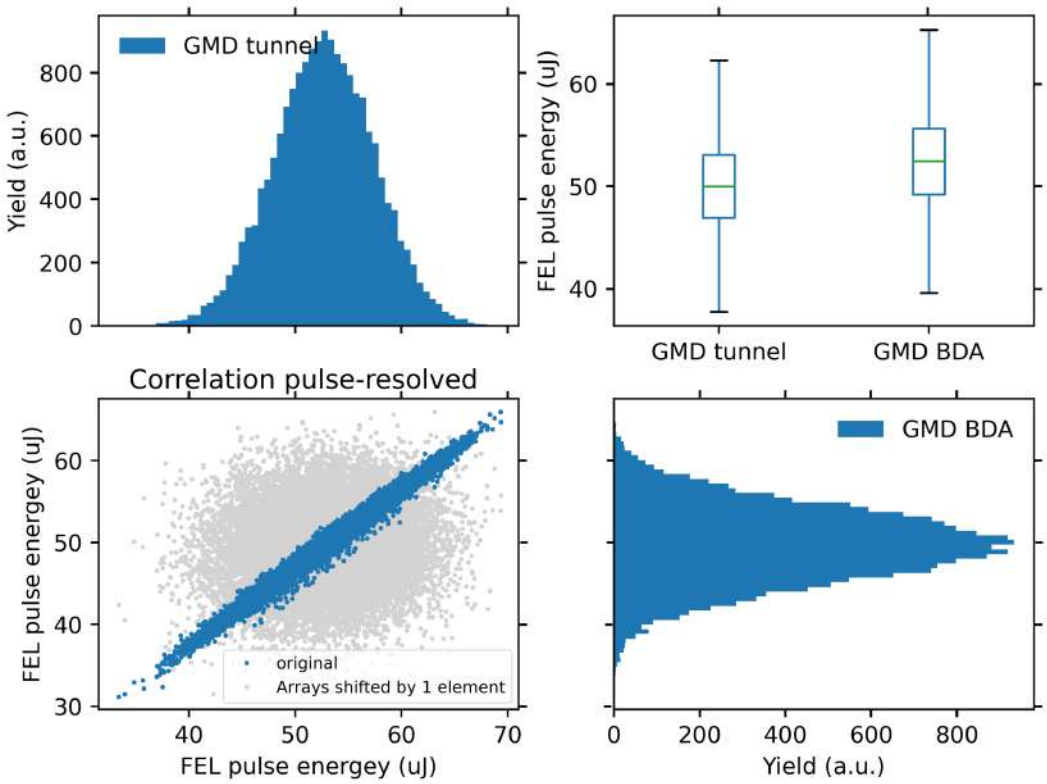

Figure 5.5: Correlation between the two GMDs (bottom-left corner). Corresponding histograms are shown next to it (top-left and bottom-right corner). The data in the upper-right corner shows the corresponding box plots.

As a first cross-check, the correlation between both GMDs was plotted. Visualized in Figure 5.5 is the scatter diagram with the correlation (bottom left), the corresponding histograms next to the correlation plot and in the top-right corner the box plots for the two GMDs are presented. The via the tunnel GMD (pulse-resolved) maximum and minimum values for the FEL pulse energy are 66 µJ and 31 µJ, respectively. The mean value is 50 µJ with a 1σ standard deviation of ± 4.6 µJ. The GMD BDA measured 69 µJ and 33 µJ as maximum and minimum values. The mean is 52 ± 4.7 µJ. The retrieved Pearson correlation coefficient is $r_{GG} = 0.99$ for the blue curve in the scatter diagram, meaning that there is an almost perfect positive correlation between both variables, as also expected. As a quick check, the two variables containing the GMD data were both shifted by one element against each other, which leads to the loss of the correlation (gray points). Thus, the FEL pulse energies are conjugated correctly. Hence, for all further correlation checks and the normalization, only the data from the GMD BDA was used, due to the fact to be closer to the experiment.

The extracted ADC traces, which were out-coupled from the MCPs at the ion side of the dVMI, are visualized for the same measurement in Figure 5.6. Figure (a) shows one exemplary ADC trace and a corresponding zoom,

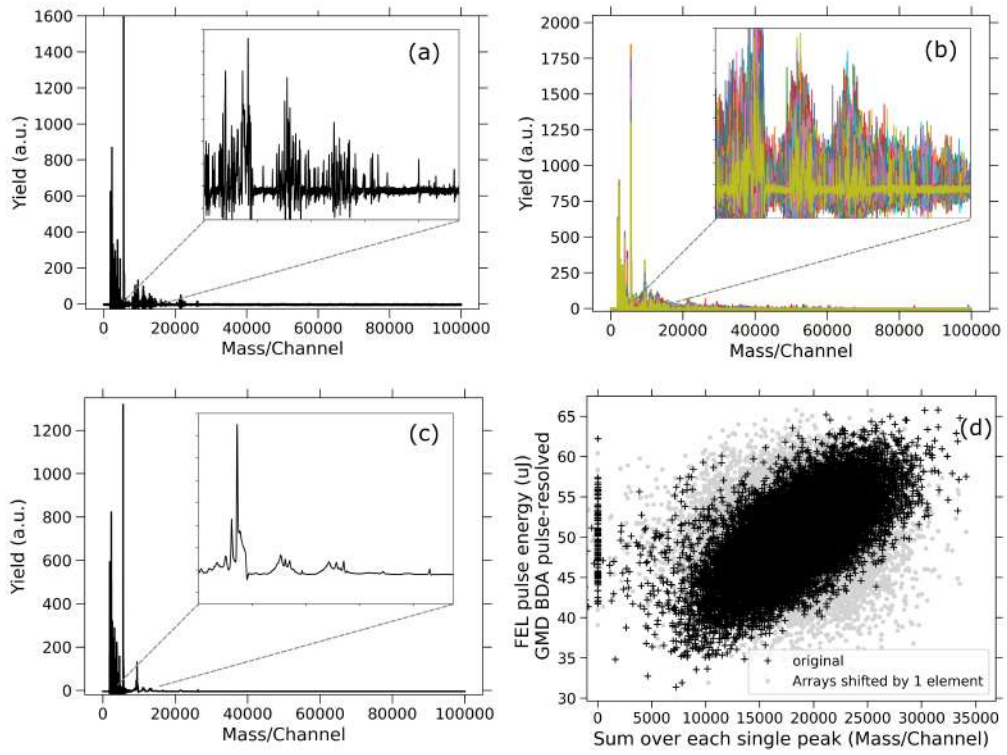

Figure 5.6: (a) One single ADC trace, (b) all single ADC traces of one run, (c) averaged ADC trace, and (d) the correlation between the pulse-resolved FEL pulse energy (retrieved from the GMD BDA) and the sum over each single peak of the averaged mass spectrum shown in (c).

into the region between 8000 and 16000. In (b) all single ADC traces (in total, 18078) are plotted and the averaged ADC trace is shown in figure (c). The zooms in (b) and (c) are in the same region as for (a). On the x-axes of figures (a-c), the cation mass is imprinted into the channels of the ADC traces. The calibration from mass over channel into mass over charge is presented later. To perform the correlation check between the FEL pulse energy (GMD BDA pulse-resolved shown at the right of Figure 5.4) and signal yield (sum over all single peaks of the averaged spectrum presented in Figure 5.6(c)), the correlation of both was plotted in a scatter diagram and visualized in figure (d). The calculated Pearson parameter is r=0.3, thus a moderate positive relationship was retrieved. Performing programmatically again the variable shift, it can be noticed that the correlation gets less (gray points). It can be therefore assumed that the measured ADC traces correspond to the initially conjugated FEL pulse energies.

The here-presented correlation checks are essential for further normalization of the signal yield against the corresponding FEL pulse energy and ensure a correct quantitative comparison among the data later. This normal-

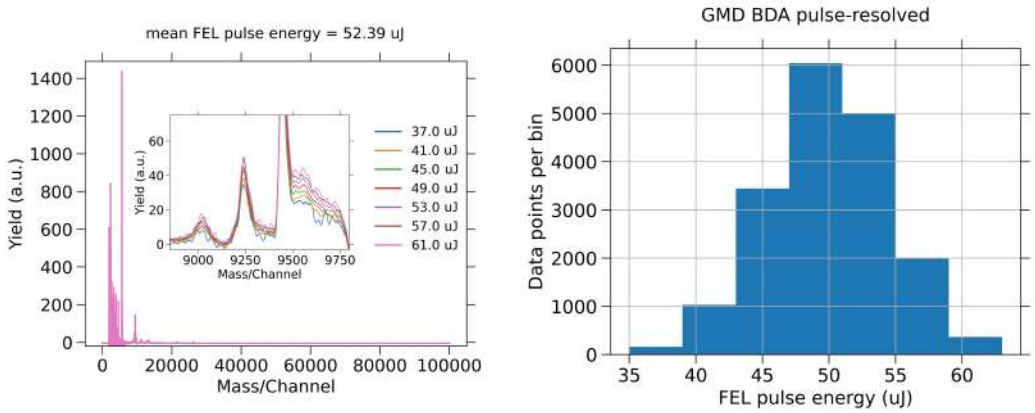

Figure 5.7: FEL-pulse energy-dependent signal yield. The signal yield is plotted for seven energy bins (each with a width of 4 µJ), which cover the range from 35 µJ to 63 µJ.

ization is important because the fluctuating FEL pulse energy increases or decreases a variety of signal yields, as exemplary shown in Figure 5.7. As already mentioned, the mean FEL pulse energy was for this specific run 52 µJ (BDA GMD pulse-resolved). The signal yield shows a clear difference for the seven energy bins ranging from 35 µJ to 63 µJ, within this measurement, minimum and maximum measured FEL pulse energy, respectively. Each bin was chosen to have a 4 µJ width (see left histogram in Figure 5.7). The lowest signal yield corresponds to the lowest FEL pulse energy range, with the mean value of 37 µJ (blue curve). The highest FEL pulse energy, with a mean of 61 µJ, yields the highest signal (magenta curve). As shown in Figure 5.4, the FEL pulse energy fluctuates a lot from shot to shot (blue points). Therefore, this pre-data analysis was used in the following to normalize each signal yield against the measured FEL pulse energy by using the pulse-resolved FEL pulse energy retrieved by the electron signal measured via the GMD BDA.

5.4.2 ADC Trace Calibration

The measured averaged spectrum, i.e., Figure 5.6(c), which data was retrieved out of the ADC traces, can be calibrated from mass over channels into mass over charge by educated guessing. Usually, the peak with the shortest time of flight stems from protons (H^+ with 1 m/z) and the peak with the longest time of flight from the intact and singly charged molecule, here the parent ion ($C_5H_{11}I^+$ with 198 m/z). Furthermore, the I^+ with 127 m/z could be identified as well, due to no other peaks in the surrounding. The identification of I^+, clarified as well the mass over charge of the two previous peaks at 63.5 m/z and 71 m/z, which are I^{2+} and the mother ion $C_5H_{11}^+$, respectively. All other peaks could be identified via the retrieved calibration presented in Figure 5.8(a).

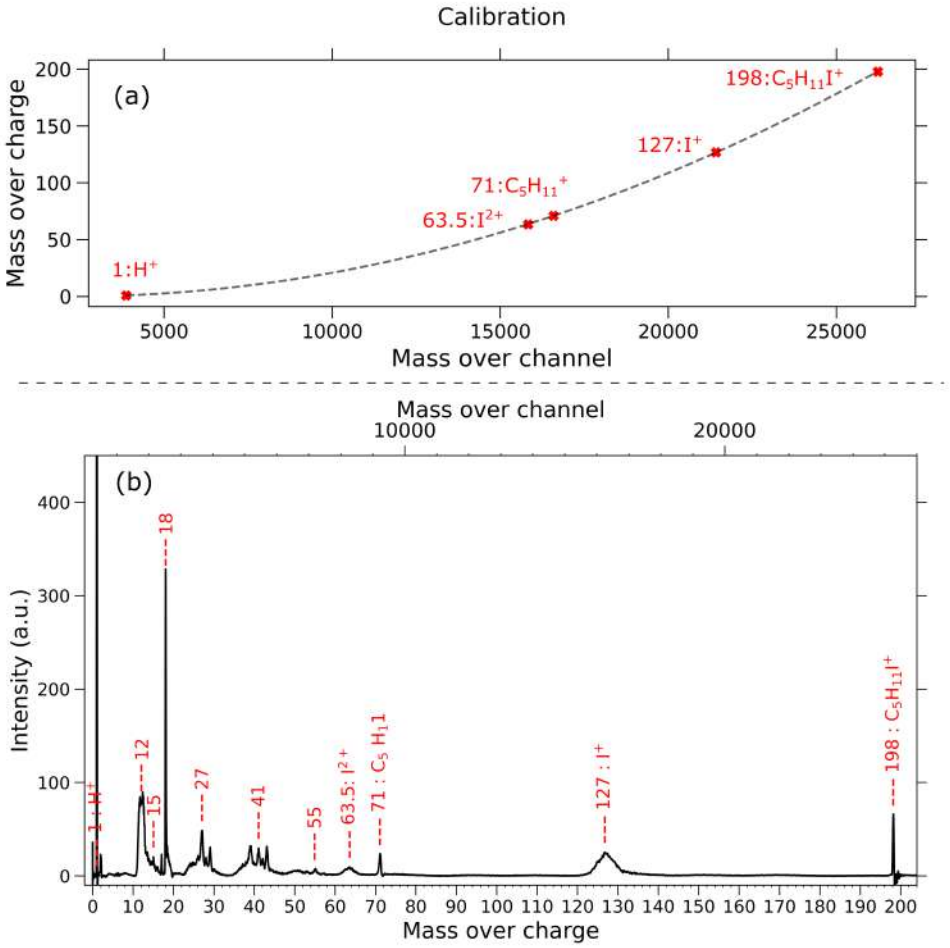

Figure 5.8: (a) ADC trace calibration from mass over channel to mass over charge. The ions in red were annotated by educated guessing. (b) shows the calibrated spectrum of the spectrum presented in Figure 5.6(c), represented on the x-axis in mass over charge (bottom) and mass over channel (top).

Such calibration was performed for all the following presented spectra, and a simplified (not fully annotated) example is shown in Figure 5.8(b).

One alternative and common approach, if the educated guessing is not realizable, is to calibrate the spectrometer and the ADC traces by the usage of noble gases, as their masses and ionization energies have well-established values.

5.4.3 UV and NIR Pulse Energy and Intensity Estimation

During the beamtime, transmission scans of the optical lasers were performed. Within the transmission control, the values were changed by entering the relative laser transmission in percentage, which induced a mechanical change of the angle of the polarizer. The corresponding pulse energies of the UV and NIR pulses are plotted within Figure 5.9 and were retrieved as follows. For the UV pulses (left figure), only one single pulse energy measurement delivering 7 µJ at 10 % relative laser transmission was documented (see gray diamond, annotated as "data point Ilchen 2018 UV"). The other pulse energies were deduced from another measurement series, which was conducted by Erk et al. some months later in 2019. This Erk data [185], visualized with red crosses, was plotted and fitted. The red-dashed fit was then shifted by approximately 5 µJ to cross the single gray data point at 10 %. The shifted fit (black-dotted line) represents the estimation of the UV pulse energies for the in the following presented FLASH beamtime results. The shifted values are lower in comparison to the measured pulse energies in red. The reason, therefore, is most probably the changes within the optical laser setup, which were for example a cleaned grating and newly installed mirrors.

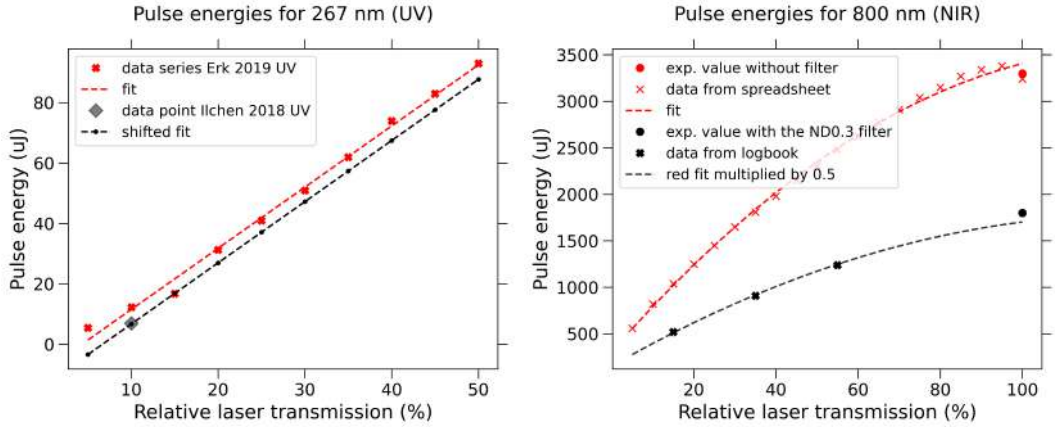

Figure 5.9: Pulse energies for the optical lasers: left for the UV covering 5 % to 50 % relative laser transmission and right for the NIR covering 5 % to 100 % without (red curve) and with a filter (black curve).

For the NIR pulses (right figure), the pulse energies were measured only twice, once without a filter (red point, 3.3 µJ) and once with an ND0.3 filter, which reduced the transmission by approximately a factor of 2 (black point, 1.8 µJ). Both measurement points were retrieved at 100 % relative laser transmission. Additionally, during the beamtime, various pulse energies were documented, but it was not clear to which configuration they belonged. Furthermore, some values for the pulse energies, with the inserted filter, were not

documented and were missing. Therefore, all measured (black and red points) and the documented values (red and black crosses) were plotted and fitted (red and black dashed lines) within one figure, which clarified to which configuration the documented pulse energies belonged. In addition, the interpolation for the pulse energies with the inserted filter, in the range between 55 % and 100 %, delivered the missing pulse energies (black-dashed line). The nonlinearity of the data is not related to any physical effect, but most probably to a wrong conversion of the via the beamline software entered relative laser transmission in percentage and the change in angle of the polarizer in the laser hutch [186].

All presented fits were performed by using the, for scientific purposes foreseen, python library "SciPy". The therein-contained "optimize" module provides several commonly used optimization algorithms, for example, the here-used method "curve fit". This method applies non-linear least squares to fit the data to a function, thus minimizing the sum of the squared residuals, which is the difference between the measured (red and black data points) and predicted value (values on the red or black dashed lines).

For the performed experiments, which are presented in the following, the pulse energies (E_p) of the black-dashed fits are applicable, which range for the UV pulses from 7 µJ to 97.7 µJ and for the NIR pulses from 0.45 mJ to 1.25 mJ (in both cases 10 % - 55 % relative laser transmission). Taking additional parameters of the optical laser into account, i.e., pulse duration t and the spot size of the beam s, the intensity can be calculated. Such a calculation was performed for the UV and NIR pulses. Within the intensity calculation, the Gaussian beam model was used. Equation (5.1) was used to calculate I_0, the intensity at the center of the beam at its waist.

$$I_0 = \frac{2 \cdot E_p}{t \cdot s} \tag{5.1}$$

The beam size was retrieved out of the beam waist at the center using the Equation (5.2). w_0 was calculated using the horizontal/vertical FWHM of the Gaussian beam using Equation (5.3).

$$s = \pi \cdot w_{0(h)} \cdot w_{0(v)} \tag{5.2}$$

$$w_0 = \frac{FWHM}{\sqrt{2 \cdot log(2)}} \tag{5.3}$$

Using the values for the UV pulse duration of 150 fs and the 100 µm FWHM of the beam, the covered intensity range is $(0.4 - 5.2)$ x 10^{12} W/cm^2. The intensity of the NIR pulses is in the range of $(1.3 - 4.1)$ x 10^{14} W/cm^2, thus three orders of magnitude higher due to the higher pulse energy, shorter pulse duration of 70 fs FWHM and the smaller beam size of 60 µm FWHM.

5.4.4 UV and NIR Beam Projections

In the following two Figures 5.10 and 5.11, the X and Y projection of UV and NIR pulses is shown, captured by a camera close to the focus position. The camera had a chip size of 601 x 401 pixels^2 (hxv). In Figure 5.10, all single UV pulse projections are plotted, left for the horizontal direction X and right for the vertical direction Y. All 360 projections of one measurement run are plotted over each other. Looking at the figures, it can be seen, that within a single run, only small shifts of the beam appeared. Meaning that all peaks of all single projections overlap in position with a maximal identified shift of 6 pix, which corresponds to 20.70 µm in the X and Y projection (1 pixel is 3.45 µm). Both projections deviate from a perfect Gaussian profile. The projections contain contributions from 4 or 5 single Gaussian peaks (blue, red, gray, magenta, and cyan-dotted lines). An exponential component can be identified as well (plotted via the orange-dotted line). The black-dotted line represents the multi-Gaussian fit, which includes each single Gaussian and in addition the exponential component. The spiky substructure of the UV pulses results from different contributions, which will be elaborated in the following [186], first for the horizontal projection X: The red Gaussian component 2 originates from the UV beam reflected at the front side of the screen. The blue Gaussian component 1 is the reflection of the beam at the back side of the illuminated screen, which is as well captured by the camera and is furthermore less intense in comparison to the beam component fitted in red. Gaussian components 3, 4 and 5 (gray, magenta and cyan, respectively) originate most probably from NIR beam components, which are detected due to the sensitivity of the screen and most probably residuals from the frequency conversion from 800 nm into 267 nm. As an estimation for the horizontal UV beam size, the FWHM of the red Gaussian component (no. 2) can be taken. The FWHM is 19.01 pixels, which corresponds to 65 µm. In the vertical projection the beam and the reflection are not any more resolved as two separated peaks but represented by one, the Gaussian component 4 in red. This is due to the smaller distance between the two reflections, visualized in Figure 5.12(a). The red peak delivers therefore also a larger FWHM in the vertical beam direction of 28.62 pixels, thus 96.60 µm, due to the peak overlap of the two beam reflections.

Figure 5.11 represents the NIR pulse projections (347 single projections), left for the horizontal direction X with an FWHM of 100 µm (29 pixels, red fit of Gaussian component 2) and on the right side for the vertical direction Y with an FWHM of 195.5 µm (56.67 pixels). The projections look less spiky in comparison to the UV pulse projections, most probably due to the not required and not performed frequency conversion. The horizontal projection (left) contains two Gaussian components originating again from the OL and its front and back reflection on the screen. In the vertical direction (right) one peak can be identified, which is again most probably the overlap of the beam

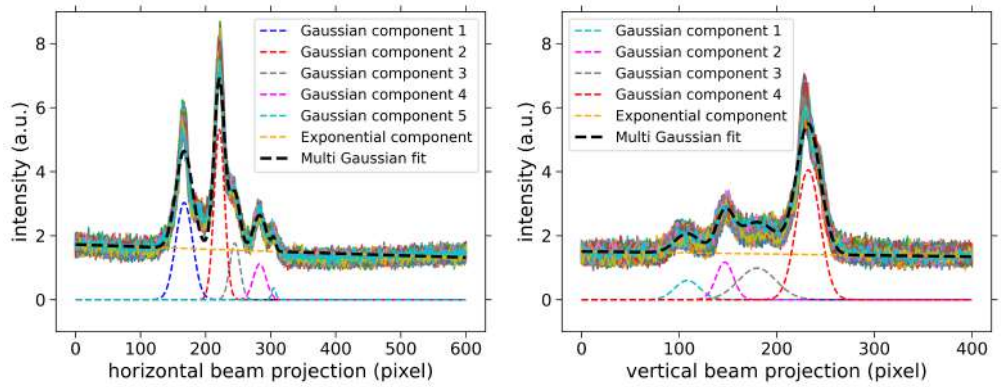

Figure 5.10: X and Y projection of all single UV pulses, in total 360. The black-dotted line represents the multi-component fit, including the 4 (5) Gaussian components ((blue), red, gray, magenta, and cyan) and an exponential in orange. The multi-Gaussian fit is shown via the black-dotted line. Red Gaussian components were used to estimate the focus size of the beam.

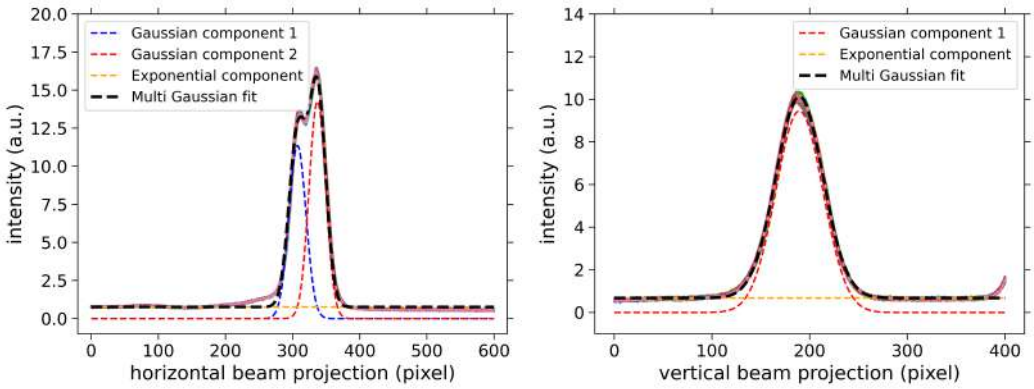

Figure 5.11: X and Y projection of single NIR pulses, in total 347. The horizontal projection (X) shows the contributions of two Gaussian components (dashed lines in blue and red). The vertical projection (Y) shows one identified Gaussian component in red. An exponential component is visualized in orange, and the multi-component fit via a black-dotted line. The red Gaussian components were used to estimate the focus size of the beam.

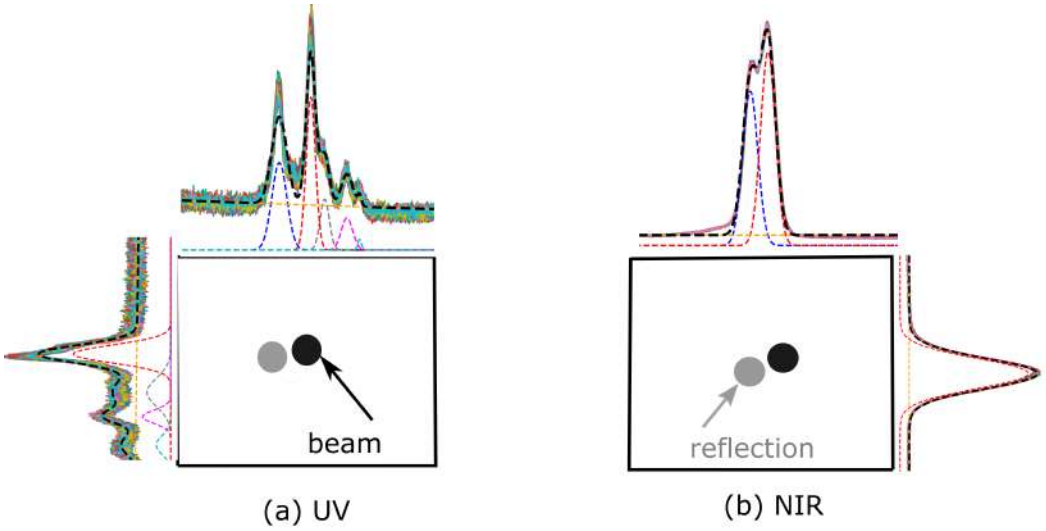

Figure 5.12: Simplified visualization of the origin of the blue and red Gaussian components in the beam projections resulting from the OL (black dot) and its reflection (gray dot) on the screen (all dimensions are not to scale).

and the reflection and shows therefore larger, almost doubled, FWHM.

The analysis of the here presented projections is useful to get an impression of the beam shape. Nonetheless, the values do not correspond directly to the beam size identified or documented during the beamtime. 100 µm^2 for the UV pulses were measured and in comparison, the above-presented analysis is a hint for the potentially smaller UV beams size and delivered 65 µm x 97 µm (hxv). In contrast, the NIR pulses were measured to be in the order of 60 µm^2, but the analysis here is an indication for a larger focus beam size of 100 µm x 196 µm (hxv). Whereas, for both OL wavelengths the horizontally extracted foci can be weighted more, due to the missing overlap of the OL with its reflection, which is apparent in the vertical projections Y.

Lastly, as a side note, even though many corrections regarding the optical or FEL components were performed automatically during the experiment, for example, the delay time fluctuations between the pump and probe pulses, known as timing jitter, the drift correlations of the optical laser were in contrast corrected manually. This means that the beam was imaged via the camera on the screen, which was graphically visualized as well in Figure 5.12, and a circle was drawn around the region of interest (ROI), i.e., the black dots representing the OL beam. The optical laser drifted by a few tenses of pixels over some hours and was then corrected and placed again into the predefined ROI by moving the mirror in the laser hutch via the available beamline software.

5.4.5 Non-linear Least Squares Regression

The FLASH beamtime data is an exploratory study, no equal experiment was performed before. Mathematical model functions were used to fit the experimental data, for example, fitting a Gaussian function to one of the mass spectra peaks. The conducted data analysis was performed within jupyter notebooks using the programming language Python 3. Python offers different fitting packages, which contain different curve fitting models. Mostly known and used are the "scipy.optimize.curve_fit" and "lmfit" module. Both modules are powerful. They are working with the non-linear least squares fitting method. For this, work the lmfit module was used. It offers a high-level interface to non-linear optimization and curve fitting problems. It includes already many optimization modules from the scipy.optimize module but contains as well many enhancements, for example, parameter and report classes. Hence, parameter bounds, for example, the amplitude that represents the overall intensity (or area of) a peak or function, the center parameter (variable of interest) will be the centroid x value and a sigma parameter that gives a characteristic width of the peak [187]. The report class displays a lot of statistical data of the fit, including information about the model, fit statistics, variables, and correlations.
Specifically, for the FLASH data the built-in and pre-defined fitting model, the GaussianModel described by Equation (5.4) from the lmfit modules, was used:

$$f(x; A, \mu, \sigma) = A \cdot \frac{1}{\sigma\sqrt{2\pi}} e^{-\frac{1}{2}(\frac{x-\mu}{\sigma})^2} \tag{5.4}$$

with the independent variable x, and the parameters: amplitude A, mean μ, and the standard deviation σ. The FWHM can be retrieved via $2\sigma\sqrt{2 \cdot ln2} \approx 2.3548\sigma$

5.5 Time-independent Results

In this section, the simultaneously recorded electron and ion data is presented separately. In experiments employing photo-induced fragmentation or ionization, which is here the case, the information about the interaction process lies in the energy and angular distribution of the emitted photoelectrons and ions. Intensities in the recorded time-of-flight mass spectra reveal information about ion or electron yield, and ion or electron momenta can be extracted from the ion or electron velocity map images. The extraction of these observables is in the following presented. The data within this chapter was not analyzed regarding time dependencies.

5.5.1 Electron Data

For the electrons, the VMI images were analyzed and are here presented in detail, including the image-processing tools, for the retrieval of photoelectron spectra and angular distributions from the recorded VMI images by applying Abel inversion algorithms.

Image Processing and Abel Inversion

Recorded VMI electron images via a dVMI were already introduced in the previous Section 4.3.2 and an exemplary data handling was shortly presented as well. Here, the analysis of the electron data recorded during the FLASH beamtime on the chiral molecule 1-iodo-2-methyl-butane is presented. This data was extracted from the two different pump-probe schemes: UV-pump XUV-probe (see Figure 5.13) and NIR-pump XUV-probe (see Figure 5.14), but within this chapter, no time-dependent features are analyzed. The photoelectrons were detected on the bottom side of the dVMI spectrometer and recorded via an Allied Vision Pike F-145 CCD camera with a sensor size of 1388×1038 pixels^2. The images were preprocessed and stored with a size of 960 x 1288 pixels^2, to save data storage. The presented images of these two figures, show averaged data of minimum 150000 images, which corresponds to a recording time of more than 4 hours. These long times originate from the low repetition rate of 10 Hz as the limit for the achievable synchronization of the OL and the XUV pulses under the given conditions for the presented experiment.

For the averaging and data analysis, recorded images from the same enantiomer, same helicity, and same pump-probe delay (OL preceded the XUV pulses by -500 fs) were used and presented. The two images, including all de-

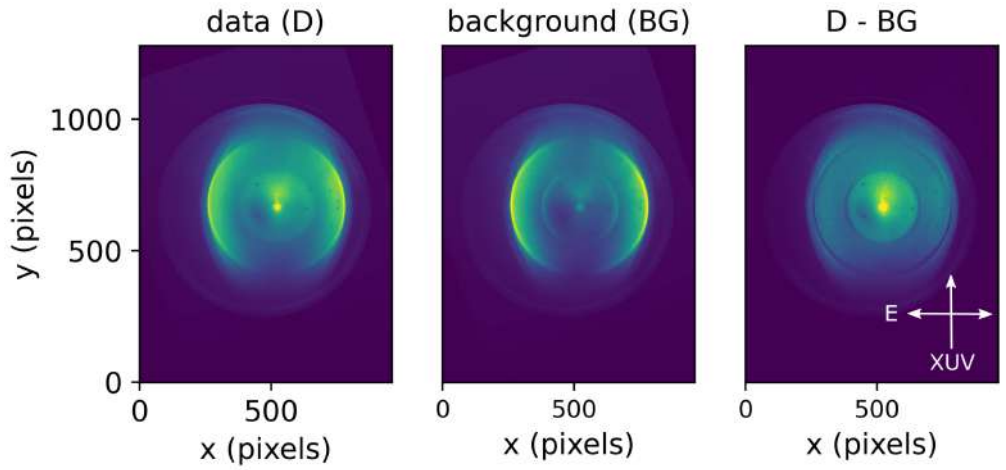

Figure 5.13: Electron VMI images obtained from the UV-pump 63 eV-XUV-probe scheme. Averaged data including the molecule, the carrier gas helium (left, defined as data D). The background (middle, abbreviated with BG) and the background-subtracted data, which was in the following analyzed (right, D-BG).

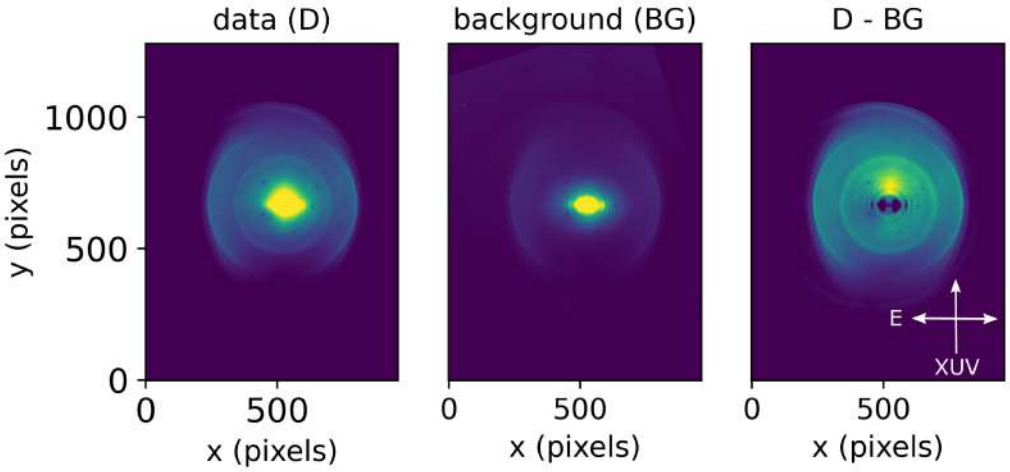

Figure 5.14: Electron VMI images obtained from the NIR-pump 75 eV-XUV-probe scheme. Averaged data including the molecule, the carrier gas helium (left, defined as data D). The background (middle, abbreviated with BG) and the background-subtracted data (right, D-BG).

tected photoelectrons during the measurement (mainly from the ionized helium and iodine), are shown in the left images of Figure 5.13 and 5.14, annotated as data (D). For the data analysis, these images were background subtracted to minimize as much as possible contributions from the disturbing background as a first image processing step for the later-performed Abel transform. Thus, the averaged image of the background (BG) was subtracted to minimize the signal from irrelevant photoelectrons showing a strong contribution or which are apparent in the proximity of the ejected electrons of interest, thus close to the photoelectrons originating from the iodine 4d shell. The background was chosen differently for both cases presented in Figure 5.13 and 5.14 due to the differently used XUV pulse energy and the different contributions from the OL and will be detailed in the following.

For the UV-pump XUV-probe experiments, shown in Figure 5.13, XUV pulses with a photon energy of 63 eV were used. This XUV photon energy addressed the 4d iodine subshell, as already in detail explained in the experimental setup Section 5.3, but also the 1s helium carrier gas electrons, which led in addition to singly (E_{bin}=24.6 eV [21]) and doubly (E_{bin}=54.5 eV) charged helium. The corresponding photoelectrons from the helium ions are also clearly recognizable in the data image (D) and are the most dominant photoelectron contribution. The outermost ring corresponds to photoelectrons from the singly charged helium, and the photoelectrons from the doubly charged helium are only a few pixels ($\sim$ 10 pixels) away from the signal of interest. Therefore, recorded background images including data from measurements only with helium were recorded, meaning that the molecule was not injected into the experimental chamber (realized by closing the corresponding Swagelock valve on the periphery of the molecular jet). These two rings from the helium background are visualized in the middle image of Figure 5.13. In addition, contributions from the UV pulses solely, which contributed much less to the background, were also added and led to the circle in the middle of the background image (BG). This combined background was subtracted from the data image, resulting in the background-subtracted image (D-BG), which was then further processed and analyzed. Before the subtraction, images (D) and (BG) were normalized against the intensity of their outermost and strongest signal originating from the He^+ photoelectrons.

In contrast, 75 eV XUV photons were used for the NIR-pump XUV-probe experiment (shown in Figure 5.14), which led to higher kinetic energies of the ejected photoelectrons and thus the radius-increment of the photoelectron rings (movement to the outer part of the detector). In addition, the photoelectrons from doubly charged helium were not present. Furthermore, the photoelectrons from the singly charged helium were a minor background contribution and therefore not treated as the most disturbing background. The main background contributions originated from the NIR-pump pulses solely, which created the bright spot in the middle and the surrounding rings. The averaged background (BG), shown in the middle image of Figure 5.14, was nor-

malized to the spot in the center and subtracted from the data image (D). The background-subtracted image (D-BG) is shown on the right and was further analyzed.

All above-presented VMI images were already corrected regarding their rotation. The next step was centering the two background-subtracted images (D-BG) by calculating the centroid of the image. Therefore, the "ndimage" module of the "SciPy" library in Python was used. In addition, the images were cut into an image size of 600 x 600 pixels^2 for easier data processing. An additional common VMI image processing step is the symmetrization of the image, which increases the signal-to-noise ratio, but this step should not be performed in the light of PECD studies. The reason is, that the data that potentially contains the asymmetry in the photoelectron angular distribution would get lost. In an additional and last image-processing step, the center of both images, showing a bright signal contribution in the center of the images, was masked.

The Abel inversion was performed using again the PyAbel library and its method rbasex. To check the result of the Abel inversion and for better visualization, half of the non-inverted VMI image and half of the abel-inverted image were stuck together, presented in Figure 5.15(a) for the UV pulses and in Figure 5.15(b) for the NIR pulses. For the inversion, the complete image was used. Nonetheless, it should be mentioned on this point, that the approach to analyze the four quadrants of the image separately was performed as well, delivering identical results. It can be seen in the presented VMI images that the instrumental resolution was high enough to resolve the few-eV spin-orbit splitting of the I 4d photoline. The rings of interest, are marked with two yellow arrows. Nonetheless, the statistics could be even better. Furthermore, the background subtraction is as well visible. These areas are the darkest ones and are represented by the minimum value, 0.

Radial Distribution and Photoelectron Spectra

The Abel inversion takes the 2D projection of the angle-resolved photoelectrons of the VMI image and reconstructs a slice of the cylindrical symmetric 3D distribution. The corresponding radial distributions of Figure 5.15, which is the horizontal projection (along the camera axis x) of the 2D slice at the position y=0, are plotted in Figure 5.16(a) and (i). Presented are, on the top, the data for the UV-pump XUV-probe (a-c) and on the bottom for the NIR-pump XUV-probe experiments (i-iii). The peaks in the radial distribution represent the detected photoelectrons. Corresponding kinetic or binding energies can be extracted after applying a calibration, similar to the presented one in Figure 4.5(c) in Section 4.3.1. Therefore, the known binding energies of the existing and already identified photoelectrons from the He^+ and He^{2+}

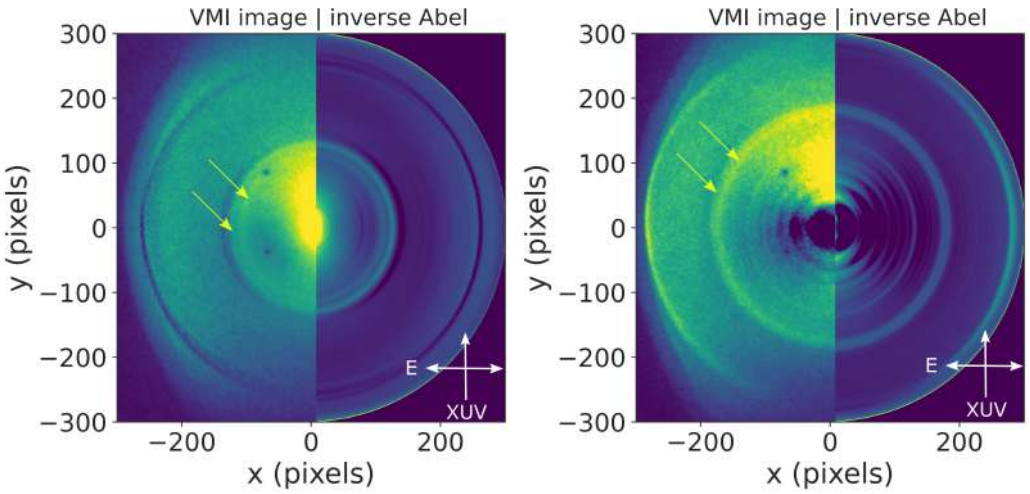

(a) UV pump **(b)** NIR pump

Figure 5.15: Background subtracted VMI images (left half) and the Abel inverted image (right half) plotted in (a) combining the XUV-probe pulses with the UV-pump and in (b) with NIR pulses.

ions were used. Their radial position is plotted against their binding energies of 24.6 eV and 54.5 eV, respectively (black data points in the middle Figure 5.16(b)). It is also possible to plot the kinetic energies, by using the equation $E_{kin} = E_{XUV} - E_{bin}$, which was calculated as well and presented via blue dots. For the calibration of Figure 5.16(ii) the calibration point of the missing He^{2+} was replaced by the data points of the two spin-orbit I 4d states, which binding energies were retrieved out of Figure 5.16(b). Generally, the square root of the ring radius (peak position in the radial distribution) is proportional to the kinetic energy of detected particles. Hence, the relationship between the radius and the charged particle's corresponding kinetic energy or binding energy can be described as a linear function, which was fitted to the data points and is represented by the blue-dashed and black-dashed lines, respectively. The fit was extrapolated, and the binding energy data were used to convert the radial distribution into spectra plotting the corresponding binding energy in eV, which are shown in Figure 5.16(c) and (iii) and represent the photoelectron spectra. The extracted calibration functions, which are given by the fits, are represented in Equations (5.5) - (5.8). As an alternative approach, especially if no known photoelectrons can be identified, the radii-conversion into kinetic energies or binding energies can be carried out via ion trajectory simulations using the SIMION software package, from which an empirical formula can be constructed that connects the radial position on the detector with the kinetic energy of the electron. This approach, which was here not necessary and therefore not performed, was presented in Section 4.3.1 and visualized in Figure 4.5(b) for ions and 4.5(c) for electrons, and would generally require much more work because the model of the spectrometer and many additional

parameters need to be defined in SIMION.

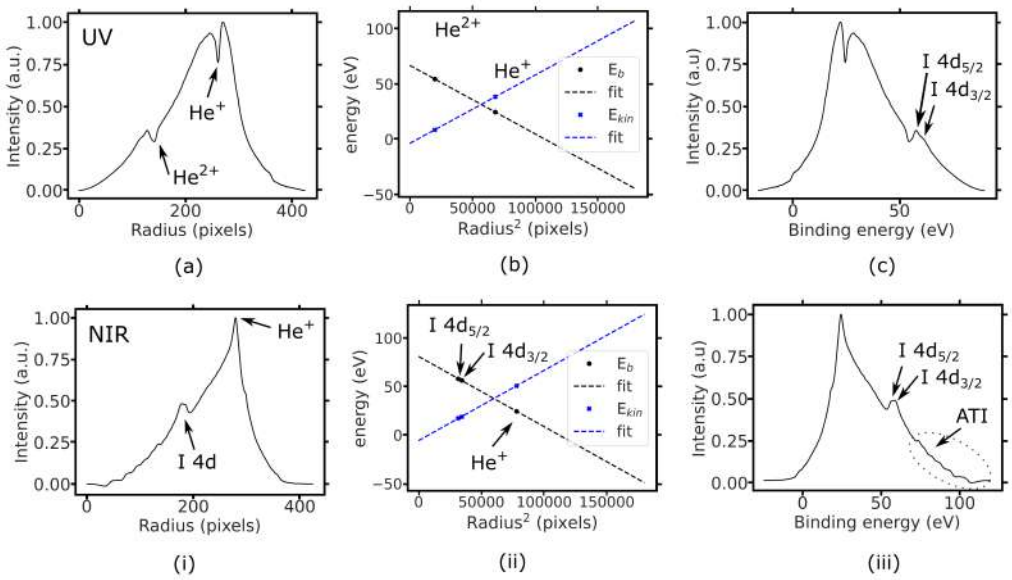

Figure 5.16: Radial distribution in pixels (right, a and i) extracted from Figure 5.15, linear fits (dashed lines) for the determination of the calibration factor k (middle, b and ii), and the corresponding photoelectron spectrum showing the binding energies in eV of the detected particles on the x-axis (left, c and iii). At the top for the UV-pump and XUV-probe (a-c) and bottom for NIR-pump XUV-probe experiments (i-iii), at -500 fs time delay for both schemes.

$$E_{kin(63eV)} = 6.19 \times 10^{-4} \cdot R^2 - 3.78 \tag{5.5}$$

$$E_{bin(63eV)} = -6.19 \times 10^{-4} \cdot R^2 + 67.60 \tag{5.6}$$

$$E_{kin(75eV)} = 7.23 \times 10^{-4} \cdot R^2 - 5.68 \tag{5.7}$$

$$E_{bin(75eV)} = -7.23 \times 10^{-4} \cdot R^2 + 81.60 \tag{5.8}$$

The two I 4d photolines, annotated in Figure 5.16(c) and (iii), delivered binding energies for the molecular iodine of 56.25 eV for the I $4d_{5/2}$ state and 57.78 eV for the I $4d_{3/2}$ (spin-orbit split of 1.53 eV), which is consistent with the published result in [106]. The data within this cited work analyzed the UV-pump-related data from the same FLASH beamtime. The main results will also be shortly presented in the following Section 5.7. Figure 5.16(iii) contains, in addition, several smaller contributions visible in the pixel region between 0 and 140. These photoelectrons originate from above-threshold ionization by the NIR pulses, which are present due to the use of high NIR-pulse energies.

Angular Distribution

The last part of the here-presented electron data analysis is the extraction of the angular distribution represented by the anisotropy parameter β_2, which was introduced in detail in Section 2.2. Figure 5.17 shows the reconstructed angular distribution and the extracted beta parameters are displayed as well. For the extraction, the radial regions covering the two spin-orbit states of the 4d subshell of iodine, the photoelectrons of interest, were selected and marked. On the left side of the figure, the data for the UV-pump and 63 eV XUV-probe scheme is presented. The peak of the I $4d_{3/2}$ state has the central position at pixel 113 and the I $4d_{5/2}$ state at 128. For the angular distribution calculation, the region of ± 6 pixels around the central peaks was included for both states, visualized via blue and green lines, respectively. The calculated β_2 parameters are -0.09 (in orange) and -0.01 (in red) in this sequence. Similar β_2 parameters were retrieved for the NIR-pump and 75 eV XUV-probe data, 0.07 (orange) and -0.01 (red) extracted from the radial range 177.6 ± 3 and 185.4 ± 4 pixels, respectively. Even higher Legendre polynomials were included, and higher beta parameters β_l for $2 < l \leq 10$ delivered tiny contributions, as expected for a single-photon ionization process. The anisotropy parameters are all close to 0, which implies an isotropic angular distribution of the photoelectrons. Furthermore, the extracted beta parameters for the $4d_{5/2}$ state are the same. The β_2 for the $4d_{3/2}$ state differ, which is most probably due to uncertainties of the Abel inversion performed on the less pronounced peak with fewer statistics. However, a deviation could additionally stem from the substantially differing and non-perfect degree of circular polarization of FLASH, which depends strongly on the photon energy, as demonstrated by von Korff Schmising et al. [188]. For 63 eV and 75 eV, a degree of 80 % and 66 % of circular polarization is expected, accordingly.

Lastly, a quick check about the sensitivity of the Abel inversion regarding the image processing was performed, by first Abel inverting the unmasked image, which delivered the same result. Meaning that the bright spots in the middle were not disturbing too much. The reason, therefore, is, that the rings of the two spin-orbit states are placed not too close to the center of the detector. Second, the image was symmetrized, which delivered again the same results, confirming that there is little anisotropy in the angular distribution of the photoelectron data. Therefore, the initial aim to measure the PECD of the two states could not be performed because only a tiny anisotropy could be identified, most probably a result of the low repetition rate of 10 Hz for the here performed OL-pump and XUV-probe experiments. Another educated guess is that at the operated temperature of the molecular jet, possibly two conformers existed with opposite signs, which PECD on average canceled out [189]. In light of future experiments, a chiral molecule with one conformer could be chosen in combination with more statistics.

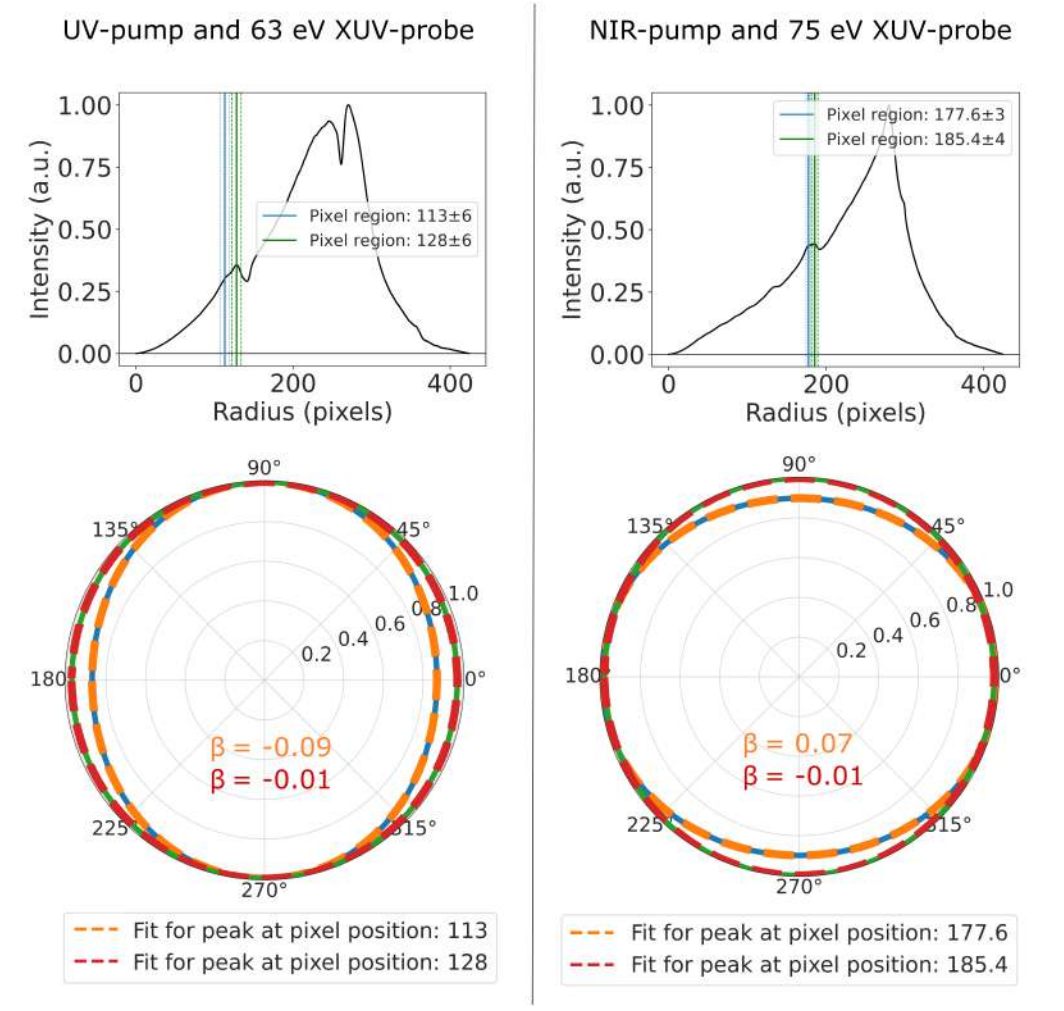

Figure 5.17: Selected pixel region of the radial distribution for the I $4d_{3/2}$ and $4d_{5/2}$ states, marked by blue and green dashed lines respectively, on the top and the corresponding calculated β_2 parameters, in orange and red respectively, on the bottom. On the left, for the UV-pump pulses combined with 63 eV XUV-probe pulses, and on the right side, NIR-pump pulses preceding the 75 eV XUV-probe pulses from FLASH.

5.5.2 Ion Data

The ion data, detected at the top side of the dVMI, is presented in the following. First, the OL-induced fragmentation patterns of the molecule and corresponding branching ratios, in dependence on the optical laser intensity, were studied. The data, which contains the mass-over-channel spectra, was out coupled of the MCPs. All presented spectra were calibrated as elaborated in detail in Section 5.4.2.

Fragmentation Patterns and Branching Ratios

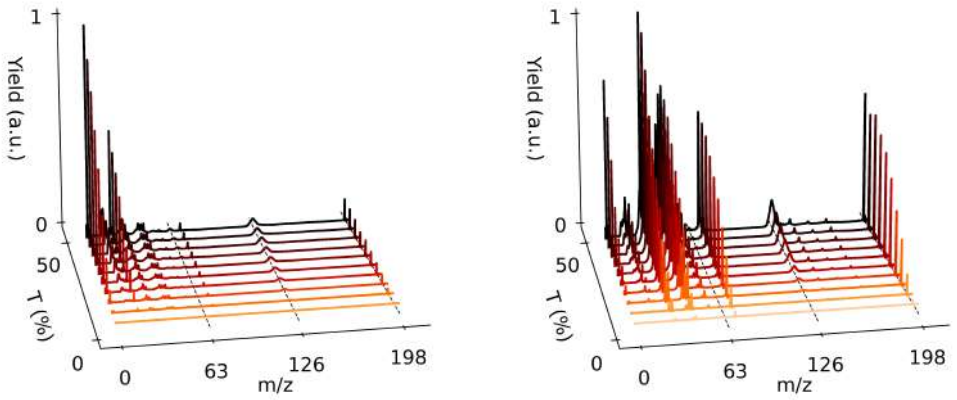

(a) UV 267 nm **(b)** NIR 800 nm

Figure 5.18: OL transmission scans represented for both OL-pump wavelengths, (a) 267 nm and (b) 800 nm, the mass spectra are plotted in dependence of the relative laser transmission (T) ranging from 5 % to 50 %. Cations are represented on the x-axis by their mass over charge (m/z) and are normalized to the highest peak.

Here, the dissociation of 1-iodo-2-methyl-butane via two OL wavelengths and a variety of OL pulse intensities is studied, regarding its ion formation mechanisms, without XUV probe pulses. First, the molecule's dissociation yields are presented for the two different OL-pump wavelengths, UV and NIR. The data provides insight into the respective branching ratios in dependence of the relative laser transmission, which was varied in steps of 5 %, ranging from 5 % to 50 % OL transmission, corresponding to the pulse energy/intensity ranges from 0.05 µJ to 87.8 µJ/$(0.4 - 5.2) \cdot 10^{12}$ W/cm^2 and 0.36 mJ to 1.16 mJ/$(1.3 - 4.1) \cdot 10^{14}$ W/cm^2 for the UV and NIR pulses, respectively.

The time-of-flight mass spectra by either UV or NIR pulses as a function of their relative laser transmission are presented in Figures 5.18 - 5.22. Comparing the transmission-dependent ion spectra for UV and NIR in Figure 5.18 it can be seen that the fragmentation patterns of $C_5H_{11}I$ differ. A detailed overview of the most prominent cationic fragments is shown in Figure 5.19 for the UV pulses and for the NIR pulses in Figure 5.21. In the following, mass-over-charge information is extracted and compared for both OL-pump pulses.

The cationic dissociation products are (except for three additional fragments in the NIR mass spectrum, which will be elaborated on below) the

same. Singly charged cationic parent fragments, $C_5H_{11}I^+$ (m/z of 198), are at the right edge of all displayed mass spectra and mostly monotonously rising with increased irradiation levels. For the NIR at 45 % transmission, there is a statistically valid minimum, indicating a potential resonance. The UV mass spectra yield strong contribution by the H^+ (m/z of 1) and H_2O^+ (m/z of 18) cations, with a ratio 2:1 (Figure 5.19). In comparison, CH_2CH^+ cations (m/z of 27) represent the highest yield in the NIR mass spectra (Figure 5.21). The relative yields of the parent ion M^+ at 198 m/z, mother fragment $(M\text{-}I)^+$ at 71 m/z and various alkyl groups $C_nH_x^+$ (n=2-4 and x=3, 5, and 7), which constitute the m/z from 27 to 55, are, compared to the absolute yield among all cations, much higher in the NIR mass spectra. Their prominence and absolute yield are by a factor of 4 smaller in the UV mass spectra, which follows due to the low pulse energy of the UV pulses and thus the dominantly induced neutral dissociation of the molecule at the C-I bond. Whereas for the NIR pulses, multiple fragmentation channels were populated, resulting in more ionic channels, and yielding several pathways with comparable abundance. Furthermore, the multi-photon dissociation via the NIR pulses yields several additional ionic channels in the mass spectra, more specifically the three additional peaks at m/z with a value of 141, 155, and 169. These three channels result from NIR pulses predominately dissociating the molecule at the C-C and not C-I bond. The 169 m/z peak, which represents the $(M\text{-}CH_3)^+$ fragment, shows the highest yield for the transmission at 45 % and seems to be the contra part for the above-mentioned minimum of the M^+ peak. Noticeable for both mass spectra is also the relatively high amount of H_2O^+ cations, which comes from the residual gas in the chamber.

The mass-over-charge calibration of the spectrometer was performed using xenon atoms. The additional nine peaks in the NIR mass spectra around the I^+ (upper-right corner in Figure 5.21), at m/z values 124, 126, 128, 129, 130, 131, 132, 134 and 136, are singly ionized xenon isotopes, produced via multi-photon ionization by the NIR laser as remainder of a previous calibration procedure and residual Xe in the chamber. It is noteworthy that the missing Xe signal for the UV case is solely caused by the absence of the residual Xe gas due to the sequence of calibrations.

Figure 5.20 and Figure 5.22 visualize the branching ratios of selected cations as a function of the relative OL transmission. To ensure a proper comparison across the different transmissions, each cation yield was normalized to the yield of the corresponding parent ion. This normalization is required because with an increase in the relative OL transmission, thus the increase in the OL pulse energy, an increment in the relative parent yield is induced as well. Represented cations in the two figures are I^+ (127 m/z), I^{2+} (63.5 m/z), $C_5H_{11}{}^+$ (71 m/z), $C_3H_7{}^+$ (42 m/z), and $C_2H_3{}^+$ (27 m/z). The changing yields, here with emphasis on the I^+, are an indication of different charge-up and dissociation pathways, which are the basis for the respective intensity choice for the time-resolving experiments presented below in the next Section 5.6. The

other fragments shown are a benchmark for reference. Corresponding pulse energy (top) and laser intensity (bottom) regimes can be found on the two additional x-axes of each figure.

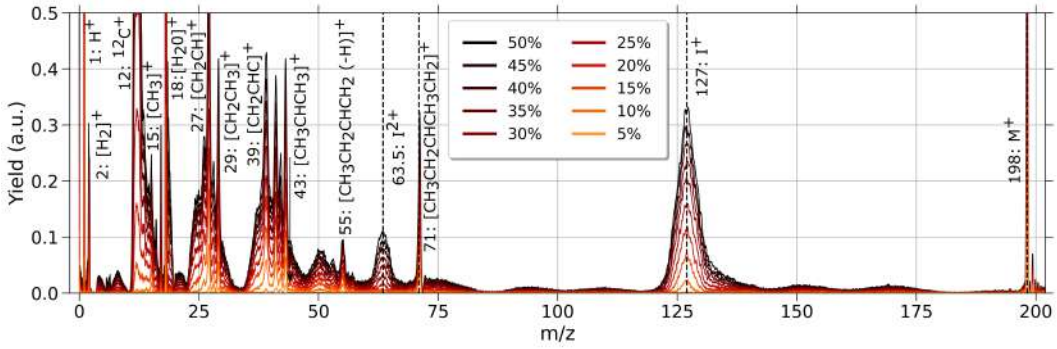

Figure 5.19: Mass spectra for different relative UV laser transmissions. The most prominent peaks are labeled. The yield of the cations in arbitrary units, plotted on the y-axis and normalized to the strongest peak H^+ at 1 m/z.

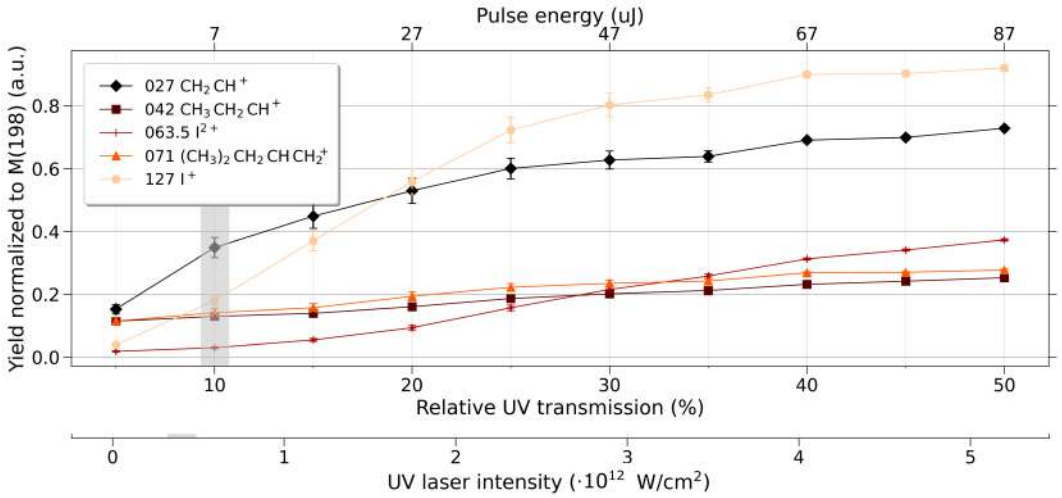

Figure 5.20: Yield of specific cationic fragments as a function of the relative UV laser transmission, ranging from 5 % to 50 % (plotted on the first bottom x-axis). Corresponding pulse energies are placed at the top x-axis and the intensities on the second bottom x-axis. Each value was normalized to the parent yield. Plotted are the mass over charges 27, 42, 63.5, 71 and 127. The lower intensity regime of the UV pulses, which was used for the below-presented UV-pump XUV-probe data, is shaded in light gray.

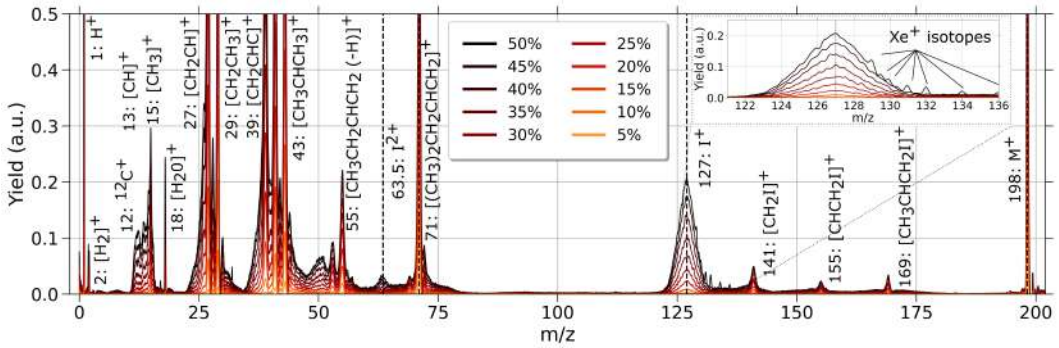

Figure 5.21: Mass spectra as a function of the relative NIR laser transmission. Plotted are the mass over charges against their yield in arbitrary units. The most prominent peaks between 1 and 198 are annotated to the corresponding fragments. The base peak is CH_2CH^+ with m/z 27.

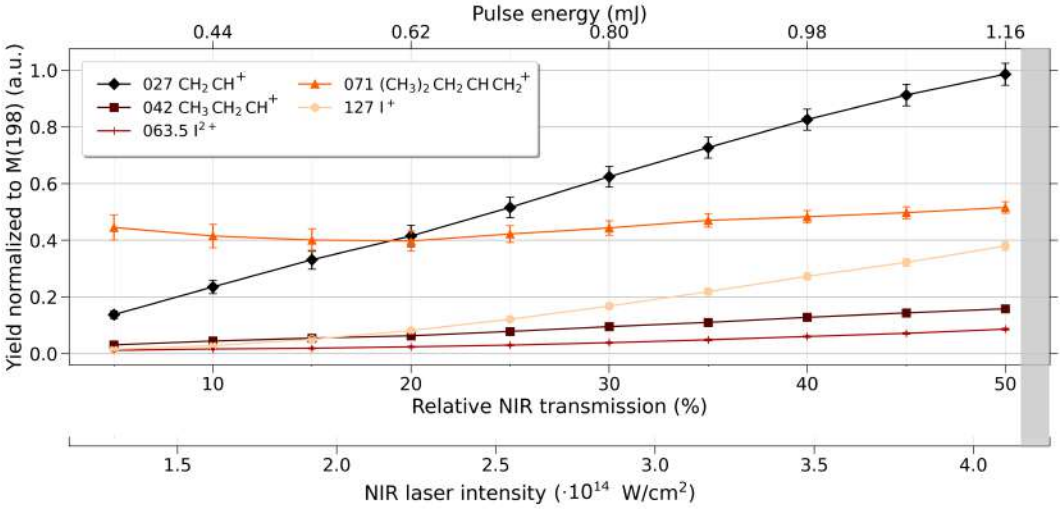

Figure 5.22: Yield of specific cationic fragments as a function of the NIR laser transmission. Corresponding pulse energies are placed at the top x-axis and the intensities on the second bottom x-axis. The yield is normalized to the yield of the parent cation with m/z=198. The higher intensity regime of the NIR pulses used, for the below-presented NIR-pump XUV-probe data, is shaded in light gray.

As mentioned before, the goal for the UV-pump XUV-probe experiments (results presented in the next Section 5.6) was to dominantly trigger a neutral dissociation into the neutral iodine atom and the C_5H_{11} alkyl fragment induced by the OL pulses and probe its evolution via FEL pulses. Therefore, the UV pulse energy was chosen to be in the vicinity of the threshold for the appearance of the I^+ fragment, the balance between ensuring sufficient excitation of this channel and minimizing the contribution from competing multiphoton

dissociation pathways. As visualized in Figure 5.20, the yield of the singly charged iodine fragment (yellow dots) increases drastically as a function of the relative laser transmission and is quite dominantly produced at higher intensities. Hence, the low UV pulse energy of 7 µJ (10 % relative UV transmission, intensity $0.4{\cdot}10^{12}$ W/cm^2 - area shaded in light gray) was used to perform the delay-dependent UV-pump, and XUV-probe experiments presented next and also in detail discussed by Allum et al. [106].

On the contrary, singly charged iodine fragments were probed for the NIR-pump XUV-probe experiment (presented in Section 5.6). As shown in Figure 5.22, the overall yield of the singly charged iodine fragments does not show a comparably considerable prominence (yellow squares). It shows a moderate increase with the increment of the relative laser transmission, and the total yield is comparably small to other fragments. To ensure a sufficient number of iodine fragments that can be probed by the XUV pulses, a high relative NIR transmission of 55 % (pulse energy ∼1.25 mJ, intensity $4.3{\cdot}10^{14}$ W/cm^2 - area shaded in light gray) was chosen to be used for the respective pump-probe experiments presented in the next Section 5.6 in Figure 5.23 and 5.25.

5.6 Time-dependent Results of the Ion Data

In order to perform pump-probe experiments, first the spatial and temporal overlap between the OL and XUV pulses was established. The spatial overlap was performed via a frosted YAG, which was for the alignment driven into the center of the dVMI spectrometer and afterward removed again. A camera captured the light of the YAG screen and both beams, the OL and XUV, were visible. The OL was steered via a mirror in the OL hutch. The spatial overlap was also checked frequently due to the already mentioned drift of the OL over a few hours (Section 5.4.4). The temporal, thus the synchronized arrival time of the OL and XUV pulses on the target, referred to as time zero t_0 in the following, was retrieved via the delay scans, thus varying the relative time delay between the OL and XUV pulses and the analysis of the time-dependent Coulombic driven channel, defined as region 2 in the following, presented in detail in Section 5.6.2.

5.6.1 OL-Pump XUV-Probe Experiments

Mass spectra showing the fragmentation of the molecule by either UV/NIR pulses (orange) or XUV pulses (gray), as well as both pulses at two different time delays (red and black), are plotted in Figure 5.23. For the mass spectra involving XUV pulses, the pulse energy fluctuation was corrected on a shot-

to-shot basis via the GMD data, as in detail discussed in Section 5.4.1. The upper plot belongs to the UV-pump experiments and the lower plot to the experiments performed with NIR pulses. As already mentioned before, contributions of stray-light-induced background electrons were neglected by the usage of fast HV switches (Behlke HTS31-GSM) that define a temporal window of operation for the MCPs. However, this kind of pulsed operation induced a substantial ringing on the ion side spanning over m/z values up to 35 that can be mostly subtracted in post-analysis. Persisting artifacts up to m/z of 13 are not shown for a more intuitive illustration. This cut-out is not critical because no pump-probe features were observed in this mass-over-charge range. Nevertheless, some foothills between 13 m/z and 40 m/z can be still seen in the UV-only mass spectrum (upper orange spectrum in Figure 5.23).

In the following, first, the UV-pump XUV-probe mass spectra are analyzed in detail (top plot in Figure 5.23). Discernible is that the total yield of the ionic fragments, resulting from multiphoton dissociative ionization, is much smaller with UV pulses (orange) than with XUV pulses (gray). Almost no charge states of iodine and only a few ionic channels with low yield (parent, mother fragment, and alkyl groups) are created via the low-intensity UV pulses. Whereas, several ionic channels more were produced by the XUV pulses. The XUV photon energy of 63 eV in this first experimental part was just above the binding energy of the neutral iodine 4d edge of the intact molecule, i.e. M-I $4d_{5/2}$ at ∼56.5 eV and $4d_{3/2}$ at ∼58 eV (note that the binding energy of the neutral atom after dissociation was measured to be ∼58 eV and 59.5 eV for the same states, respectively [106]) resulting in few charge states of iodine: I^+, I^{2+} I^{3+} and I^{4+}. Since it is not sufficient to core ionize ionic iodine, neither in the molecule nor as atomic ion (binding energies in the order of 70 eV), double Auger-Meitner relaxation is expected to be the most prominent origin, but also excited states in the cation and/or charge transfer mechanisms from other sites of the molecular system can contribute to these rather high charge states. While the I^+ peak is independent of the pump-probe delay, clear pump-probe features can be seen, i.e. for I^{2+}, in the red mass spectrum (UV early), where the UV pulses preceded the XUV pulses by 500 fs which corresponds, among other possibilities, to the introduced and anticipated channel of neutral dissociation and subsequent ionization of the 4d electrons after channel-closing, i.e. the generation of doubly charged atomic iodine. Due to the deliberately chosen low relative laser transmission for the UV pulses followed by little creation of iodine charge states, the most prominent delay-dependent effect with a significantly enhanced yield is noticeable at the I^{2+} peak with the m/z of 63.5. Meaning that this channel results from a neutral dissociation of the molecule into iodine and the alkyl group induced by the UV pulses, and is followed by ionization of the iodine atom via the XUV pulses resulting in an Auger-Meitner decay and the creation of I^{2+} with I^* the spin-orbit excited states:

$$C_5H_{11}I + UV \rightarrow C_5H_{11} + I^* + XUV \rightarrow C_5H_{11} + I^{2+}$$

At larger internuclear distances, the charge transfer between the fragments becomes impossible, and the charge vacancy cannot be distributed between the atomic iodine and mother fragment, thus the evolution of the (time-dependent) I^{2+} yield is an indication of channel closing mechanisms [173]. The same effect can be identified for the delay-dependent peak at m/z 42.3, representing the I^{3+} fragment, as expected from a double-Auger-Meitner yield in the order of 15 % [190, 191]. This yield shows a smaller pump-probe signal in comparison to the I^{2+} peak. Molecules, which interact first with the XUV pulses and second with the 500 fs delayed UV pulses are visualized as well in the mass spectra (visualized via the black line). Here, the UV pulses post-ionize the highly excited molecular fragments created by the XUV pulses, leading for exapmple to the higher yield of singly-charged iodine cations.

The situation is distinctly different for the second part of the experiment, where the OL-pump trigger is realized via NIR-laser pulses (details see experimental section). Here, the NIR-pump and XUV-probe mass spectra (bottom plot in Figure 5.23) are already different due to the much higher chosen pulse energy of the NIR-pump pulses, and their inability to resonantly excite the molecule through single-photon absorption. As already briefly discussed, the multiphoton dissociative ionization is much more pronounced with the NIR than UV pulses, which results in several ionic fragments (orange), including as well the iodine charge state I^+. Generally, the highest yields can be seen again in the black mass spectrum, where XUV pulses arrive 1 ps before the NIR pulses. Delay-dependent "laser-early" peaks can be seen in the red mass spectrum for the case of a 2 ps delay. Compared to the previously discussed UV-early XUV-late mass spectrum, the same delay-dependent peaks at m/z 42.3 and m/z 63.5 can be identified, with an increased strength for the former and similar abundance for the latter. I^{2+} fragments appear less prominent, due to the lower number of neutral iodine created via the relatively strong NIR pulses. In contrast, the additional I^+ fragments created by the NIR pulses, lead to a more prominent pump-probe signal at the I^{3+} fragment as a consequence of the higher XUV photon energy in this part of the experiment, which is sufficient for core-ionizing singly charged iodine. The observed pump-probe signal in the I^{4+} yield is consistent with the mentioned double-Auger yield. Residual Xenon from a previous calibration is annotated in the inset, also showing a small pump-probe effect as can be expected from similar mechanisms. Furthermore, two additional delay-dependent channels, not shown in an additional inset, appear with a tiny contribution, HO^+ at m/z 17 and CHI^+ at m/z 140.

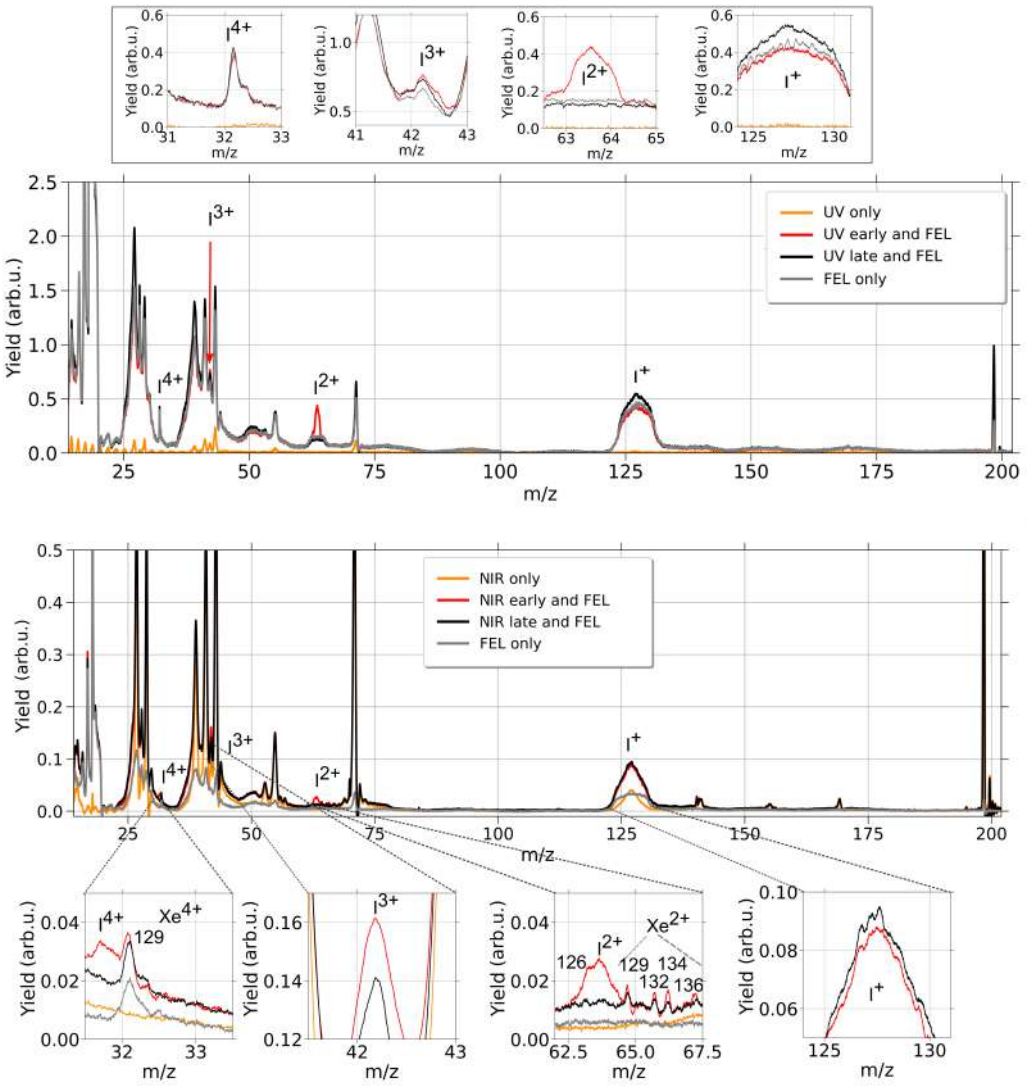

Figure 5.23: Mass spectra of 1-iodo-2-methyl-butane for different pump and probe schemes. On the top for the UV and on the bottom for the NIR pulses, with an intensity of $0.4{\cdot}10^{12}\,\mathrm{W/cm^2}$ and $4.3{\cdot}10^{14}\,\mathrm{W/cm^2}$, respectively. Compared are mass spectra resulting from the OL (orange), from the XUV-FEL ionization (gray), from OL-pump pulses 500 fs (UV) / 2 ps (NIR) before the XUV-probe pulses (red, laser-early regime) and lastly from the XUV-probe pulses 500 fs (UV) / 1 ps (NIR) before the OL-pump pulses (black, laser-late regime). Enlarged views are plotted for I^{4+}, I^{3+}, I^{2+}, and I^{+} fragments. Short cation flight times are subject to ringing due to electronic feedback from the pulsing of the high voltage of the electron detector. Masses <m/z=13 are therefore not analyzed. Xenon peaks result from residual gas of a previous calibration measurement.

5.6.2 Kinetic-Energy-Release Maps

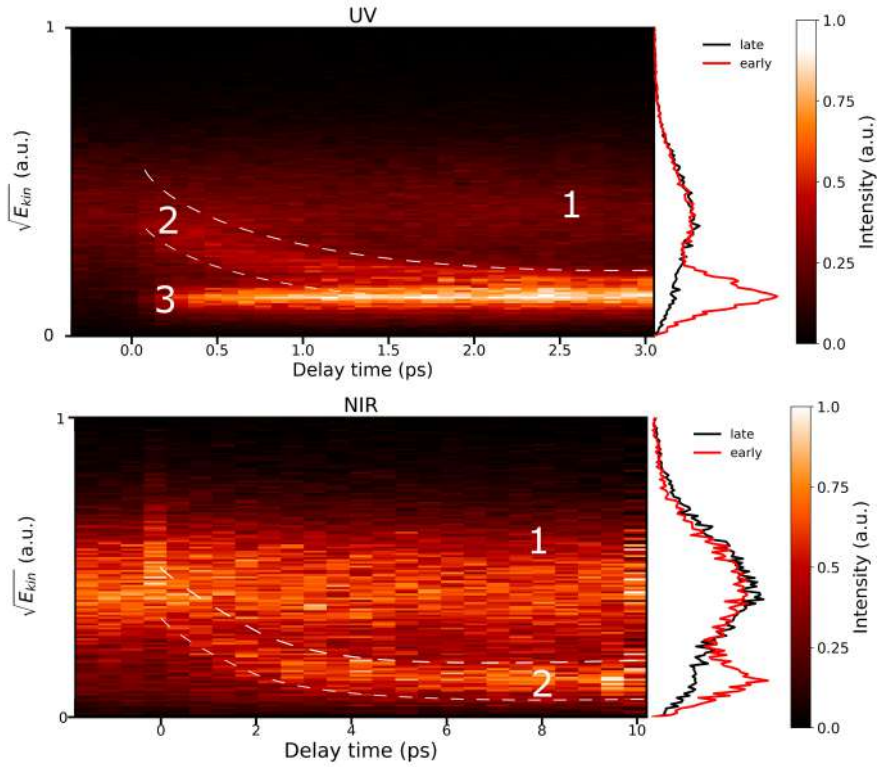

Figure 5.24: Radial distribution maps for the delay-dependent kinetic-energy distributions of I^{2+}: at the top the UV and at the bottom the NIR map. Three regions are marked, named 1, 2 and 3. Region 2 is highlighted by white-dashed lines. The projections of the kinetic energy axis are displayed next to the maps: UV/NIR late in black for delays -0.25/-1 ps and UV/NIR early in red for delays +2/+5 ps. Notebook for data analysis adapted from [192].

Delay-dependent effects can be studied in yet more detail by investigating the kinetic energy (KE) dependence of selected ionic fragments, such as I^{2+}, and their respective yields for various pump-probe delays, in a so-called ion kinetic-energy-release (KER) map. KER refers to the energy released during a chemical or physical process, typically in the form of the kinetic energy of the products. In the context of molecular or atomic reactions, KER is often used to describe the energy released when a molecule or atom undergoes dissociation or fragmentation into smaller fragments. Here, we study the Coulomb-driven OL-induced dissociation of the C-I bond and its timescales, as well as compare them for the two OL-pump wavelengths. Delay scans were performed by varying the arrival time between the OL and XUV pulses, covering ranges before (negative delay times, XUV before OL) and after (positive delay times, OL before XUV) time zero. For the UV-induced fragmentation, a scan in steps of 100 fs, covering a 3.5 ps range starting at -0.5 ps and ending at 3 ps, is presented. The covered delay time range for the NIR laser was

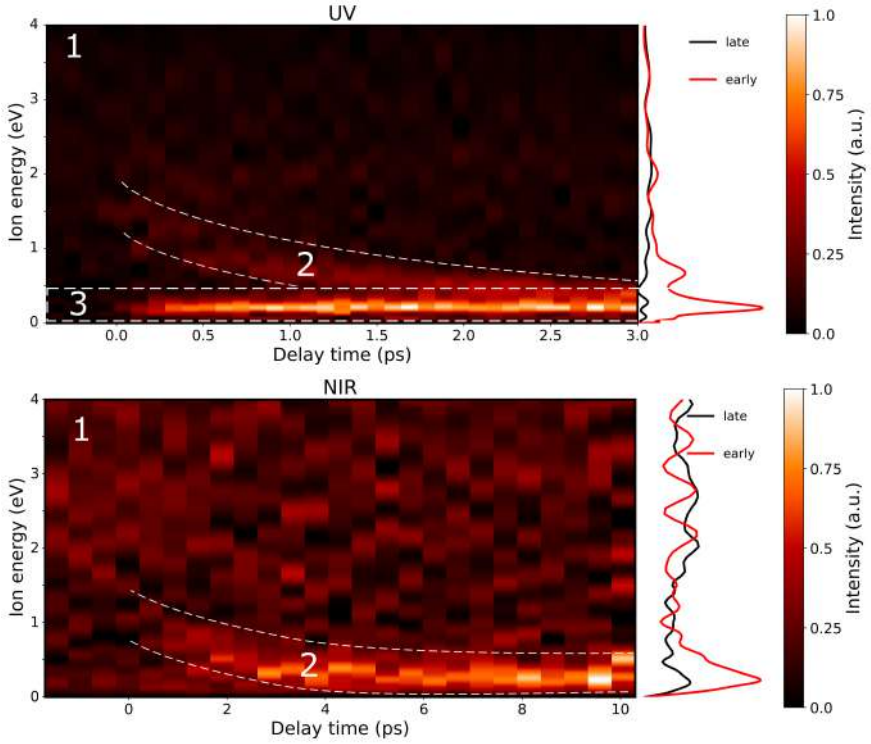

Figure 5.25: Ion kinetic energy release maps for the delay-dependent kinetic-energy distributions of I^{2+}: at the top the UV and at the bottom the NIR map. Three regions are marked, named 1, 2 and 3. Region 2 and 3 are highlighted by white-dashed lines. The projections of the kinetic energy axis are displayed next to the maps: UV/NIR late in black for delays -0.25/-1 ps and UV/NIR early in red for delays +2/+5 ps. Notebook for data analysis adapted from [192].

12 ps, ranging from -2 ps to 10 ps, with scan steps of 500 fs since the observable processes cover a longer range than in the UV-case. The corresponding ion kinetic-energy-release maps are visualized once by direct plotting of the radius (equivalent to $\sqrt{E_{kin}}$) in Figure 5.24, and second after the conversion into the corresponding kinetic energy of the ions, shown in Figure 5.25. As shown in both figures (top for UV pulses and bottom for NIR pulses) the delay range is plotted on the x-axis, ranging from the OL early (right, positive delays) to OL late (left, negative delays) regimes. One exemplary energy-dependent ion spectrum is plotted vertically between the KER map and intensity color bar for the UV/NIR early regime in red picking out the delay at +2/+5 ps and one for the UV/NIR late in black for the delay time -0.25/-1 ps. The y-axis contains the square root of the kinetic energy in arbitrary units, which is proportional to the radial distribution of the measured I^{2+} fragments (Figure 5.24). In Figure 5.25, the y-axis shows the ion energy in eV, which was derived from the PImMS camera velocity-map images and the used pBASEX Abel inversion algorithm [193]. A detailed insight into the data analysis has been examined recently in [106].

The Coulomb repulsion of the fragments, which is mapped in the kinetic-energy-release distribution, decreases with an increasing radius R between the dissociating fragments. These maps furthermore represent the dominance of the different pump-probe-dependent and independent fragmentation pathways. Up to three regions can be identified, marked 1, 2 and 3. Region 1 comprises a broad feature in the UV and NIR map, covering a wide KE region between 1 eV and 3 eV and being independent of the delay time. I^{2+} fragments in this region originate from molecules that did not interact with the OL-pump pulses or did not dissociate after the interaction. These molecules were multiphoton ionized only via XUV photons at different indistinguishable internuclear distances during the Coulomb repulsion of the molecule to produce mutually repelling I^{2+} and ionic alkyl cofragment(s), resulting in a wide KER spread covering the high-energy part of the KER maps. Moreover, region 1 is much more pronounced in the NIR map, which can be mainly attributed to a higher FEL intensity in this experimental part and thus more multiphoton ionization via the XUV pulses.

Region 2 is the delay-dependent Coulomb channel and decreases in the form of a horizontal asymptote from high ion energies to low energies approaching region 3. Here, the molecule interacts with the OL and the XUV ionization follows the OL-induced dissociation, ending in two charged fragments. With larger delays between the pump and probe pulses, the internuclear distance R increases due to the Coulomb repulsion, and hence the measured ion KER decreases due to channel closing and no further electron charge transfer between the dissociative fragments. This region is shaped by the Coulombic repulsion of the mother fragment (or a subset of it) and the ejected iodine atom. These internuclear-distance dependent channels can be formed by various processes elaborated in the following: 1. The single charge-up by the OL where the mother fragment keeps the charge and the iodine is ejected ($C_5H_{11}^+$ + I) and subsequently the iodine is ionized by the FEL, forming I^{2+} with no charge transfer after the subsequent ionization step. 2. The single charge-up of the iodine atom and subsequent ionization by the FEL. The charge is then transferred to the mother fragment ($C_5H_{11} + I^+ \xrightarrow{XUV} C_5H_{11} + I^{3+} \xrightarrow{CT} C_5H_{11}^+ + I^{2+}$). 3. Via created single-charge states by the OL at both, the mother fragment and the iodine atom ($C_5H_{11}^+ + I^+$ with subsequent ionization of the valence shell of the iodine atom and no further charge transfer. This case seems to be least probable due to the small cross-section of the iodine valance in comparison to cross section of the remaining constituents. 4. Via neutral dissociation as discussed above and valance FEL-photon absorption the residual-fragment site and core ionization at the iodine. 5. Via neutral dissociation as discussed above and sequential FEL-photon absorption at the iodine and the residual-fragment site. 6. Via higher-order charge-up of the intact molecule with break-up into charged fragments and doubly charged iodine and more. At the moment it can not be claimed, which process is the most probable. The calculations are still ongoing [194]. Nonetheless, due to the slow dynamics, it can be assumed that a channel, including only one charge

fragment after the interaction with the OL, for example in process 1, is more probable. Channel, which contains after the OL interaction two charges fragments, would repulse each other from the beginning and faster dynamics are expected. But as already mentioned, this needs to be further confirmed by theory.

Region 3, in this study only visible in the UV-pump XUV-probe KER map (top maps in Figures 5.24 and 5.25), shows delay-dependent features at low ion energy and is constantly placed around the ion energy band at 0.25 eV, as discussed in detail in [106]. These I^{2+} fragments, result from the XUV ionization of the OL excited C_5H_{11} + I^* channel (see Figure 5.2). This channel yields two independent neutral fragments. XUV-ionization occurs solely at the isolated iodine atom leading to the final channel C_5H_{11} + I^{2+}, as already mentioned before. The doubly charged iodine fragments carry little kinetic energy, indicating that they come from a dissociation with a neutral fragment. This channel is the most pronounced one for the UV case under the given experimental conditions, which follows from the previous data and the discussion of the results presented above. The reason for the absence of this channel in the NIR maps (see bottom maps in Figure 5.24 and 5.25) is probably due to the high pulse energy of NIR pulses, which ionizes the target producing less neutral fragments.

Looking into the integrated yield of the I^{2+} peak of the channel leading to region 2 (red points) as a function of the pump-probe delay, an estimation of the timescales of the underlying processes can be extracted via a fit of a Gaussian cumulative distribution function (black line), see Figure 5.26 ((a) for UV and (b) for NIR). The yield of this time-dependent Coulombic interaction peak increases within the first few 100 fs (UV)/few picoseconds (NIR). The width of the fitted Gaussian function (σ) differs for the two used OL. For the UV pulses a value of σ=0.2 ps was retrieved. In stark contrast, for NIR excitation, the timescale for the formation of region 2 signal is several times slower with σ=0.9 ps, implying that there is a substantial time between interaction with the NIR pulse and the ultimate fragmentation. This can be explained by considering the PECs presented in Figure 2.5. The high NIR pulse energy excited the molecule most probably into different PECs, leading to dissociation via a different reaction coordinate, involving more complex structural rearrangements that are characterized by longer timescales.

The integrated yield of the I^{2+} peak of the neutral channel in region 3 located at approximately 0.25 eV delivers, considering the kinetic energy range of ∼0.2-0.35 eV, a value of σ=0.3 ps (see Figure 5.26(c)). Furthermore, it should be noted that the intensity yield maximum is not at time zero but shifted to larger delay times, located at 0.6 ps. This is due to charge transfer, which still occurs at early OL-pump XUV-probe delays. If the two fragments are in close proximity, which is the case for small time delays around t_0, the neutral C_5H_{11} fragment will not remain neutral in the vicinity of the doubly

charged iodine ion but become singly charged via electron transfer.

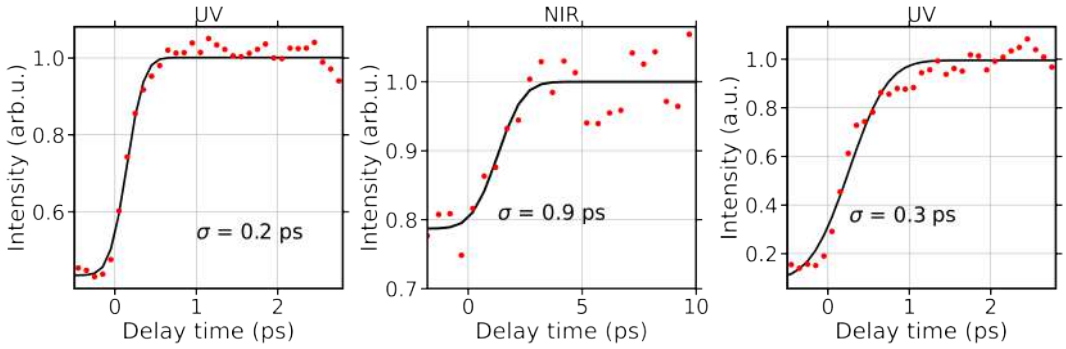

(a) UV region 2 **(b)** NIR region 2 **(c)** UV region 3

Figure 5.26: Integrated yield of the ion-energy channel I^{2+} of region 2 for UV (a) and NIR (b) as a function of pump-probe delay (represented by the red points) with a fit to a normal cumulative distribution function (plotted via the black line). The center of the fitted Gaussian function is indicated with σ. (c) CDF for the neutral channel in region 3. Notebook for data analysis adapted from [192].

The channel of region 2 was furthermore used to find t_0, due to the fact that the appearance of the additional charge on the alkyl mother fragment minimizes the probability of charge transfer, thus this channel can be probed via the XUV pulses immediately after the excitation with the OL pulses and the increase in yield of this channels is not retarded as for example for the channel in region 3, which was just elaborated above.

5.7 Partial Electron-Ion Covariance

In the above-shown data analysis, the simultaneously detected electrons and ions were analyzed individually and not correlated with each other. Here, the partial covariance between the simultaneously detected particles was applied and used to follow the dynamical changes of iodine. It was demonstrated that the iodine can be followed via XUV-probe pulses during the transition from a molecular into an atomic environment, after the UV-induced neutral C-I bond dissociation. The main results will be in the following presented shortly. All shown figures were taken and adapted (colors) from the previously published work [106].

During the transition from the molecular into the atomic environment, chemical shifts occur, which are the change in the electron binding energy. The chemical environment has an impact on the binding energies of core electrons. These changes are in the order of few electronvolts and this chemical shift in binding energies can be measured via photoelectron spectroscopy.

The photoelectron spectra were recorded during the experiment using the bottom side of the CAMP-dVMI spectrometer. The data is presented in Section 5.5.1. The VMI images, visualized in Figure 5.13, contain all photoelectrons created during the light-matter interaction. The signals, which contain small changes in binding energies, overlap and can not be disentangled without applying additional methods. To follow the undergoing dynamics, it is required to isolate the detected photoelectrons of one specific (time-dependent) channel out of the signal containing signal from all fragmentation channels.

As presented in the study [106] electron-ion partial covariance imaging [195–198] can be applied. It is the covariance between selected photoelectrons and corresponding positively charged iodine fragments, corrected by the fluctuating FEL pulse energy. Generally, covariance is a linear measure of the correlation between two variables (here between each pixel of the electron image Y and the total count of the ion channel of interest, obtained from the centroided data X captured by the PImMS camera) [199–202] and defined as:

$$cov(X, Y) = \langle XY \rangle - \langle X \rangle \langle Y \rangle \tag{5.9}$$

The FEL pulse energy fluctuations lead to unstable experimental conditions on a shot-to-shot basis, resulting that all measured channels fluctuating together, becoming correlated. The FEL pulse energy normalization was furthermore already in detail motivated in Section 5.4. The term to remove the "false correlations" induced by the FEL pulse energy fluctuations and defined as I, which is the fluctuating parameter of interest and included in the correction term, is defined as:

$$corr(X, Y; I) = \frac{cov(X, I)cov(Y, I)}{cov(I, I)} \tag{5.10}$$

for the partial covariance follows then the equation:

$$pcov(X, Y) = cov(X, Y) - corr(X, Y; I) \tag{5.11}$$

Figure 5.27(a) visualizes all detected photoelectrons, similar to the presented one in Figure 5.13, which was analyzed independently of the here presented data. The retrieved binding energies of the background subtracted image (right image in Figure 5.27(a)) are visualized via the black curve in 5.27(c) and agree with the above-analyzed and previously shown data presented in Figure 5.16(c). Two peaks appear, which correspond to the iodine in the molecular environment, thus to an unpumped signal, and have values of 56.5 eV for I $4d_{5/2}$ and 58 eV for I $4d_{3/2}$. In comparison, photoelectrons originating from singly charged iodine fragments, mostly originating from the molecule interacting solely with the XUV pulses (iodine atom ionization followed by Coulomb explosion of the entire molecule, see Figure 5.19), were correlated with each other, and all other photoelectrons were filtered out. The corresponding VMI image is shown in the left image of Figure 5.27(b) labeled with cov(I^+,e^-). This image was corrected by the fluctuating FEL pulse energy corr(I^+,e^-), which image is shown in the middle of (b). The FEL pulse-energy correction is required due to the still significantly present background from the helium. The corrected image, shown at the right in (b), represents the partial covariance imaging of photoelectrons of the selected ion of interest, here the I^+ ions, labeled with pcov(I^+,e^-). It can be seen, that all other contributing photoelectrons, such as helium, disappear. The retrieved binding energies shown via the magenta curve in (c) (also shown in (e)) do not show a prominent shift in comparison to the binding energy retrieved from the background-subtracted raw image in black (shown in (c)), containing all photoelectrons and extracted from the presented right image in (a).

Therefore, the partial covariance of a distinct pathway, hence the time-dependent channel, which creates I^{2+} fragments only originating from the neutral dissociation (region 3 in the UV KER maps in Figure 5.24 and 5.25) was used and its partial covariance studied in more detail. This data, more precisely data for one specific time delay where the UV pulses preceded the XUV pulses by 550 fs, is visualized in the right image of (d) and labeled pcov(I^{2+},e^-). The binding energies are plotted in (e) in blue. As visible, the blue curve is shifted, in comparison to the magenta curve, to higher binding energies, i.e. 1.7 eV. This change can be also seen in the VMI images shown in (d). Here, the two outer photoelectron rings, originating from the two spin-orbit states of the iodine 4d shell, show different diameters. The two white-dashed lines are the guide to the eye and the rings in the right image show a smaller diameter. The binding energies in the blue photoelectron spectrum, presented in (e), deliver binding energies of 58 eV for the I $4d_{5/2}$ and 59.5 eV for I $4d_{3/2}$, which is consistent with the measured binding energies of free iodine atoms retrieved at synchrotron light sources [203, 204]. Thus at this time delay between the UV and XUV pulses, the transition from the ionic into the atomic environment already occurred. Furthermore, in stark contrast to previously performed studies [205], the less-prominent signal from the atomic iodine can be disentangled from the much stronger contributions from the unpumped molecular signal and other time-dependent channels. The presented photoelectron spec-

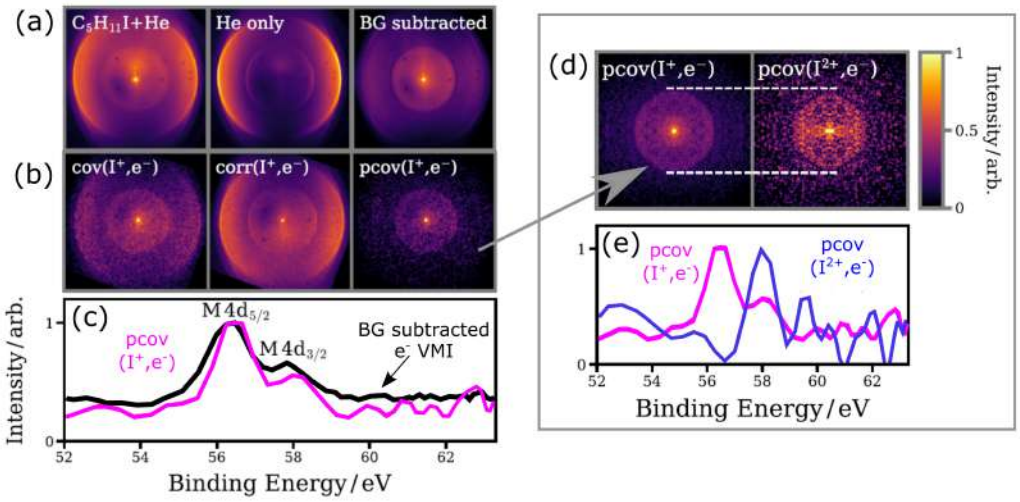

Figure 5.27: Photoelectron data: (a) photoelectron VMI images of the target molecule, helium background, and the background subtracted image (left to right), (b) partial electron-ion covariance (right), retrieved from the correlation (left) minus the correction term (middle), (c) photoelectron spectra from the right images of (a) and (b), colored in black and magenta, respectively. Comparison of the partial electron-ion covariance for the photoelectrons originating from the I^+ (left and already shown in the right image of (b) and I^{2+}. The to (d) corresponding photoelectron spectra are shown in (e). Figures adapted from [106].

tra were obtained by Abel-inverting the images using the pBASEX algorithm [193].

In the next step, the environmental transition of the iodine was followed in a time-resolved manner along the potential energy curves. The involved potential energy curves were presented in Figure 5.2 and the schematic representation is visualized as well in Figure 5.28(a). Two additional time delays at earlier transition times were chosen, which probe the iodine after the UV excitation and therewith induced neutral fragmentation. Data is shown for UV pulses preceding the XUV pulses by 0.05 ps (b) and 0.3 ps (c). Looking into (b), the initial state, from the unpumped molecule in the ground state pcov(I^+,e^-), is represented by the magenta curve, as already mentioned and shown before. These binding energies correspond to the molecular iodine 4d photoelectrons. Photoelectron spectra, extracted via partial covariance pcov(I^{2+},e^-) are visualized via the blue curve and correspond to data, quickly after time zero (close to the equilibrium bond distance) where the XUV pulses arrived 0.05 ps after the UV pulses. The theoretical photoelectron spectra, as a function of the distance between the dissociating carbon and iodine, are plotted in red for the excited triplet ($^3Q_0$) state and in black for the singlet ($^1Q_1$) state. It was

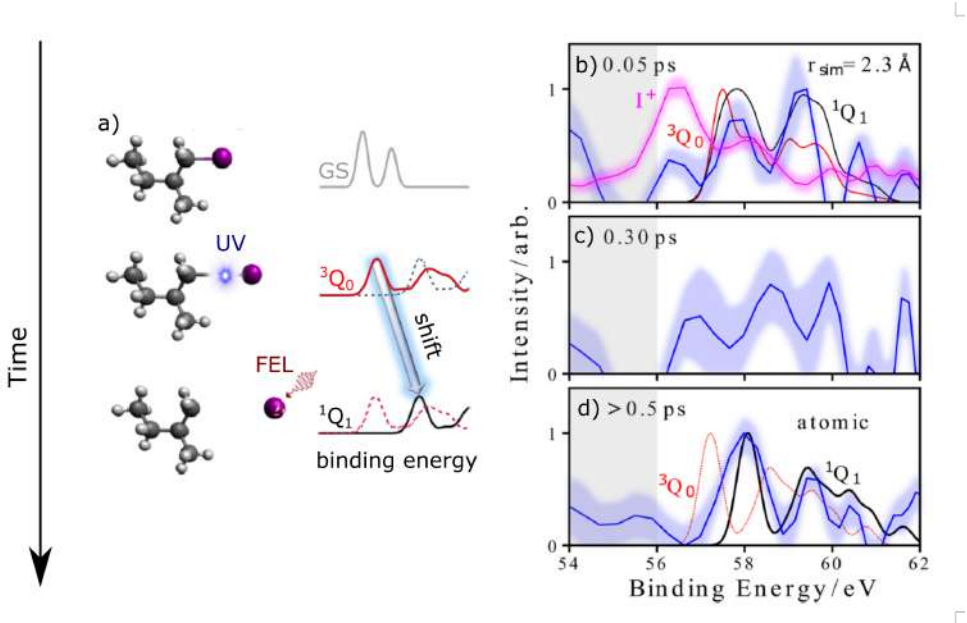

Figure 5.28: Dynamical changes of the target: (a) schematic representation of the molecule's different states, including the ground state (GS) and the via UV-pulses induced excited triplet state $^3Q_0$, which evolves with the time into the singlet state $^1Q_1$ and produces the atomic iodine. The binding energy shift is probed via XUV pulses at different time delays. The via partial electron-ion covariance retrieved binding energies are shown in blue for different time delays, 0.05 ps (b), 0.30 ps (c), and >0.5 ps (d). Corresponding theoretical calculations are also visualized in red for the triplet and in black for the singlet state. The magenta curve in (b) corresponds to the unpumped signal. The shaded areas around the magenta and blue curve, represent the estimated 1σ error. Figures adapted from [106].

calculated, that the conical intersection, where the population transition from the excited triplet state into the singlet state occurs, is at a bond distance of 2.4 Å, which is theoretically reached after approximately 10 fs (for more details see theoretical methods in [106]).

The experimental data for the time delay of 50 fs (blue curve) reveals first, that the yield of the I^{2+} fragments is lower due to the small bond distance and the possible charge transfer between the iodine and the mother fragment. Furthermore, by comparing the experimental and the theoretical data, it can be seen that the calculated transition is still not fully finished. There are still contributions from the triplet state, but as well from the singlet state. The two states, "cannot be clearly distinguished" an indication of "some convolution of both involved states" [106]. Panel (c) shows the data for the delay of 300 fs, where the theory predicts mostly contributions from the singlet state, which cannot be confirmed by the experiment. At this time delay, again a convoluted

state of the triplet and singlet state can be identified with a small change in comparison to panel (b). For the last time delay (>500 ps), at larger internuclear distances between C and I, shown in panel (d), the experiment confirms mainly the dominant contribution of the singlet state with a still small contribution of the triplet state, which causes the smaller binding energy shift visible by comparing the black and blue curves.

Chapter Six

Conclusion and Outlook

This work paves the way to the possibility of studying chiral dynamics with the usage of the 4th generation light sources, the free-electron lasers. Due to still unsolved questions regarding chiral molecules, for example, their formation, their investigation of electronic structure and relaxation dynamics from a specific atomic observer site on natural timescales is of utmost importance because chirality forms our daily life. Such studies are principally accessible with the here-discussed ultrabright and ultrashort FELs pulses, which are shaping the future towards time-resolved PECD of a chiral molecule using FELs.

Clear limitations are crucial so far, for example, the complexity of such experiments, the synthesis of enantiopure targets, the missing theory, the still not fully understood nonlinear physics induced by the high-intensity FEL pulses, the limited access to FEL facilities, the limited degree of circular polarization, the generally small PECD signal in the range of few percent, or also the extreme technical challenges by applying pump-probe techniques.

FELs light sources are single-user machines, making their operation costly and access to them much more limited than storage rings or tabletop sources. The reason why other sources, with easier access in comparison to FELs, are as well needed and therefore emphasized here. They offer furthermore other valuable and important observables regarding chirality studies from different excitation regions, which are essential for the overall picture.

An additional limitation can be the low repetition rate of the probing FELs pulses operated with OL systems delivering the pump pulses for specific experimental conditions, also applicable for the here-presented experiment performed at the FLASH FEL line FLASH1. This work, originally, aimed to measure the time-resolved PECD of the chiral molecule 1-iodo-2-methyl-butane. This goal could not be demonstrated, mostly due to a lack of statistics, a low degree of circular polarization, and low time resolution. Nonetheless, fragmentation benchmarks for further time-resolving studies of this prototypical chiral

molecule, also in terms of its photoelectron circular dichroism, were established and in detail presented. As a first step, the OL-induced dissociation of the prototypical chiral molecule 1-iodo-2-methyl-butane was characterized as a function of the OL's intensity, using UV (267 nm) and NIR (800 nm) pulses. A detailed picture of the induced fragmentation was presented for the given experimental conditions. Due to the lower pulse energies of the UV pulses, fewer ionic channels were induced in comparison to the NIR pulses, which were driven with higher photon pulse energies (3 orders of magnitude). These results can be used for further studies to choose the suited OL wavelength and pulse energy depending on the fragment of interest, especially in the light of PECD studies on this prototypical chiral molecule. In a second step, the OL-induced dissociation was site-selectively probed via femtosecond time-resolved inner-shell photoionization at the I 4d edge using the XUV pulses from FLASH1. To evaluate the timescale of the OL-induced dissociation, the yield of the I^{2+} fragments, which originate from the OL-induced dissociation into charged and Coulomb repulsive fragments, was chosen for the comparison, as the common time-dependent channel for both OL. The atomic iodine atom was ionized via XUV pulses and relaxed via an Auger-Meitner decay into the doubly charged iodine fragment. By analyzing the KER of this specific fragment as a function of different OL-pump XUV-probe delay times, it turned out, that the molecule dissociated faster after the UV-induced fragmentation in comparison to NIR-induced fragmentation. The UV dissociation was retrieved to be approximately 0.2 ps, while the NIR dissociation is characterized by $\sim$0.9 ps. This result originates most probably from the via the OL differently excited states. The UV pulses mainly triggered a neutral dissociation into the $3Q_0$ state, whereas, the dissociation triggered by the in pulse energy much higher NIR pulse proceeds along a different reaction coordinate(s), probably via more complex structural rearrangements that take significantly longer to evolve.

Moreover, the application of electron–ion partial covariance imaging was demonstrated for ultrafast site-specific photoelectron spectroscopy, revealing the ability to energetically distinguish between molecular and atomic levels at the iodine 4d edge. This methodology allows for a reliable assessment of covariant electron angular distributions and their dynamic evolution over time. Additionally, this approach has the potential to expand its utility to the detection of asymmetric photoelectron distributions and is a prospective tool for investigating ultrafast chiral dynamics in future PECD-based FEL experiments.

The imminent upgrades, of undulator-based helical light with a high degree of circular polarization and the increased repetition rate for the synchronized operation required for OL-pump and FEL-probe experiments, of the two FEL facilities, EuXFEL and FLASH2, potentially pave the way to the realization of the first time-resolved PECD. The for AMO purposes built SQS endstation at EuXFEL, was extensively commissioned, and the results of the commissioning and first experimental campaigns were presented in the light

of possible future chiral studies. EuXFEL is up-to-date, a unique FEL facility due to its high-repetition rate of up to 27 000 pulses per second. SQS offers versatile experimental chambers, which are suited to measure the angular distribution of photoelectrons either in the laboratory- or recoil-frame. Furthermore, the FLASH2 FEL will also produce soon undulator-based helical light, critical for chiral studies. Due to the large research engagement of various fields and groups, improvements targeting also the other above or here not explicitly mentioned limitations are ongoing. The relevance of studying chiral matter gained during the last few years an immense interest.

Lastly, the within this PhD project built and here-presented double-sided VMI spectrometer offers the possibility to detect photoelectrons and ions simultaneously at high repetition rates. This spectrometer is fully functional and can be used. The available spectrometers, FEL facilities and gained methodological, technical and scientific know-how are an enrichment toward the bright future of TR-PECD at FELs.

Chapter Seven

Appendix

7.1 Averaged and Uncorrected Electron Images

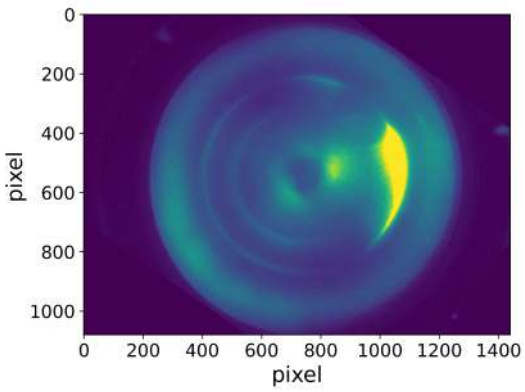

Figure 7.1: Electron image during single-mode operation. Corrected image plotted in Figure 4.17(c).

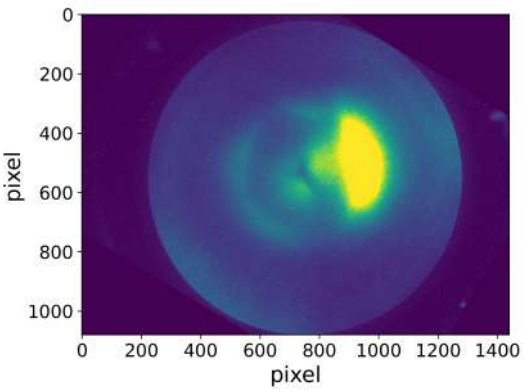

Figure 7.2: Electron image during dual-mode operation. The corrected image is plotted in Figure 4.20(c).

7.2 Experimental Parameters

Two experiments were presented in this PhD thesis, first the double-sided VMI commissioning beamtime at the PTB in Berlin (Chapter 4) and second the Free-electron laser beamtime at FLASH on the chiral molecule 1-iodo-2-methyl-butane (Chapter 5). The used experimental equipment and the related parameters are presented in the following in a bundled form.

7.2.1 PTB, DVMI Commissioning, 2022

MLS

- beamline: U125
- photon energy: 40 eV
- repetition rate: 550 MHz
- ring current: 133 - 70 mA
- spot size: 1 mm x 0.5 mm (hxv)

Molecular jet

- operation mode: continuous
- gas: argon
- backing pressure: 65 mbar
- nozzle diameter: 100 µm
- skimmer: BeamDynamics Model 1, nickel, orifice diameter 250 µm and 500 µm

Other

- spectrometer operation mode: single side and double side
- MCPs: chevron stack, active area 120 mm, pore size 25 µm, pore distance 32 µm, temporal resolution 2.5 ns
- P47 phosphor screen: light emission 400 nm, decay time 100 ns
- camera: Basler acA1440-73gm GigE vision, sensor size 1440 x 1080 pixels^2
- camera lens: Basler C23-0824-5M-P f8mm
- RGA: mks microvision 2, resolution 1-100 amu

7.2.2 FLASH, 1-iodo-2-methyl-buatne, 2018

Free-electron laser FLASH

FLASH1 branch setting 1

- photon energy: 63 eV
- energy bandwidth: ∼1 % FWHM
- repetition rate: 10 Hz
- pulse energy: 10 µJ
- pulse length: 80 fs FWHM
- spot size: 10 µm^2 FWHM
- optical laser: UV

FLASH1 branch setting 2

- photon energy: 75 eV
- energy bandwidth: ∼1 % FWHM
- repetition rate: 10 Hz
- pulse energy: 20 µJ
- pulse duration: 80 fs FWHM
- spot size: 10 µm^2 FWHM
- optical laser: NIR

Ti:Sapphire pump laser

UV settings

- photon energy: 4.6 eV
- wavelength: 267 nm
- repetition rate: 10 Hz
- pulse energy: 7 µJ- 176 µJ
- pulse duration: 150 fs FWHM
- spot size: 100 µm^2 FWHM
- intensity: (0.4-5.2)·10^{12} W/cm^2

NIR settings

- photon energy: 1.55 eV
- wavelength: 800 nm
- repetition rate: 10 Hz
- pulse energy: 0.45 µJ - 1.8 mJ
- pulse duration: 70 fs FWHM
- spot size: 60 µm^2 FWHM
- intensity: (1.3-4.3)·10^{14} W/cm^2

Molecular jet

- R/S-1-iodo-2-methyl-butane ($C_5H_{11}I$)
- carrier gas: helium, 1 bar
- target temperature: 45 °C
- nozzle diameter: 30 µm
- skimmer: Model 14 BeamDynamics, nickel, orifice diameter 150 µm and 350 µm
- aperture: 4 mm x 4 mm
- nozzle temperature: 80 °C

Other

- BBO crystal for UV generation: β-BaB_2O_4
- MCPs: chevron-stacked, active area 80 mm, pore size 25 µm, pore distance 32 µm, temporal resolution 2.5 ns
- P47 phosphor screen: light emission 400 nm, decay time 100 ns
- electron camera: Allied Vision Pike F-145 CCD camera, sensor size 1388 × 1038 pixels^2
- ion camera: PImMS, sensor size 324 x 324 pixels^2

7.3 Voltage Optimization Code for dVMI Mode

In the following, the Python code for optimizing the electrode voltages, for achieving vmi conditions on both spectrometer sides, is presented [206].

```
# importing needed libraries
import os
import time
import subprocess
import numpy as np
import scipy.optimize as opt
from IPython.display import Image
from bayes_opt import BayesianOptimization
from zoopt import Dimension, Objective, Parameter, Opt,
                  ExpOpt, Solution
```

```
#path to the simion software
os.chdir(r"/home/musicv/Desktop/SIMION-8.1")

#path to the simion file which has to be optimized
wkpath = r'/home/musicv/Desktop/double-sided_VMI'
```

```
# Definition of the metric for each spectrometer side
# VMI conditions for electrons
def VMI_metric_ele(results, last_metric = 1e3):
    X_arr = results[:,name2ind['X']]
    # x lies in the detector plane
    Y_arr = results[:,name2ind['Y']]
    # y lies in the detector plane
    Z_arr = results[:,name2ind['Z']]
    # z is the propagation direction of the particles
    Cg_arr = results[:,name2ind['Charge']]


    # 150 is the position of the MCP front on the electron side
    d2_accum = 0
    #checks the charge
    for i in range(3):
        assert Cg_arr[2*i+1]<0


        #checks if particle reaches the detector (150)
        if ((150.-X_arr[2*i+1]) != 0) or ((150.-X_arr[6+2*i+1])
                                          != 0):
            return last_metric*1e10

        d2_accum += ((Y_arr[2*i+1] - Y_arr[6+2*i+1])**2 + (
                                        Z_arr[2*i+1] - Z_arr[6+
                                        2*i+1])**2)
    return d2_accum
```

```
# VMI conditions for ions
def VMI_metric_ion(results, last_metric = 1e3):
    X_arr = results[:,name2ind['X']]
    Y_arr = results[:,name2ind['Y']]
    Z_arr = results[:,name2ind['Z']]
    Cg_arr = results[:,name2ind['Charge']]

    #-500 is position of the MCP front on the ion side (-500)
    d2_accum = 0
    for i in range(3):
        assert Cg_arr[12+2*i+1]>0

        if ((-500.-X_arr[18+2*i+1]) != 0) or ((-500.-X_arr[12+2
                                        *i+1]) != 0):
            return last_metric*1e10

        d2_accum += ((Y_arr[12+2*i+1] - Y_arr[18+2*i+1])**2 + (
                                        Z_arr[12+2*i+1] - Z_arr
                                        [18+2*i+1])**2)
    return d2_accum

names = ["Ion N","Events","TOF","Mass","Charge","X","Y","Z","
                                    Azm","Elv","Vx","Vy","Vz","KE"]
name2ind = {}
for i, name in enumerate(names):
    name2ind[name] = i
```

```
# initial voltages on the electrodes (for the electron side)
u1=-1795;u2=-2420;u3=-2725;u4=-2835;u5=-4000;u6=-4600;
u7=-2300;u8=5;u9=425;u10=-300;u11=-400;u12=420;u13=320;
u14=1810;u15=200;u16=2200;u17=5000

# create a dictionary for electron voltages
u_dicts = {'1':u1,'2':u2,'3':u3,'4':u4,'5':u5,'6':u6,'7':u7,
           '8':u8,'9':u9,'10':u10,'11':u11,'12':u12,'13':u13,
           '14':u14,'15':u15,'16':u16, '17':u17}
```

```
#connects the index with the right voltages
volt_str = ''
for k in u_dicts.keys():
    volt_str += k+'='+str(u_dicts[k])+','
volt_str = volt_str[:-1]
```

```
# initial voltages on the electrodes (for the ion side)
iu1=-1795;iu2=-2420;iu3=-2725;iu4=-2835;iu5=-4000;iu6=-4600;
iu7=-2300;iu8=5;iu9=425;iu10=-300; iu11=-400; iu12=420;
iu13=320; iu14=1810; iu15=200; iu16=2200; iu17=5000

# create a dictionary for the ion voltages
iu_dicts = {'1:u1,'2':iu2,'3':iu3,'4':iu4,'5':iu5,'6':iu6,'7':
            iu7,'8':iu8,'9':iu9,'10':iu10,'11':iu11,'12':iu12,
            '13':iu13,'14':iu14,'15':iu1,'16':iu16,'17':iu17}
```

```
#low volts to high, i.e., excluding the detector voltages
#contains voltage for electrodes and flight tubes
order_dicts = {0:'5',1:'4',2:'3',3:'2',4:'1',5:'11',6:'12',7:'
                                13',8:'14',9:'6'}
```

```
#Voltage optimization range for each electrode
pbounds = {}
init_volts = np.zeros((10,))
dvolts = 500
for i in order_dicts.keys():
    init_volts[i] = iu_dicts[order_dicts[i]]
    pbounds['u'+order_dicts[i]] = (-dvolts+iu_dicts[order_dicts
                                    [i]], dvolts+iu_dicts[
                                    order_dicts[i]])
```

```
#exemplary output
{'u5': (-4500, -3500),
 'u4': (-3335, -2335),
 'u3': (-3225, -2225),
 'u2': (-2920, -1920),
 'u1': (-2295, -1295),
 'u11': (-900, 100),
 'u12': (-80, 920),
 'u13': (-180, 820),
 'u14': (1310, 2310),
 'u6': (-5100, -4100)}
```

```
#SIMION files to optimize/modify in the working path
PA_file = wkpath+r'/long_open_plane.PA0'
fly_file = wkpath+r'/dVMI_plane_ligroup.fly2'
output_file = wkpath+r'/out_opt_dVMI_plane.dat'
iob_file = wkpath+r'/dVMI_plane.iob'
```

```
def Metric(sol):

    #fixed detector voltages for ion side
    u7=-2300;u8=5;u9=425

    #fixed detector voltages for electron side
    u15=200;u16=2200;u17=5000

    ux = sol.get_x()

    u = []
    for ui in ux:
        u.append(ui)

    u5=u[0];u4=u[1];u3=u[2];
    u2=u[3];u1=u[4];u11=u[5];
    u12=u[6];u13=u[7];u14=u[8];u6=u[9]

    u_dicts = {'1':u1, '2':u2,'3':u3,'4':u4,'5':u5,'6':u6,
               '7':u7,'8':u8,'9':u9,'10':u10,'11':u11,'12':u12,
```

```
                '13':u13,'14':u14,'15':u15,'16':u16, '17':u17}

    if os.path.isfile(output_file):
        os.remove(output_file)
    volt_str = ''

    for k in u_dicts.keys():
        volt_str += k+'='+str(u_dicts[k])+','
    volt_str = volt_str[:-1]

    #running SIMION via the python notebook
    subprocess.call(r' wine simion.exe --nogui fastadj '+
                    PA_file+' '+volt_str, shell=True)

    subprocess.call(r'wine simion.exe --nogui fly --particles='
                    +fly_file+' --recording-enable=1 --
                    recording-output='+output_file+' --restore-
                    potentials=0 --retain-trajectories=0 '+
                    iob_file, shell=True)

    results = np.loadtxt(output_file,skiprows = 12,max_rows=24,
                         delimiter=',')

    metric = VMI_metric_ion(results) + VMI_metric_ele(results)

    return metric
```

```
#define starting voltages -> here we place later optimized
#voltages and run this cell and all cells below again
init_volts = np.array([-3655., -2609., -1864., -1422., -1038.,
                                -269.,  499., 515., 2310.,  -
                                4852.])
```

```
#convert pbounds (dictionary) into the list bounds
bounds = []
for k in pbounds.keys():
    bounds.append([pbounds[k][0],pbounds[k][1]])
```

```
dim = len(init_volts)
sol0 = Solution(x=init_volts)
param = Parameter(budget=5000,intermediate_result=True,
                  intermediate_freq=10,init_samples=[sol0])
obj = Objective(Metric, Dimension(dim, bounds, [True]*dim))
```

```
#start optimization and print optimized values
start = time.time()
solution = Opt.min(obj, param)
end = time.time()
print(end-start)
```

```
#exemplary output
[zoopt] init solution 0, value: 10000000000026.664
[zoopt] expected remaining running time: 01:04:18
[zoopt] budget 30, fx result: 122.12497366130002
```

```
[zoopt] x: [-3606.683873846373, -2700.0297954476773,
            -2671.333154391642, -2769.554462355277,
            -2189.713231485545, -274.52423443046393,
            847.6983469034087, 180.4855803861103,
            1853.2269142042142, -4292.795363309067]
[zoopt] budget 40, fx result: 72.22376708129998
[zoopt] x: [-3654.11814230896, -2620.92131869707,
            -2671.333154391642, -2769.554462355277,
            -2189.713231485545, -447.9348375084487,
            837.6636109686216, 180.4855803861103,
            1853.2269142042142, -4292.795363309067]

#[...]

[zoopt] budget 5000, fx result: 3.094821706208993
[zoopt] x: [-3690.07169485122, -2740.8587457865465,
            -2646.021995296985, -2764.368712973955,
            -2189.382485831536, -899.0624046915639,
            380.4660694025442, -178.98285364316177,
            2309.9999997121618, -4107.81641209284]
            # example for first optimization results
```

```
# The optimized values are then the new init_volts:
Next steps
0. enter new voltages manually in SIMION (check improvement)
1. redefine init_volts
2. call SIMION again
3. get again optimized results
4. repeat step 0 - 3 until you are satisfied with the result
```

References

1. Planck, M. Ueber irreversible Strahlungsvorgänge. *Annalen der Physik* **311,** 69–122 (1901).
2. Feymann, R. The Character of Physical Law (Chapter 6). *The M.I.T Press* (1965).
3. Fermi, E. In A Dictionary of Scientific Quotations by Alan L. Mackay. *CRC Press* (1991).
4. Born, M. & Einstein, A. Book: Albert Einstein and Max Born: Letters from 1916 to 1955, page. 34. *Rowohlt, Reinbeck by Hamburg* (1969).
5. Bohr, N. I On the constitution of atoms and molecules. *The London, Edinburgh, and Dublin Philosophical Magazine and Journal of Science* **26,** 1–25 (1913).
6. Thomson Baron Kelvin, W. Baltimore Lectures on Molecular Dynamics and the Wave Theory of Light. *Cambridge University Press. Cambridge Library Collection - Physical Sciences* (2010).
7. CRC 1319 ELCH webpage. Accessed August 8, 2023 https://www.uni-kassel.de/forschung/sfb/sfb-1319-elch (n.d.).
8. DFG project, CRC 1319 ELCH. Accessed August 8, 2023 https://gepris.dfg.de/gepris/projekt/328961117?context=projekt&task=showDetail&id=328961117& (n.d.).
9. A4 project within CRC 1319 ELCH. Accessed August 8, 2023 https://www.uni-kassel.de/fb10/en/institute/physics/research-groups/funktionale-duenne-schichten-physik-mit-synchrotronstrahlung/welcome-page (n.d.).
10. Demtröder, W. Book Experimentalphysik 3: Atome, Moleküle und Festkörper. *Springer-Verlag* (2016).
11. Caldwell, J. & Wainer, I. W. Stereochemistry: definitions and a note on nomenclature. *Human Psychopharmacology: Clinical and Experimental* **16,** S105–S107 (2001).
12. Cahn, R. S., Ingold, C. & Prelog, V. Spezifikation der molekularen Chiralität. *Angewandte Chemie* **78,** 413–447 (1966).

13. Fischer, E. Einfluss der Configuration auf die Wirkung der Enzyme. *Berichte der deutschen chemischen Gesellschaft* **27,** 2985–2993 (1894).

14. Bonner, W. The origin and amplification of biomolecular chirality. *Origins Life Evol Biosphere* **21,** 59–111 (1991).

15. Quack, M. Die Spiegelsymmetrie des Raumes und die Chiralität in Chemie, Physik, und in der biologischen Evolution. *Nova Acta Leopoldina* **127,** 119–166 (2016).

16. Ritchie, B. Theory of the angular distribution of photoelectrons ejected from optically active molecules and molecular negative ions. *Phys. Rev. A* **13,** 1411–1415 (1976).

17. Walker. *Organic Chemistry I* Accessed May 1, 2023 https://chem.libretexts.org/Courses/SUNY_Potsdam/Book:_Organic_Chemistry_I_(Walker)/04:_Stereochemistry/4.01:_Chirality. (n.d.).

18. Thompson, A. *et al.* X-ray Data Booklet. *Lawrence Berkeley National Laboratory, University of California Berkeley* (2009).

19. Einstein, A. Über einen die Erzeugung und Verwandlung des Lichtes betreffenden heuristischen Gesichtspunkt. *Annalen der Physik* **322,** 132–148 (1905).

20. Krause, M. O. Atomic radiative and radiationless yields for K and L shells. *Journal of Physical and Chemical Reference Data* **8,** 307–327 (1979).

21. Krause, M. O. & Oliver, J. H. Natural widths of atomic K and L levels, K X-ray lines and several KLL Auger lines. *Journal of Physical and Chemical Reference Data* **8,** 329–338 (1979).

22. Bearden, J. A. X-ray wavelengths. *Reviews of Modern Physics* **39,** 78 (1967).

23. Son, S.-K. & Santra, R. Monte Carlo calculation of ion, electron, and photon spectra of xenon atoms in x-ray free-electron laser pulses. *Physical Review A* **85,** 063415 (2012).

24. Eberly, J. H., Javanainen, J. & Rzażewski, K. Above-threshold ionization. *Physics Reports* **204,** 331–383 (1991).

25. Kochur, A. G. & Popov, V. A. Shake up and shake off probabilities for L-, M-, and N-electrons in atoms with Z=3 to 60. *Radiation Physics and Chemistry* **75,** 1525–1528 (2006).

26. Becker, U. & Shirley, D. A. Book: VUV and Soft X-Ray Photoionization. *Springer Science & Business Media* (1996).

27. Belford, R. *General Chemistry I* Accessed July 7, 2023 https://chem.libretexts.org/Courses/University_of_Arkansas_Little_Rock/Chem_1402:_General_Chemistry_1_(Belford)/Text/6:_The_Structure_of_Atoms/6.6:_The_Shapes_of_Atomic_Orbitals. (n.d.).

28. Haas, K. *Inorganic Chemistry* Accessed July 7, 2023 https://chem.libretexts.org/Bookshelves/Inorganic_Chemistry/Inorganic_Chemistry_(LibreTexts)/05%3A_Molecular_Orbitals/5.02%3A_Homonuclear_Diatomic_Molecules/5.2.01%3A_Molecular_Orbitals. (n.d.).
29. Mendeleev, D. On the relationship of the properties of the elements to their atomic weights. *Zeitschrift für Chemie* **12,** 405–406 (1869).
30. Law, J. & Rennie, R. Book: A Dictionary of Physics. *OUP Oxford* (2015).
31. Schrödinger, E. Quantisierung als Eigenwertproblem. *Annalen der Physik* **384,** 489–527 (1926).
32. Atkins, P. & de Paula, J. Book: Physical Chemistry (ninth edition). *Oxford university press* (2010).
33. Born, M. & Oppenheimer, R. Zur Quantentheorie der Molekeln. *Annalen der Physik* **389,** 457–484 (1927).
34. Mayer-Kuckuk, T. Book: Atomphysik: Eine Einführung (fifth edition). *Springer-Verlag* (1997).
35. Private communication with Zheng Li & Ludger Inhestern (2020).
36. Lennard-Jones, J. E. The electronic structure of some diatomic molecules. *Transactions of the Faraday Society* **25,** 668–686 (1929).
37. Mulliken, R. S. Spectroscopy, Molecular Orbitals, and Chemical Bonding. *Science* **157,** 13–24 (1967).
38. Kutzelnigg, W. Friedrich Hund and Chemistry. *Angewandte Chemie International Edition in English* **35,** 572–586 (1996).
39. Weinhold, F. & Landis, C. R. Valency and bonding: a natural bond orbital donor-acceptor perspective. *Cambridge University Press* (2005).
40. Park, B. S. & Stetten, D. A Principle Written in Diagrams: The Aufbau Principle for Molecules and Its Visual Representations, 1927–1932. *Springer Netherlands* (ed Klein, U.) 179–198 (2001).
41. Hartree, D. R. The Wave Mechanics of an Atom with a Non-Coulomb Central Field. Part II. Some Results and Discussion. *Mathematical Proceedings of the Cambridge Philosophical Society* **24,** 111–132 (1928).
42. Slater, J. C. The self consistent field and the structure of atoms. *Physical Review* **32,** 339 (1928).
43. Hohenberg, P. & Kohn, W. Inhomogeneous Electron Gas. *Phys. Rev.* **136,** B864–B871 (1964).
44. Burke, K. & Wagner, L. O. DFT in a nutshell. *International Journal of Quantum Chemistry* **113,** 96–101 (2013).
45. Bagayoko, D. Understanding density functional theory (DFT) and completing it in practice. *AIP Advances* **4,** 127104 (2014).

46. Cooper, J. & Zare, R. N. Angular Distribution of Photoelectrons. *The Journal of Chemical Physics* **48,** 942–943 (1968).

47. Laplanche, G, Jaouen, M & Rachman, A. Angular distributions and polarisation phenomena in non-resonant multiphoton ionisation of alkali-metal atoms. I. Formal theory. *Journal of Physics B: Atomic and Molecular Physics* **19,** 79 (1986).

48. Manson, S. T. & Starace, A. F. Photoelectron angular distributions: energy dependence for *s* subshells. *Rev. Mod. Phys.* **54,** 389–405 (1982).

49. Powis, I. Photoelectron circular dichroism of the randomly oriented chiral molecules glyceraldehyde and lactic acid. *The Journal of Chemical Physics* **112,** 301–310 (2000).

50. Cherepkov, N. Theory of spin polarisation phenomena in molecular photoionisation processes. *Journal of Physics B: Atomic and Molecular Physics* **14,** 2165 (1981).

51. Cherepkov, N. Circular dichroism of molecules in the continuous absorption region. *Chemical Physics Letters* **87,** 344–348 (1982).

52. Hemmers, O. *et al.* Dramatic Nondipole Effects in Low-Energy Photoionization: Experimental and Theoretical Study of Xe 5*s*. *Phys. Rev. Lett.* **91,** 053002 (2003).

53. Hemmers, O. *et al.* Nondipole Effects in the Photoionization of Xe $4d_{5/2}$ and $4d_{3/2}$: Evidence for Quadrupole Satellites. *Phys. Rev. Lett.* **93,** 113001 (2004).

54. Wang, M.-X., Chen, S.-G., Liang, H. & Peng, L.-Y. Review on nondipole effects in ionization and harmonic generation of atoms and molecules. *Chinese Physics B* **29,** 013302 (2020).

55. Ilchen, M. *et al.* Symmetry breakdown of electron emission in extreme ultraviolet photoionization of argon. *Nature Communications* **9,** 4659 (2018).

56. McNeil, B. W. J. & Thompson, N. R. X-ray free-electron lasers. *Nature Photonics* **4,** 814–821 (2010).

57. Pellegrini, C., Marinelli, A. & Reiche, S. The physics of x-ray free-electron lasers. *Rev. Mod. Phys.* **88,** 015006 (2016).

58. Madey, J. M. Stimulated emission of bremsstrahlung in a periodic magnetic field. *Journal of Applied Physics* **42,** 1906–1913 (1971).

59. Schmüser, P., Dohlus, M. & Rossbach, J. Book: Ultraviolet and soft X-ray free-electron lasers: introduction to physical principles, experimental results, technological challenges. *Springer Science & Business Media* **229** (2009).

60. Allaria, E *et al.* Highly coherent and stable pulses from the FERMI seeded free-electron laser in the extreme ultraviolet. *Nature Photonics* **6,** 699–704 (2012).

61. Ackermann, W. *et al.* Operation of a free-electron laser from the extreme ultraviolet to the water window. *Nature Photonics* **1,** 336–342 (2007).

62. Feldhaus, J. FLASH—the first soft x-ray free electron laser (FEL) user facility. *Journal of Physics B: Atomic, Molecular and Optical Physics* **43,** 194002 (2010).

63. Altarelli, M., Brinkmann, R. & Chergui, M. The European X-ray free-electron laser. *Technical design report* (2007).

64. Altarelli, M. The European X-ray free-electron laser facility in Hamburg. *Nuclear Instruments and Methods in Physics Research Section B: Beam Interactions with Materials and Atoms* **269,** 2845–2849 (2011).

65. Robinson, I., Gruebel, G. & Mochrie, S. Focus on X-ray Beams with High Coherence. *New Journal of Physics* **12,** 035002 (2010).

66. Stohr, J. Linac coherent light source II (LCLS-II) conceptual design report. *SLAC National Accelerator Lab., Menlo Park, CA (United States)* (2011).

67. Clarke, J. A. Book: The science and technology of undulators and wigglers. *OUP Oxford* **4** (2004).

68. Levichev, E. & Vinokurov, N. Undulators and other insertion devices. *Reviews of Accelerator Science and Technology* **3,** 203–220 (2010).

69. Saldin, E., Schneidmiller, E. & Yurkov, M. V. Book: The physics of free electron lasers. *Springer Science & Business Media* (2000).

70. Prat, E. Synchrotron light sources and X-ray free-electron-lasers. *arXiv preprint arXiv:2107.09131* (2021).

71. Geloni, G., Huang, Z. & Pellegrini, C. Book: The Physics and Status of X-ray Free-electron Lasers, Chapter: X-Ray Free Electron Lasers: Applications in Materials, Chemistry and Biology. *The Royal Society of Chemistry* (2017).

72. Hwu, Y. & Margaritondo, G. Synchrotron radiation and X-ray free-electron lasers (X-FELs) explained to all users, active and potential. *Journal of Synchrotron Radiation* **28,** 1014–1029 (2021).

73. Kang, H.-S. & Loos, H. X-ray free electron laser tuning for variable-gap undulators. *Physical Review Accelerators and Beams* **22,** 060703 (2019).

74. Siegman, A. E. Book: Lasers. *University science books* (1986).

75. Bonifacio, R, De Salvo, L, Pierini, P, Piovella, N & Pellegrini, C. Spectrum, temporal structure, and fluctuations in a high-gain free-electron laser starting from noise. *Physical review letters* **73,** 70 (1994).

76. Huang, N., Deng, H., Liu, B., Wang, D. & Zhao, Z. Features and futures of X-ray free-electron lasers. *The Innovation* **2,** 100097 (2021).

77. Tiedtke, K *et al.* The soft x-ray free-electron laser FLASH at DESY: beamlines, diagnostics and end-stations. *New journal of physics* **11,** 023029 (2009).

78. Tschentscher, T. *et al.* Photon beam transport and scientific instruments at the European XFEL. *Applied Sciences* **7,** 592 (2017).

79. Moeller, S. *et al.* Photon beamlines and diagnostics at LCLS. *Nuclear Instruments and Methods in Physics Research Section A: Accelerators, Spectrometers, Detectors and Associated Equipment* **635,** S6–S11 (2011).

80. Tiedtke, K. *et al.* Gas detectors for x-ray lasers. *Journal of Applied Physics* **103** (2008).

81. Sorokin, A. A. *et al.* An X-ray gas monitor for free-electron lasers. *Journal of Synchrotron Radiation* **26,** 1092–1100 (2019).

82. Viti, M. *et al.* The bunch arrival time monitor at FLASH and European XFEL. *Proc. ICALEPCS'17,* 701–705 (2017).

83. Löhl, F. *et al.* Electron Bunch Timing with Femtosecond Precision in a Superconducting Free-Electron Laser. *Phys. Rev. Lett.* **104,** 144801 (2010).

84. Schulz, S. *et al.* Few-femtosecond facility-wide synchronization of the European XFEL. *Proceedings of the 39 the International Free-Electron Laser Conference (Hamburg),* 319–321 (2019).

85. Redlin, H. *et al.* The FLASH pump–probe laser system: Setup, characterization and optical beamlines. *Nuclear Instruments and Methods in Physics Research Section A: Accelerators, Spectrometers, Detectors and Associated Equipment* **635,** S88–S93 (2011).

86. Sinn, H. *et al.* The SASE1 X-ray beam transport system. *Journal of synchrotron radiation* **26,** 692–699 (2019).

87. Hahn, U. & Tiedtke, K. The gas attenuator of FLASH at DESY. *AIP Conference Proceedings* **879,** 276–282 (2007).

88. Rumiz, L *et al.* The gas attenuator vacuum system of FERMI@ Elettra. *2nd International Particle Accelerator Conference (IPAC),* 1530 (2011).

89. Martins, M *et al.* Monochromator beamline for FLASH. *Review of scientific instruments* **77,** 115108 (2006).

90. Dziarzhytski, S. *et al.* Microfocusing at the PG1 beamline at FLASH. *Journal of synchrotron radiation* **23,** 123–131 (2016).

91. Siewert, F *et al.* Sub-nm accuracy metrology for ultra-precise reflective X-ray optics. *Nuclear Instruments and Methods in Physics Research Section A: Accelerators, Spectrometers, Detectors and Associated Equipment* **635,** S52–S57 (2011).

92. Vannoni, M., Martín, I. F., Music, V. & Sinn, H. Calibration and optimization of an x-ray bendable mirror using displacement-measuring sensors. *Optics express* **24,** 17292–17302 (2016).

93. Vannoni, M. *et al.* Metrology characterization of ultraprecise bendable mirrors for the European XFEL: from offsite calibration to installation and commissioning. *Journal of synchrotron radiation* **26,** 1110–1114 (2019).

94. Wurth, W. FLASH: running two FELs in parallel. *Synchrotron Radiation News* **30,** 3–6 (2017).

95. Vannoni, M & Freijo-Martin, I. Installation and commissioning of the European XFEL beam transport in the first two beamlines from a metrology point of view. *Review of Scientific Instruments* **90,** 021701 (2019).

96. Schmidt, T. & Calvi, M. APPLE X Undulator for the SwissFEL Soft X-ray Beamline Athos. *Synchrotron Radiation News* **31,** 35–40 (2018).

97. Liang, X., Calvi, M., Kittel, C., Schmidt, T. J. & Sammut, N. Advanced operational models of the apple x undulator. *FEL 2019: 39th Free Electron Laser Conf.* (2019).

98. Yakopov, M. *et al.* Characterization of helical APPLE X undulators with 90 mm period for the European XFEL. *Journal of Physics: Conference Series* **2380,** 012019 (2022).

99. Li, P., Wei, T., Li, Y. & Pflueger, J. Magnetic design of an Apple-X afterburner for the SASE3 undulator of the European XFEL. *Nuclear Instruments and Methods in Physics Research Section A: Accelerators, Spectrometers, Detectors and Associated Equipment* **870,** 103–109 (2017).

100. Calvi, M., Camenzuli, C, Prat, E & Schmidt, T. Transverse gradient in Apple-type undulators. *Journal of synchrotron radiation* **24,** 600–608 (2017).

101. Allaria, E. *et al.* Control of the Polarization of a Vacuum-Ultraviolet, High-Gain, Free-Electron Laser. *Phys. Rev. X* **4,** 041040 (2014).

102. Tischer, M *et al.* Development of an APPLE-III undulator for FLASH-2. *Journal of Physics: Conference Series* **2380,** 012017 (2022).

103. Von Korff Schmising, C. *et al.* Generating circularly polarized radiation in the extreme ultraviolet spectral range at the free-electron laser FLASH. *Review of Scientific Instruments* **88,** 053903 (2017).

104. Hartmann, G *et al.* Circular dichroism measurements at an x-ray free-electron laser with polarization control. *Review of scientific instruments* **87,** 083113 (2016).

105. Grychtol, P. *et al.* Timing and X-ray pulse characterization at the Small Quantum Systems instrument of the European X-ray Free Electron Laser. *Optics express* **29,** 37429–37442 (2021).

106. Allum, F. *et al.* A localized view on molecular dissociation via electron-ion partial covariance. *Communications chemistry* **5,** 42 (2022).

107. Schulz, S. *et al.* Femtosecond all-optical synchronization of an X-ray free-electron laser. *Nature communications* **6,** 5938 (2015).

108. Sydlo, C., Zummack, F, Müller, J, Felber, M & Lamb, T. Femtosecond optical synchronization system for the European XFEL. *Proceedings of IPAC2017,* 3969–3971 (2017).

109. Lamb, T. *et al.* Large-scale optical synchronization system of the European XFEL with femtosecond precision. *Proc. IPAC'19,* 3835–3838 (2019).

110. Mazza, T. *et al.* Mapping Resonance Structures in Transient Core-Ionized Atoms. *Physical Review X* **10,** 041056 (2020).

111. Kastirke, G. *et al.* Double Core-Hole Generation in O_2 Molecules Using an X-Ray Free-Electron Laser: Molecular-Frame Photoelectron Angular Distributions. *Physical review letters* **125,** 163201 (2020).

112. Kastirke, G. *et al.* Photoelectron Diffraction Imaging of a Molecular Breakup Using an X-Ray Free-Electron Laser. *Physical Review X* **10,** 021052 (2020).

113. Kastirke, G. *et al.* Investigating charge-up and fragmentation dynamics of oxygen molecules after interaction with strong X-ray free-electron laser pulses. *Physical chemistry chemical physics : PCCP* **24,** 27121–27127 (2022).

114. Jahnke, T. *et al.* Inner-Shell-Ionization-Induced Femtosecond Structural Dynamics of Water Molecules Imaged at an X-Ray Free-Electron Laser. *Physical Review X* **11,** 041044 (2021).

115. Freund, H. & O'Shea, P. Two-color operation in high-gain free-electron lasers. *Physical Review Letters* **84,** 2861 (2000).

116. Schneidmiller, E. *et al.* Two-color operation of a soft x-ray FEL with alternation of undulator tunes. *Applied Sciences* **13,** 67 (2022).

117. Lutman, A. *et al.* Experimental demonstration of femtosecond two-color x-ray free-electron lasers. *Physical review letters* **110,** 134801 (2013).

118. Ilchen, M. *et al.* Site-specific interrogation of an ionic chiral fragment during photolysis using an X-ray free-electron laser. *Communications Chemistry* **4,** 119 (2021).

119. Rouxel, J. R. & Mukamel, S. Molecular chirality and its monitoring by ultrafast x-ray pulses. *Chemical Reviews* **122,** 16802–16838 (2022).

120. Zehnacker, A. Book: Chiral recognition in the gas phase. *CRC Press* (2010).

121. Ordonez, A. F. & Smirnova, O. Generalized perspective on chiral measurements without magnetic interactions. *Phys. Rev. A* **98,** 063428 (2018).

122. Powis, I. Photoelectron circular dichroism of the randomly oriented chiral molecules glyceraldehyde and lactic acid. *The Journal of Chemical Physics* **112,** 301–310 (2000).

123. Böwering, N *et al.* Asymmetry in photoelectron emission from chiral molecules induced by circularly polarized light. *Physical review letters* **86,** 1187 (2001).

124. Ferré, A *et al.* A table-top ultrashort light source in the extreme ultraviolet for circular dichroism experiments. *Nature Photonics* **9,** 93–98 (2015).

125. Turchini, S. *et al.* Conformational Sensitivity in Photoelectron Circular Dichroism of 3-Methylcyclopentanone. *ChemPhysChem* **14,** 1723–1732 (2013).

126. Turchini, S. Conformational effects in photoelectron circular dichroism. *Journal of Physics: Condensed Matter* **29,** 503001 (2017).

127. Blanchet, V. *et al.* Ultrafast relaxation investigated by photoelectron circular dichroism: an isomeric comparison of camphor and fenchone. *Physical Chemistry Chemical Physics* **23,** 25612–25628 (2021).

128. Beaulieu, S. *et al.* Probing ultrafast dynamics of chiral molecules using time-resolved photoelectron circular dichroism. *Faraday discussions* **194,** 325–348 (2016).

129. Hadidi, R., Bozanic, D. K., Garcia, G. A. & Nahon, L. Electron asymmetries in the photoionization of chiral molecules: possible astrophysical implications. *Advances in Physics: X* **3,** 1477530 (2018).

130. Nahon, L., Garcia, G. A. & Powis, I. Valence shell one-photon photoelectron circular dichroism in chiral systems. *Journal of Electron Spectroscopy and Related Phenomena* **204,** 322–334 (2015).

131. Ilchen, M *et al.* Emitter-site-selective photoelectron circular dichroism of trifluoromethyloxirane. *Physical Review A* **95,** 053423 (2017).

132. Hergenhahn, U. *et al.* Photoelectron circular dichroism in core level ionization of randomly oriented pure enantiomers of the chiral molecule camphor. *The Journal of chemical physics* **120,** 4553–4556 (2004).

133. Lutman, A. A. *et al.* Polarization control in an X-ray free-electron laser. *Nature photonics* **10,** 468–472 (2016).

134. Decking, W *et al.* A MHz-repetition-rate hard X-ray free-electron laser driven by a superconducting linear accelerator. *Nature photonics* **14,** 391–397 (2020).

135. Music, V. Bachelor's Thesis: Optimisation and Characterisation of a Mechanical Bender for X-ray Mirrors. *University of Hamburg* (2015).

136. Music, V. Master's Thesis: Characterisation of X-ray Optics at the European XFEL SASE1 Beamline. *University of Hamburg* (2018).

137. Meyer, M. *et al.* The Small Quantum System (SQS) Instrument at European XFEL: Results of commissioning and first experiments. *Journal of Physics: Conference Series* **1412,** 112005 (2020).

138. Mazza, T. *et al.* The beam transport system for the Small Quantum Systems instrument at the European XFEL: optical layout and first commissioning results. *Journal of Synchrotron Radiation* **30,** 457–467 (2023).

139. Baumann, T. *et al.* Harmonic radiation contribution and X-ray transmission at the Small Quantum Systems instrument of European XFEL. *J. Synchrotron Rad.* **30,** 662–670 (2023).

140. De Fanis, A. *et al.* High-resolution electron time-of-flight spectrometers for angle-resolved measurements at the SQS Instrument at the European XFEL. *Journal of synchrotron radiation* **29,** 755–764 (2022).

141. Li, X. *et al.* Coulomb explosion imaging of small polyatomic molecules with ultrashort x-ray pulses. *Physical Review Research* **4,** 013029 (2022).

142. Li, X. *et al.* Resonance-enhanced x-ray multiple ionization of a polyatomic molecule. *Physical Review A* **105,** 053102 (2022).

143. Boll, R. *et al.* X-ray multiphoton-induced Coulomb explosion images complex single molecules. *Nature Physics* **18,** 423–428 (2022).

144. Eichmann, U. *et al.* Photon-recoil imaging: Expanding the view of nonlinear x-ray physics. *Science* **369,** 1630–1633 (2020).

145. Heisen, B. C. *et al.* Karabo: An Integrated Software Framework Combining Control, Data Management, and Scientific Computing Tasks. *Proceedings of ICALEPCS2013,* 1465–1468 (2013).

146. Rouxel, J. R., Kowalewski, M. & Mukamel, S. Photoinduced molecular chirality probed by ultrafast resonant X-ray spectroscopy. *Structural Dynamics* **4,** 044006 (2017).

147. Hartmann, N. *et al.* Attosecond time–energy structure of X-ray free-electron laser pulses. *Nat. Photonics* **12,** 215–220 (2018).

148. Duris, J. *et al.* Tunable isolated attosecond X-ray pulses with gigawatt peak power from a free-electron laser. *Nat. Photonics* **14,** 30–36 (2020).

149. Eppink, A. T. J. B. & Parker, D. H. Velocity map imaging of ions and electrons using electrostatic lenses: Application in photoelectron and photofragment ion imaging of molecular oxygen. *Review of Scientific Instruments* **68,** 3477–3484 (1997).

150. Friedrich, B. & Schmidt-Böcking, H. Book: Molecular Beams in Physics and Chemistry: From Otto Stern's Pioneering Exploits to Present-Day Feats. *Springer Nature* (2021).

151. Eppink, A. T. J. B. & Parker, D. H. Energy partitioning following photodissociation of methyl iodide in the A band: A velocity mapping study. *The Journal of Chemical Physics* **110,** 832–844 (1999).

152. Vredenborg, A., Roeterdink, W. G. & Janssen, M. H. M. A photoelectron-photoion coincidence imaging apparatus for femtosecond time-resolved molecular dynamics with electron time-of-flight resolution of sigma=18 ps and energy resolution Delta E/E=3.5%. *The Review of scientific instruments* **79,** 063108 (2008).

153. Hosaka, K. *et al.* Coincidence Velocity Imaging Apparatus for Study of Angular Correlations between Photoelectrons and Photofragments. *Japanese Journal of Applied Physics* **45,** 1841–1849 (2006).

154. Lebech, M., Houver, J. C. & Dowek, D. Ion–electron velocity vector correlations in dissociative photoionization of simple molecules using electrostatic lenses. *Review of Scientific Instruments* **73,** 1866–1874 (2002).

155. Wiley, W. C. & McLaren, I. H. Time–of–Flight Mass Spectrometer with Improved Resolution. *Review of Scientific Instruments* **26,** 1150–1157 (1955).

156. Shepp, L. A. & Logan, B. F. The Fourier reconstruction of a head section. *IEEE Transactions on Nuclear Science* **21,** 21–43 (1974).

157. Hickstein, D. D., Gibson, S. T., Yurchak, R., Das, D. D. & Ryazanov, M. A direct comparison of high-speed methods for the numerical Abel transform. *Review of Scientific Instruments* **90,** 065115 (2019).

158. Champenois, E. G. PhD Thesis: Resolving Non-Adiabatic Dynamics in Small Molecules with Few-Femtosecond Sensitivity. *University of California, Berkeley* (2017).

159. Ryazanov, M. PhD Thesis: Development and implementation of methods for sliced velocity map imaging. Studies of overtone-induced dissociation and isomerization dynamics of hydroxymethyl radical (CH_2OH and CD_2OH). *University of Southern California* (2012).

160. Jitschin, W. *et al.* Book: Wutz Handbuch Vakuumtechnik: Theorie und Praxis. *Springer-Verlag* (2013).

161. Beamdynamics skimmer webpage. Accessed May 19, 2023 https://www.beamdynamicsinc.com/molecular-beam-skimmers (n.d.).

162. Osipov, T. *et al.* The LAMP instrument at the Linac Coherent Light Source free-electron laser. *Review of Scientific Instruments* **89,** 035112 (2018).

163. Strüder, L. *et al.* Large-format, high-speed, X-ray pnCCDs combined with electron and ion imaging spectrometers in a multipurpose chamber for experiments at 4th generation light sources. *Nuclear Instruments and Methods in Physics Research Section A: Accelerators, Spectrometers, Detectors and Associated Equipment* **614,** 483–496 (2010).

164. Ali, I. *et al.* Multi-hit detector system for complete momentum balance in spectroscopy in molecular fragmentation processes. *Nuclear Instruments and Methods in Physics Research Section B: Beam Interactions with Materials and Atoms* **149,** 490–500 (1999).

165. Scientific Instrument Services, Inc. SIMION Simulation Software Package. Version 8.1 (2011).

166. Gottwald, A. *et al.* Current capabilities at the Metrology Light Source. *Metrologia* **49,** 146 (2012).

167. Gottwald, A., Kaser, H. & Kolbe, M. The U125 insertion device beamline at the Metrology Light Source. *J. Synchrotron Rad.* **26,** 535–542 (2019).

168. O_2 Cross Section NIST webpage. Accessed July 22, 2023 https://www.physics.nist.gov/cgi-bin/Ionization/table.pl?ionization=O2 (n.d.).

169. Lin, P. & Lucchese, R. R. Theoretical studies of cross sections and photoelectron angular distributions in the valence photoionization of molecular oxygen. *The Journal of Chemical Physics* **116,** 8863–8875 (2002).

170. PubChem webpage. Accessed August 9, 2023 https://pubchem.ncbi.nlm.nih.gov/compound/1-Iodo-2-methylbutane#section=3D-Conformer (n.d.).

171. Amini, K. *et al.* Photodissociation of aligned CH_3I and $C_6H_3F_2I$ molecules probed with time-resolved Coulomb explosion imaging by site-selective extreme ultraviolet ionization. *Structural Dynamics* **5,** 014301 (2018).

172. Boll, R. *et al.* Charge transfer in dissociating iodomethane and fluoromethane molecules ionized by intense femtosecond X-ray pulses. *Structural Dynamics* **3,** 043207 (2016).

173. Erk, B. *et al.* Imaging charge transfer in iodomethane upon x-ray photoabsorption. *Science* **345,** 288–291 (2014).

174. Mertens, K., Gerken, N., Klumpp, S., Braune, M. & Martins, M. Soft X-ray multiphoton excitation of small iodine methane derivatives. *Journal of Modern Optics* **63,** 383–389 (2016).

175. Motomura, K. *et al.* Charge and Nuclear Dynamics Induced by Deep Inner-Shell Multiphoton Ionization of CH_3I Molecules by Intense X-ray Free-Electron Laser Pulses. *The Journal of Physical Chemistry Letters* **6,** 2944–2949 (2015).

176. Köckert, H. *et al.* UV-induced dissociation of CH_2BrI probed by intense femtosecond XUV pulses. *Journal of Physics B: Atomic, Molecular and Optical Physics* **55,** 014001 (2022).

177. Domondon, A. T. & Tong, X. M. Photoabsorption spectra of I and its ions in the 4*d* region. *Phys. Rev. A* **65,** 032718 (2002).

178. Kjeldsen, H. *et al.* Absolute photoionization cross sections of I^+ and I^{2+} in the 4*d* ionization region. *Phys. Rev. A* **62,** 020702 (2000).

179. Erk, B. *et al.* CAMP@FLASH: an end-station for imaging, electron- and ion-spectroscopy, and pump–probe experiments at the FLASH free-electron laser. *Journal of Synchrotron Radiation* **25,** 1529–1540 (2018).

180. Moulton, P. F. Spectroscopic and laser characteristics of Ti:Al2O3. *Journal of The Optical Society of America B-optical Physics* **3,** 125–133 (1986).

181. Nikogosyan, D. N. Beta barium borate (BBO). *Applied Physics A* **52,** 359–368 (1991).

182. Whitaker, B. J. Book: Imaging in molecular dynamics: technology and applications. *Cambridge university press* (2003).

183. John, J. *et al.* PImMS, a fast event-triggered monolithic pixel detector with storage of multiple timestamps. *Journal of Instrumentation* **7,** C08001 (2012).

184. Henke, B., Gullikson, E. & Davis, J. X-Ray Interactions: Photoabsorption, Scattering, Transmission, and Reflection at E = 50-30,000 eV, Z = 1-92. *Atomic Data and Nuclear Data Tables* **54,** 181–342 (1993).

185. Private communication with Benjamin Erk (September 2022).

186. Private communication with Benjamin Erk (June 2023).

187. lm fit webpage. Accessed August 10, 2023 https://lmfit.github.io/lmfit-py/intro.html (n.d.).

188. Von Korff Schmising, C. *et al.* Generating circularly polarized radiation in the extreme ultraviolet spectral range at the free-electron laser FLASH. *Review of Scientific Instruments* **88,** 053903 (2017).

189. Private communication with Rudolf Pietschnig (2020).

190. Eland, J. *et al.* Ion charge-resolved branching in decay of inner shell holes in Xe up to 1200 eV. *Journal of Physics B: Atomic, Molecular and Optical Physics* **48,** 205001 (2015).

191. Forbes, R. *et al.* Photoionization of the I 4d and valence orbitals of methyl iodide. *Journal of Physics B: Atomic, Molecular and Optical Physics* **53,** 155101 (2020).

192. Private communication with Felix Allum (2022).

193. Garcia, G. A., Nahon, L. & Powis, I. Two-dimensional charged particle image inversion using a polar basis function expansion. *Review of Scientific Instruments* **75,** 4989–4996 (2004).

194. Private communication with Ludger Inhester (2023).

195. Slater, C. S. *et al.* Covariance imaging experiments using a pixel-imaging mass-spectrometry camera. *Phys. Rev. A* **89,** 011401 (2014).

196. Frasinski, L. J. *et al.* Dynamics of Hollow Atom Formation in Intense X-Ray Pulses Probed by Partial Covariance Mapping. *Phys. Rev. Lett.* **111,** 073002 (2013).

197. Kornilov, O *et al.* Coulomb explosion of diatomic molecules in intense XUV fields mapped by partial covariance. *Journal of Physics B: Atomic, Molecular and Optical Physics* **46,** 164028 (2013).

198. Driver, T. *et al.* Two-Dimensional Partial-Covariance Mass Spectrometry of Large Molecules Based on Fragment Correlations. *Phys. Rev. X* **10,** 041004 (2020).

199. Frasinski, L. J., Codling, K. & Hatherly, P. A. Covariance Mapping: A Correlation Method Applied to Multiphoton Multiple Ionization. *Science* **246,** 1029–1031 (1989).

200. Frasinski, L. J. Covariance mapping techniques. *Journal of Physics B: Atomic, Molecular and Optical Physics* **49,** 152004 (2016).

201. Rading, L. *et al.* A Versatile Velocity Map Ion-Electron Covariance Imaging Spectrometer for High-Intensity XUV Experiments. *Applied Sciences* **8,** 998 (2018).

202. Zhaunerchyk, V., Frasinski, L. J., Eland, J. H. D. & Feifel, R. Theory and simulations of covariance mapping in multiple dimensions for data analysis in high-event-rate experiments. *Phys. Rev. A* **89,** 053418 (2014).

203. Tremblay, Larzillière, Combet-Farnoux & Morin. Photoelectron spectroscopy of atomic iodine produced by laser photodissociation. *Physical review. A, General physics* **38 7,** 3804–3807 (1988).

204. Nahon, L., Svensson, A. & Morin, P. Experimental study of the 4d ionization continuum in atomic iodine by photoelectron and photoion spectroscopy. *Phys. Rev. A* **43,** 2328–2337 (1991).

205. Braußе, F. *et al.* Time-resolved inner-shell photoelectron spectroscopy: From a bound molecule to an isolated atom. *Phys. Rev. A* **97,** 043429 (2018).

206. Private communication Xiang Li (March 2020).

Publication List

1. M. Vannoni, I. Frejo Martin, **V. Music,** & H. Sinn, *Calibration and optimization of an x-ray bendable mirror using displacement-measuring sensors*, Optics express **24**, 17292–17302 (2016).

2. H. Sinn, M. Dommach, B. Dickert, M. Di Felice, X. Dong, J. Eidam, D. Finze, I. Freijo Martín, N. Gerasimova, N. Kohlstrunk, D. La Civita, F. Meyn, **V. Music**, M. Neumann, M. Petrich, B. Rio, L. Samoylova, S. Schmidtchen, M. Stœrmer, A. Trapp, M. Vannoni, R. Villanueva and F. Yang, *The SASE1 X-ray beam transport system*, J. Synchrotron Rad. **26**, 692–699 (2019).

3. M. Vannoni, I. Freijo Martín, S. Schmidtchen, T. M. Baumann, M. Meyer and **V. Music**, *Metrology characterization of ultraprecise bendable mirrors for the European XFEL: from offsite calibration to installation and commissioning*, J. Synchrotron Rad. **26**, 1110–1114 (2019).

4. M. Ilchen, T. Mazza, T. M. Baumann, R. Boll, A. De Fanis, P. Grychtol, **V. Music**, Y. Ovcharenko, D. Rivas, N. Berrah, B Erk, E. Gryzlova, P. Johnsson, C. Küstner-Wetekam, L. Marder, M. Martins, Ch. Ott, S. Pathak, Th. Pfeifer, D. Rolles, P. Schmidt, A Grum-Grzhimailo. and M. Meyer, *X-ray spectroscopy on ultrafast-decaying core-excited atomic ions*, Journal of Physics: Conference Series **1412**, 112001 (2020).

5. M. Meyer, T. M. Baumann, A. Achner, R. Boll, A. De Fanis, P. Grychtol, M. Ilchen, T. Mazza, J. Montaño, **V. Music**, Y. Ovcharenko, N. Rennhack, D. E. Rivas, R. Wagner, P. Ziołkowski, D. Rolles, P. Walter, B. Erk, B. Keitel, E. Plönjes, K. Mann, S. Lange, B. Schäfer, J. Chalupský, T. Burian, K. Juranova, L. Vyšín, V. Hájková and L. Juha, *The Small Quantum System (SQS) Instrument at European XFEL: Results of commissioning and first experiments*, Journal of Physics: Conference Series **1412**, 112005 (2020).

6. P. Schmidt, **V. Music**, G. Hartmann, R. Boll, B. Erk, S. Bari, F. Allum, T. M. Baumann, G. Brenner, M. Brouard, M. Burt, R. Coffee, S. Dörner, A. Galler, P. Grychtol, D. Heathcote, L. Inhester, M. Kazemi, M. Larsson, J. Lee, Z. Li, A. Lutmann, B. Manschwetus, L. Marder, R. Mason, S. Moeller, T. Osipov, H. Otto, C. Passow, D. Rolles, P. Rupprecht, K. Schubert, L. Schwob, R. Thomas, C. Vallance, C. von Korff Schmising, R. Wagner, P. Walter, T. J. A. Wolf, V. Zhaunerchyk, M. Meyer, A. Ehresmann, A. Knie, Ph. V. Demekhin and M Ilchen, *Ultrafast Structural Changes in Chiral Molecules Measured with Free-Electron Lasers*, Journal of Physics: Conference Series **1412**, 112009 (2020).

7. U. Eichmann, H. Rottke, S. Meise, J.E. Rubensson, J. Söderström, M. Agåker, C. Såthe, M. Meyer, T. M. Baumann, R. Boll, A. De Fanis, P. Grychtol, M. Ilchen, T. Mazza, J. Montano, **V. Music**, Y. Ovcharenko, D. E. Rivas, S. Serkez, R. Wagner, S. Eisebitt1, *Photon-recoil imaging: Expanding the view of nonlinear x-ray physics*, Science **369**, 1630–1633 (2020).

8. G. Kastirke, M. S. Schöffler, M. Weller, J. Rist, R. Boll, N. Anders, T. M. Baumann, S. Eckart, B. Erk, A. De Fanis, K. Fehre, A. Gatton, S. Grundmann, P. Grychtol, A. Hartung, M. Hofmann, M. Ilchen, C. Janke, M. Kircher, M. Kunitski, X. Li, T. Mazza, N. Melzer, J. Montano, **V. Music**, G. Nalin, Y. Ovcharenko, A. Pier, N. Rennhack, D. E. Rivas, R. Dörner, D. Rolles, A. Rudenko, P. Schmidt, J. Siebert, N. Strenger, D. Trabert, I. Vela-Perez, R. Wagner, T. Weber, J. B. Williams, P. Ziolkowski, L. Ph. H. Schmidt, A. Czasch, K. Ueda, F. Trinter, M. Meyer, P. V. Demekhin, and T. Jahnke, *Double Core-Hole Generation in O_2 Molecules Using an X-Ray Free-Electron Laser: Molecular-Frame Photoelectron Angular Distributions*, Phys. Rev. Lett. **125**, 163201 (2020).

9. G. Kastirke, M. S. Schöffler, M. Weller, J. Rist, R. Boll, N. Anders, T. M. Baumann, S. Eckart, B. Erk, A. De Fanis, K. Fehre, A. Gatton, S. Grundmann, P. Grychtol, A. Hartung, M. Hofmann, M. Ilchen, C. Janke, M. Kircher, M. Kunitski, X. Li, T. Mazza, N. Melzer, J. Montano, **V. Music**, G. Nalin, Y. Ovcharenko, A. Pier, N. Rennhack, D. E. Rivas, R. Dörner, D. Rolles, A. Rudenko, P. Schmidt, J. Siebert, N. Strenger, D. Trabert, I. Vela-Perez, R. Wagner, T. Weber, J. B. Williams, P. Ziolkowski, L. Ph. H. Schmidt, A. Czasch, F. Trinter, M. Meyer, K. Ueda, P. V. Demekhin, and T. Jahnke, *Photoelectron Diffraction Imaging of a Molecular Breakup Using an X-Ray*

Free-Electron Laser, Phys. Rev. X **10**, 021052 (2020).

10. T. Mazza, M. Ilchen, M. D. Kiselev, E. V. Gryzlova, T. M. Baumann, R. Boll, A. De Fanis, P. Grychtol, J. Montaño, **V. Music**, Y. Ovcharenko, N. Rennhack, D. E. Rivas, Ph. Schmidt, R. Wagner, P. Ziolkowski, N. Berrah, B. Erk, P. Johnsson, C. Küstner-Wetekam, L. Marder, M. Martins, C. Ott, S. Pathak, T. Pfeifer, D. Rolles, O. Zatsarinny, A. N. Grum-Grzhimailo, and M. Meyer, *Mapping Resonance Structures in Transient Core-Ionized Atoms*, Phys. Rev. X **10**, 041056 (2020).

11. P. Grychtol, D. E. Rivas, T. M. Baumann, R. Boll, A. De Fanis, B. Erk, M. Ilchen, J. Liu, T. Mazza, J. Montano, J. Müller, V. Music, Y. Ovcharenko, N. Rennhack, A. Rouze, P. Schmidt, S. Schulz, S. Usenko, R. Wagner, P. Ziolkowski, H. Schlarb, J. Grünert, N. Kabachnik and M. Meyer, *Timing and X-ray pulse characterization at the Small Quantum Systems instrument of the European X-ray Free Electron Laser*, Optics Express **Vol. 29, No. 23**, 37429-37442 (2021).

12. M. Ilchen, P. Schmidt, N. M. Novikovskiy, G. Hartmann, P. Rupprecht, R. N. Coffee, A. Ehresmann, A. Galler, N. Hartmann, W. Helml, Z. Huang, L. Inhester, A. A. Lutman, J. P. MacArthur, T. Maxwell, M. Meyer, **V. Music**, H.-D. Nuhn, T. Osipov, D. Ray, T. J. A. Wolf, S. Bari, P. Walter, Z. Li, S. Moeller, A. Knie & P. V. Demekhin *Site-specific interrogation of an ionic chiral fragment during photolysis using an X-ray free-electron laser*, Commun. Chem. **Vol. 4, No. 119** (2021).

13. T. Jahnke, R. Guillemin, L. Inhester, S.-K. Son, G. Kastirke, M. Ilchen, J. Rist, D. Trabert, N. Melzer, N. Anders, T. Mazza, R. Boll, A. De Fanis, **V. Music**, Th.Weber, M.Weller, S. Eckart, K. Fehre, S. Grundmann, A. Hartung, M. Hofmann, C. Janke, M. Kircher, G. Nalin, A. Pier, J. Siebert, N. Strenger, I. Vela-Perez, T. M. Baumann, P. Grychtol, J. Montano, Y. Ovcharenko, N. Rennhack, D. E. Rivas, R.Wagner, P. Ziolkowski, P. Schmidt, T. Marchenko, O. Travnikova, L. Journel, I. Ismail, E. Kukk, J. Niskanen, F. Trinter, C. Vozzi, M. Devetta, S. Stagira, M. Gisselbrecht, A. L. Jäger, X. Li, Y. Malakar, M. Martins, R. Feifel, L. Ph. H. Schmidt, A. Czasch, G. Sansone, D. Rolles, A. Rudenko, R. Moshammer, R. Dörner, M. Meyer, T. Pfeifer, M. S. Schöffler, R. Santra, M. Simon, and M. N. Piancastelli, *Inner-Shell-Ionization-Induced Femtosecond Structural Dynamics of Water Molecules Imaged at an X-Ray*

Free-Electron Laser, Phys. Rev. X **10**, 041044 (2021).

14. X. Li, A. Rudenko, T. Mazza, A. Rörig, N. Anders, Th. M. Baumann, S. Eckart, B. Erk, A. De Fanis, K. Fehre, R. Dörner, L. Foucar, S. Grundmann, P. Grychtol, A. Hartung, M. Hofmann, M. Ilchen, Ch. Janke, G. Kastirke, M. Kircher, K. Kubicek, M. Kunitski, S. Meister, N. Melzer, J. Montano, **V. Music**, G. Nalin, Y. Ovcharenko, Ch. Passow, A. Pier, N. Rennhack, J. Rist, D. E. Rivas, I. Schlichting, L. Ph. H. Schmidt, Ph. Schmidt, M. S. Schöffler, J. Siebert, N. Strenger, D. Trabert, F. Trinter, I. Vela-Perez, R. Wagner, P. Walter, M. Weller, P. Ziolkowski, A. Czasch, M. Meyer, T. Jahnke, D. Rolles, and R. Boll, *Resonance-enhanced x-ray multiple ionization of a polyatomic molecule*, Phys. Rev. A **105**, 053102 (2022).

15. X. Li, A. Rudenko, M. S. Schöffler, N. Anders, Th. M. Baumann, S. Eckart, B. Erk, A. De Fanis, K. Fehre, R. Dörner, L. Foucar, S. Grundmann, P. Grychtol, A. Hartung, M. Hofmann, M. Ilchen, Ch. Janke, G. Kastirke, M. Kircher, K. Kubicek, M. Kunitski, T. Mazza, S. Meister, N. Melzer, J. Montano, **V. Music**, G. Nalin, Y. Ovcharenko, Ch. Passow, A. Pier, N. Rennhack, J. Rist, D. E. Rivas, I. Schlichting, L. Ph. H. Schmidt, Ph. Schmidt, J. Siebert, N. Strenger, D. Trabert, F. Trinter, I. Vela-Perez, R. Wagner, P. Walter, M. Weller, P. Ziolkowski, A. Czasch, D. Rolles, M. Meyer, T. Jahnke, and R. Boll, *Coulomb explosion imaging of small polyatomic molecules with ultrashort x-ray pulses*, Phys. Rev. Research **4**, 013029 (2022).

16. R. Boll, J. M. Schäfer, B. Richard, K. Fehre, G. Kastirke, Z. Jurek, M. S. Schöffler, M. M. Abdullah, N. Anders, T. M. Baumann, S. Eckart, B. Erk, A. De Fanis, R. Dörner, S. Grundmann, P. Grychtol, A. Hartung, M. Hofmann, M. Ilchen, L. Inhester, C. Janke, R. Jin, M. Kircher, K. Kubicek, M. Kunitski, X. Li, T. Mazza, S. Meister, N. Melzer, J. Montano, **V. Music**, G. Nalin, Y. Ovcharenko, Ch. Passow, A. Pier, N. Rennhack, J. Rist, D. E. Rivas, D. Rolles, I. Schlichting, L. Ph. H. Schmidt, P. Schmidt, J. Siebert, N. Strenger, D. Trabert, F. Trinter, I. Vela-Perez, R. Wagner, P. Walter, M. Weller, P. Ziolkowski, S.-K. Son, A. Rudenko, M. Meyer, R. Santra and T. Jahnke, *X-ray multiphoton-induced Coulomb explosion images complex single molecules*, Nat. Phys. **18**, 423–428 (2022).

17. F. Allum, **V. Music**, L. Inhester, R. Boll, B. Erk, P. Schmidt, T. M. Baumann, G. Brenner, M. Burt, P. V. Demekhin, S. Dörner, A. Ehresmann, A. Galler, P. Grychtol, D. Heathcote, D. Kargin, M. Larsson, J. W. L. Lee, Z. Li, B. Manschwetus, L. Marder, R. Mason, M. Meyer, H. Otto, Ch. Passow, R. Pietschnig, D. Ramm, K. Schubert, L. Schwob, R. D. Thomas, C. Vallance, I. Vidanović, C. von Korff Schmising, R. Wagner, P. Walter, V. Zhaunerchyk, D. Rolles, S. Bari, M. Brouard & M. Ilchen,*A localized view on molecular dissociation via electron-ion partial covariance*, Commun. Chem. **5**, 42 (2022).

18. G. Kastirke, F. Ota, D. V. Rezvan, M. S. Schöffler, M. Weller, J. Rist, R. Boll, N. Anders, T. M. Baumann, S. Eckart, B. Erk, A. De Fanis, K. Fehre, A. Gatton, S. Grundmann, P. Grychtol, A. Hartung, M. Hofmann, M. Ilchen, C. Janke, M. Kircher, M. Kunitski, X. Li, T. Mazza, N. Melzer, J. Montano, **V. Music**, G. Nalin, Y. Ovcharenko, A. Pier, N. Rennhack, D. E. Rivas, R. Dörner, D. Rolles, A. Rudenko, Ph. Schmidt, J. Siebert, N. Strenger, D. Trabert, I. Vela-Perez, R. Wagner, Th. Weber, J. B. Williams, P. Ziolkowski, L. Ph. H. Schmidt, A. Czasch, Y. Tamura, N. Hara, K. Yamazaki, K. Hatada, F. Trinter, M. Meyer, K. Ueda, Ph. V. Demekhin and T. Jahnke, *Investigating charge-up and fragmentation dynamics of oxygen molecules after interaction with strong X-ray free-electron laser pulses*, Phys. Chem. Chem. Phys. **24**, 27121-27127 (2022).

19. A. De Fanis, M. Ilchen, A. Achner, T. M. Baumann, R. Boll, J. Buck, C. Danilevsky, S. Esenov, B. Erk, P. Grychtol, G. Hartmann, J. Liu, T. Mazza, J. Montano, **V. Music**, Y. Ovcharenko, N. Rennhack, D. Rivas, D. Rolles, P. Schmidt, H. Sotoudi Namin, F. Scholz, J. Viefhaus, P. Walter, P. Ziolkowski, H. Zhanga and M. Meyer, *High-resolution electron time-of-flight spectrometers for angle-resolved measurements at the SQS Instrument at the European XFEL*, J. Synchrotron Rad. **29**, 755–764 (2022).

20. T. Mazza, T. M. Baumann, R. Boll, A. De Fanis, P. Grychtol, M. Ilchen, J. Montano, **V. Music**, Y. Ovcharenko, N. Rennhack, D. E. Rivas, A. Roerig, P. Schmidt, S. Usenko, P. Ziołkowski, D. La Civita, M. Vannoni, H. Sinn, B. Keitel, E. Ploenjes, U. F. Jastrow, A. Sorokin, K. Tiedtke, K. Mann, B. Schaefer, N. Breckwoldt, S.-K. Son and M. Meyer, *The beam transport system for the Small Quantum Systems instrument at the European XFEL: optical layout and first commissioning results*, J. Synchrotron Rad. **30** (2023).

21. T. M. Baumann, R. Boll, A. De Fanis, P. Grychtol, M. Ilchen, U.F. Jastrow, M. Kato, C. Lechner, T. Maltezopoulos, T. Mazza, J. Montano, **V. Music**, Y. Ovcharenko, N. Rennhack, D.E. Rivas, N. Saito, P. Schmidt, S. Serkez, A. Sorokin, S. Usenko, J. Yan, G. Geloni, T. Tanaka, K. Tiedtke, and M. Meyer, *Harmonic radiation contribution and X-ray transmission at the Small Quantum Systems instrument of European XFEL*, J. Synchrotron Rad. **30** (2023).

V. Music et al., *Wavelength-dependent Photodissociation of Iodomethylbutane*, in preparation (2024).

Acknowledgement

The last 4.5 years were a great adventure. I had the immense luck of meeting you Markus during a shift in the BKR on the DESY campus. We were together on the commissioning shift and had the great opportunity and privilege to be a part of the team playing around with the first photons of EuXFEL, even much earlier before the first experiments started. Now, years later, I can say, I never regret my choice to work with you. Besides the great topic and scientific environment (within the Peter-Paul-Ewald Volkswagen fellowship), you gave me all the freedom to develop and supported me whenever requested. You always had an open ear for everything. I always felt supported and valued by you. You have such a great personality, and you are inspiring me, besides your tremendous scientific success, especially with your human values, which are in my opinion even more valuable. You are a real role model of self-reflection, and I learned that I should never stop working on myself. For me, you were the perfect supervisor and I could easily fill several pages about all the extremely nice experiences working with you, but let it be short: Thanks for everything, Markus!

The FLASH beamtime 2018 started a few weeks after the start of my PhD. During this time, I met so many great people within this collaboration. A special thanks to Christopher Passow, who helped me in the beginning to find the right paths for the data analysis. A big thanks also to Daniel Ramm, who helped a lot by borrowing equipment or showing me how to use the ultrasonic bath properly. An enormous thanks to Benjamin Erk, who helped during the preparation time, discussions, and analysis. I am sorry, but somehow you did not get rid of me. Thanks for all your time, answering all my questions, the discussions we had, and the borrowed parts saving us and our experiment. You were really a crucial part of the progress and success of many things related to my work. You impressed me with your kindness and professionalism.

My second stop during this journey was the SQS team at the EuXFEL under the lead of Michael Meyer. I want to thank Michael for the chance to be involved in the early science phase and the first experiments at SQS. It was a pleasure to work with you and the whole team. A huge thanks to Pawel Ziolkowski, who supported me with so many things. He was the first one to help to build my first Rose-Krieger construction. He was also helping with smaller design parts. I bothered him even when he left the group. We discussed CAD model modifications, my CAD viewer problems, undulator stuff, and many

more things. Your help contributed tremendously. Many thanks, you are a great engineer and person. I really appreciated your positivity.

The next stop was my SLAC stay in 2020. Thanks to Peter Walter, who initiated and hosted my stay. Without him and Markus, this great experience would still be a dream. It was a pleasure to work with you, Peter. I learned so much and this experience is priceless. At this point, I need to say also many thanks to Xiang Li, I learned a lot from him related to SIMION simulations. You are a really open-minded person and I enjoyed working with you.

In between, the Corona pandemic caught all of us, but this was, for me personally, a wonderful time because I got my lovely son in the summer of 2020. After my return from parental leave in 2021, I focused on the build-up of the DVMI spectrometer. So many people helped me, and I want to express my sincerest gratitude to everyone. To emphasize at this point, huge contributions by Michael Lüdecke, who was a big help related to hardware work, tightening all my loose screws, and who helped me later to transport the set-up to DESY. Yvheniji Ovcharenko, who was an important consultant and who showed me how to make the threads into Rose-Krieger parts. Rebecca Boll was always open to discussing new ideas and contributed a lot to many things related to the work. Thanks for everything! And I want to thank everyone at EuXFEL, there are so many more people, who were involved and without them, plenty of things would not be able, including people from the beam transport group, vacuum group, undulator group, IT, HR, and many more. Thanks to everyone.

My journey continued then at FLASH, as a member of the FLASH-D group under the lead of Kai Tiedtke. Kai, you were always very kind and created a super pleasant environment for me as a person, but also for the DVMI spectrometer. Besides, I had the big chance and luck to work with some group members closely together. Special thanks to Yilmaz Bican, Fini Jastrow, Michael Walther, and Markus Degenhardt, who were tightly involved in the preparation and commissioning of the DVMI spectrometer. You all contributed so much, and I want to thank you honestly for all your effort and time. It was such a nice atmosphere and a lot of fun working with you. I also want to thank everyone involved in the commissioning beamtime of the DVMI performed at the PTB. I am happy for every single person, who contributed before, during the beamtime, or afterward. You were all indeed crucial for the success.

My deepest gratitude goes to Maciej Brachmanski, who was absolutely the project saver for the DVMI from the engineering perspective. He invested a lot of his time into the CAD models, adaptions, and many more things, that I cannot even list. Maciej, you are a great thinker, experienced engineer, and creative problem solver. It was such a pleasure to work with you and learn from you. You are such a great personality and I hope I can be your trainee for a short time to assimilate the basic CAD skills, so I do not need to bother you

in the future. Thanks also to Elke Plönjes-Palm, who allowed us to involve Maciej so much in the quite time-consuming project.

Especially at the end of my journey, I was in an exchange with Felix Allum. Felix, you offered your help whenever possible and impressed me with your kindness. Thank you very much. I also want to thank Sara Savio, for her full engagement whenever needed. Sara, you were always there when I needed additional hands and I could always count on you, and this is something really valuable. Thank you so much! A big thanks also to Thorsten Otto, who volunteered to proofread parts of this work.

A special thanks, goes also to the people in Kassel (within the DFG project No. 328961117 - SFB 1319 ELCH: Extreme light for sensing and driving molecular chirality). Prof. Arno Ehresmann, my supervisor in Kassel. Thank you for giving me the freedom to perform the research in Hamburg and the support whenever requested. A big thanks also to Prof. Buhmann and Prof. Giesen, who were a part of the examination committee. I also want to thank Dana Bloß, who was my contact person regarding all my questions about the University of Kassel. You were such a big help and my bridge from Hamburg to Kassel. Thanks a lot. And I need to thank Andrea Wecker, who was the biggest support related to administrative tasks. You helped me so much, and I want to thank you, sincerely.

Not to forget all my office roommates. First, I shared an office with the brilliant guys from the undulator group, under the lead of Joachim Pflüger. Thanks to Joachim for the office space for a longer time than agreed, especially in the light of office shortage. Second, to Florian Preißkorn, Uwe Englisch and Majid Bagha-Shanjani. It was so fun sharing with you the office. Thanks for the extraordinary atmosphere and all the help you offered as well, related to the build-up process of the DVMI. You were often the additionally needed strong hands, required to lift heavy vacuum pumps. Thank you so much! My office at DESY I shared with Sven Ackermann and Mahdi Bidhendi, thanks for all the nice conversations and the kind welcome.

I want, of course, to thank people outside academia. My friends, and my whole family, especially my parents and sister for believing, supporting, and being proud of me. Also, a big thanks to other mommies in my social environment, who took great care of my son, especially at the end of my PhD. I am thankful to have all of you! A special thanks and my deepest gratitude to my grandparents, Nana and Deda. You left everything behind you in Serbia and moved to Germany and worked day and night to offer us a better future. My grandmother went only to primary school because she did not have the opportunity to continue, but she was a really open-minded, intelligent, and inspiring person. She and all my family taught me the values of life and shaped my personality tremendously. I am so thankful for everything. Болим Вас. Many thanks to all those who may not have been mentioned explicitly

but who contributed as well.

And finally, thanks to my best friend and husband, who has been by my side since I started to study physics in 2012. You are always supporting me, and we experienced and achieved so much individually and together over the last few years. I am so grateful for being your wife and the mother of our beloved sons. This journey of the PhD studies came to an end and we as a family are looking forward to a bright future. Тако сам поносна што вас имам. Ви сте моје благо. Бескрајно вас волим!